Design of the Dual-Shaped Triple Layer Pillbox Antenna

by
Charl Wynand Baard

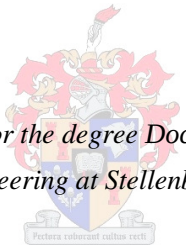

Dissertation presented for the degree Doctor of Philosophy in the Faculty of Engineering at Stellenbosch University.

Supervisor: Prof. K. D. Palmer
Department of Electrical & Electronic Engineering

March 2013

DECLARATION

By submitting this thesis electronically, I declare that the entirety of the work contained therein is my own, original work, that I am the sole author thereof (save to the extent explicitly otherwise stated), that reproduction and publication thereof by Stellenbosch University will not infringe any third party rights and that I have not previously in its entirety or in part submitted it for obtaining any qualification.

Date: 22 February 2013

ABSTRACT

The triple layer pillbox antenna is an antenna topology well suited for use as a stackable "plank" element in radar applications. Its suitability arises from the folding which makes it compact, and from the layered nature which can be exploited for low cost manufacture. Existing designs of these "cheese" antennas, whether two or three layers, suffer from two drawbacks: a) The bend or fold between layers introduces undesirable reflections and b) Due to their parabolic sector geometry virtually no pattern control is available to the designer. This work addresses both of these shortcomings.

A low reflection transition is realized by introducing simple compensating elements into the design which, with minimal manufacturing complexity, offer high performance over a broad frequency and incidence angle range. To cater for pattern control the concept of "dual shaped reflectors" is borrowed from the high performance dish antenna literature and implemented in the pillbox geometry. This shaping offers limited but useful control of the aperture distribution and thus indirectly over the radiation pattern.

To test these innovations three X-band antennas have been designed, built and measured. An initial unshaped geometry is used for the first design to show the fold or bend performance. This antenna has a simulated and measured $2GHz$ usable bandwidth, with a reflection coefficient below $-10dB$ and side-lobes below $-27dB$ over a bandwidth in excess of 20%. Shaping is then added to show how either side-lobe levels can be lowered to below $-32dB$, or the gain enhanced by $2dB$. The enhanced designs have been built and experimentally verified.

OPSOMMING

Die drie-dubbel gevoude pildoos antenna is ‘n antenna topologie wat goed gepas is vir die gebruik as ‘n stapelbare ”plank” element vir radar aanwending. Sy geskiktheid kom vanwee die vou van die struktuur wat dit meer kompak maak sowel as die konstruksie moontlik goedkoper maak. Huidige ontwerpe van die antenna strukture, hetsy twee of drie lae, ly aan twee tekortkominge: a) Die buiging of vou tussen die lae veroorsaak ongewensde weerkaatsings en b) Weens hul paraboliese meetkunde is feitlik geen beheer oor die stralings patroon beskikbaar nie. Hierdie werk spreek beide hierdie tekortkominge aan.

‘n Lae weerkaatsing by die oorgang is verkry deur eenvoudige kompenserende elemente by die ontwerp in te voeg wat, met minimale vervaardigings kompleksiteit, hoë werkverrigting lewer oor ‘n breë frekwensie en invals hoek spektrum. Om patroon beheer te voorsien is die konsep van ”dubbele gevormende weerkaatsers” geleen vanaf die hoë verkverrigting skottel antenna literatuur en in die pildoos meetkunde ingestel. Hierdie vorming lewer beperkte dog nuttige beheer oor die openings verspreiding en dus indirek oor die stralings patroon.

Om hierdie nuwighede te toets is drie X-band antennas ontwerp wat gebou en gemeet is. ’n Aanvanklike ongevormende meetkunde is gebruik vir die eerste ontwerp om die vou of buiging se werksverrigting te bewys. Hierdie antenna het ‘n gesimuleerde en gemete $2GHz$ bruikbare bandwydte met ‘n weerkaatsings kwosiënt onder $-10dB$ en sylobbe van minder as $-27dB$ oor ‘n bandwydte van meer as 20%. Vorming is dan bygevoeg om te bewys dat òf verlaagde sylobbe van onder $-32dB$ òf verhoogde aanwins met $2dB$ verkrygbaar is. Die verbeterde ontwerpe is gebou en eksperimenteel bewys.

CONTENTS

LIST OF FIGURES

LIST OF TABLES

LIST OF ABBREVIATIONS AND SYMBOLS

2D - Two Dimensional

AUT - Antenna Under Test

dB - Decibel

dBi - Decibel Isotropic

FFT - Fast Fourier Transform

FMCW - Frequency-modulated continuous-wave

f/D - focal depth over width

GHz - Gigahertz

GO - Geometric Optics

k - Propagation constant

λ - Wave length

Ω - Ohm

PEC - Perfect Electric Conductor

VNA - Vector Network Analyzer

SLL - Side-lobe Level

CHAPTER 1
Introduction

1.1 Overview

Short to moderate ground to air radar systems targeting the air traffic control or area surveillance market typically require an X-band antenna element with a fan-beam radiation pattern and low azimuth side-lobes. From Aperture Spectrum Theory this beam shape can be obtained from 'plank' shaped, i.e. horizontally long and vertically thin, antenna elements which are stacked vertically to obtain elevation resolution. Current designs have proven to be expensive and difficult to manufacture, resulting in poor performance. This dissertation focuses on the design of such a plank element with the vertical stacking and combining not being addressed. The design will be based on antenna specifications from a local radar company. This company requires an antenna for FMCW radar to have the following specifications:

- Antenna specifications:

  1. A fan-beam elevation radiation pattern
  2. Low azimuth side-lobes (below $-30dB$)
  3. X-band operation (centre frequency of $9.5GHz$)
  4. A $2GHz$ ($\approx 20\%$) bandwidth
  5. $30dBi$ Gain
  6. 1° beam-width
  7. Stackable plank element
  8. Low cost and easy to manufacture
  9. Power handling capabilities of $< 50Watt$ for FMCW
  10. Final dimensional restraints of 2.4m wide and 0.6m deep

The proposed antenna to this problem is the pillbox antenna, Figure 1.1, of which the flat structure makes it useable as a stacked plank element. Structural simplicity makes the pillbox structure a cheap, manufacturable design. Unfortunately the single layer pillbox antenna suffers from performance degradation due to the aperture blockage caused by the feed in the radiating

aperture of the antenna. To solve the problem of aperture blockage a multi-layered pillbox antenna is designed.

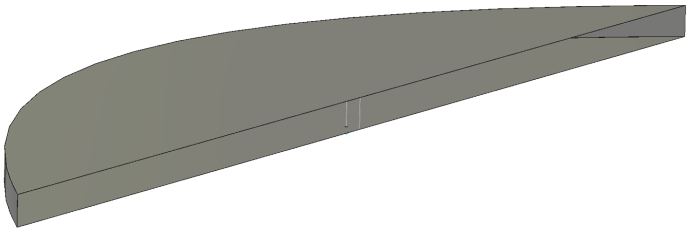

Figure 1.1: Model of a traditional Single Layer Pillbox antenna

A multi-layered pillbox antenna solves aperture blockage by removing the feed from the aperture and simultaneously results in a more compact structure as shown in Figure 1.2. The limiting factor of these structures is the coupling at the transitions. These transition areas need to effectively couple energy from one layer to the next while maintaining structural simplicity. Current designs either lack the necessary bandwidth or are difficult to manufacture. In this dissertation a compensated transition is designed for adequate bandwidth while maintaining structural simplicity. This compensated transition is then incorporated into a multi-layered structure from which a triple layer pillbox antenna is acquired.

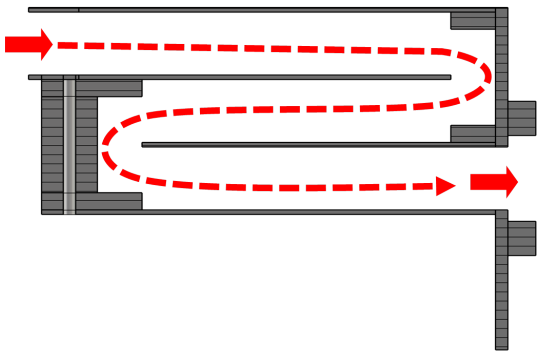

Figure 1.2: Diagram illustrating the idea of a multi-layered structure

The triple layer pillbox antenna is a multi-layered structure consisting of a feed layer which contains the feed, an aperture layer which opens in the antenna aperture and a middle layer which connects the other layers as shown in Figure 1.3. This structure is compact and has a

symmetrical aperture which results in the required symmetrical azimuth and elevation patterns. It is further shown that the structure can be manufactured using stacked laser-cut aluminium plates, resulting in a relatively cheap antenna structure. Evaluation of the antenna's performance is first done through simulation before the antenna is built and measured.

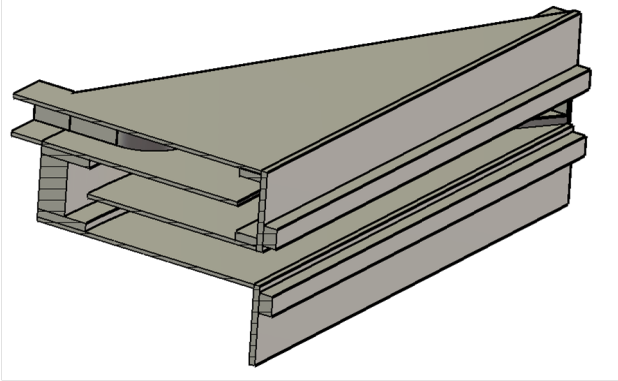

Figure 1.3: Model of a Triple Layer Pillbox antenna

Further improvement can be made if the transition between layers allows for good coupling, this allows the triple layered structure to be mathematically simplified to a two dimensional model, consisting of two reflectors as shown in Figure 1.4. Dual reflector shaping can be implemented on these reflectors, allowing for some control over the aperture distribution and thus the azimuth radiation pattern. Two antennas are designed using dual reflector shaping to obtain different radiation patterns. These antennas are evaluated using the same techniques used for the unshaped triple layer pillbox antenna.

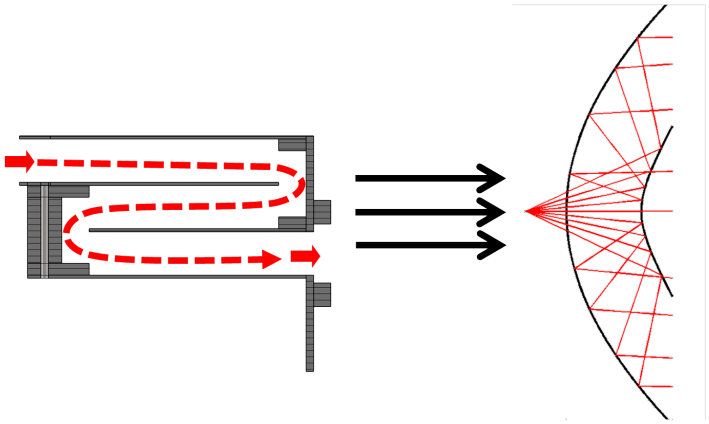

Figure 1.4: Diagram illustrating the simplification of the Triple Layered Pillbox to a two dimensional model

At the end of this dissertation a design process is obtained through the process described in Figure 1.5 in which a triple layered pillbox antenna is designed for a required aperture distribution. The design process is verified through the measured results taken from antennas designed and constructed for different configurations.

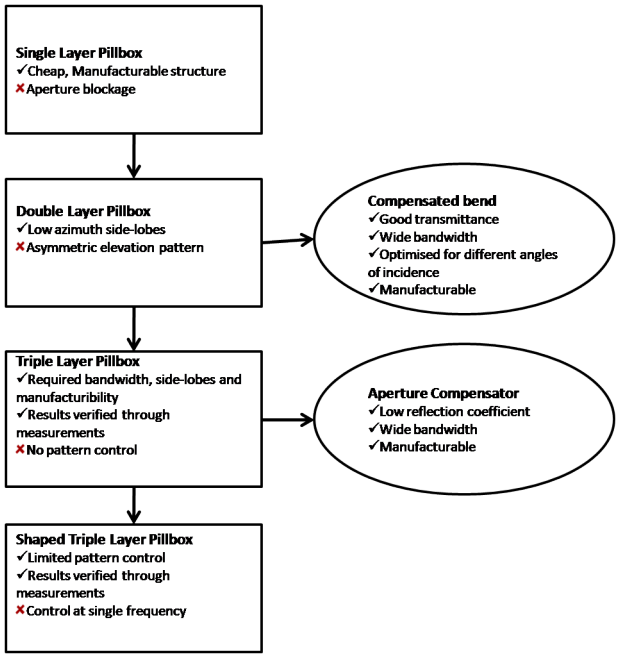

Figure 1.5: Development chart of process used to design a Dual Shaped Triple Layer Pillbox antenna

1.2 Single Layer Pillbox Antenna

1.2.1 Introduction to Single Layered Pillbox Antennas

This section gives a brief overview of the single layer pillbox antenna. Limitations of the traditional pin and waveguide fed pillbox antennas are investigated through the use of simulated results. It is found that aperture blockage caused by the positioning of the feed in the aperture has a significant impact on antenna performance. The feed is removed from the aperture through the offset fed pillbox found in the literature. Limitations to the offset fed pillbox are discussed and the antenna structure is found to be too large for the requirements of this project.

A pillbox antenna is essentially a cylindrical reflector wedged between two parallel plates. Energy from a point source is reflected off a reflector and culminated into a plane wave front. Pillbox antennas are linearly polarised and can be either E-plane or H-plane type antennas. The high gain and fan-beam radiation pattern obtained from pillbox antennas make these antenna structures ideal for radar applications.

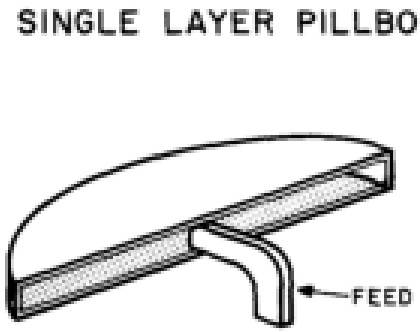

Figure 1.6: Single Layer Pillbox from literature, [1]

The pillbox feed is traditionally located at the focal point of the reflector. For symmetrical antennas this is located in the middle of the aperture. Either a pin or waveguide feed can be used, depending on the system requirements. Further variations of these feeds can be found through the use of stubs which are used to obtain better impedance matching and reflector illumination, not discussed in this dissertation.

The pin feed is usually the easiest feed to mechanically implement into a system. Through simulation it is shown that although acceptable bandwidth is obtainable through matching and the relatively small size of the pin allows for little aperture blockage, the large back-lobe of the pin feed deteriorates the far-field pattern, resulting in side-lobe levels of more than $-10dB$.

Waveguide structures offer the best bandwidth, are rigid and can handle high power which is ideal for radar applications. Simulated results show that waveguides tend to focus energy, causing reflector illumination to become a concern when implemented into a pillbox antenna. The large structure of a waveguide causes aperture blockage which deteriorates the far-field patterns and significantly reduces bandwidth.

Some work has been done to minimize the effect of aperture blockage in symmetrical single layer pillbox antennas through the design of complicated feeding systems [1], [2]. Unfortunately there has been little success in acquiring the desired low side-lobe levels. It is shown that the problem of aperture blockage can be solved by using an offset fed antenna. This configuration is shown to yield low side-lobes in the literature, but requires a much larger structure to be implemented than is possible for this project.

1.2.2 Coordinate system

Unless stated otherwise the coordinate system shown in Figure 1.7 will be used throughout this dissertation. For the cartesian coordinate system the *x-axis* is defined as the axis normal to the radiating aperture of the antenna. The *y-axis* is the axis perpendicular to the parallel plates and the *z-axis* runs normal to the direction of propagation.

In the spherical coordinate system *Theta* is defined as the angle from the *z-axis* to the *x-axis* and *Phi* the angle from the *x-axis* to the *y-axis*.

The azimuth far-field pattern is defined along *Theta* with a constant $Phi = 0^\circ$ and the elevation pattern along *Phi* with a constant $Theta = 90^\circ$.

1.2.3 Limitations of Single Layered Pillbox Antennas

To determine the obtainable antenna performance in terms of bandwidth and side-lobe levels, a relatively small pillbox is designed. An antenna width of 10λ is chosen for reasonable simulation time while still being electrically large.

A parabolic curve is chosen for the reflector shape. The path length of all rays from the focal point of the parabolic curve to its aperture is the same and is reflected off the reflector parallel to each other, shown in Appendix.A. This enables a flat phase distribution at the aperture. The spacing between the parallel plates needs to be less than $\lambda/4$ to suppress higher order modes of propagation, but not too small to keep losses down. For this design the spacing is chosen to be 10.16mm to conform to the dimensions of the WR-90 waveguide port which will be used

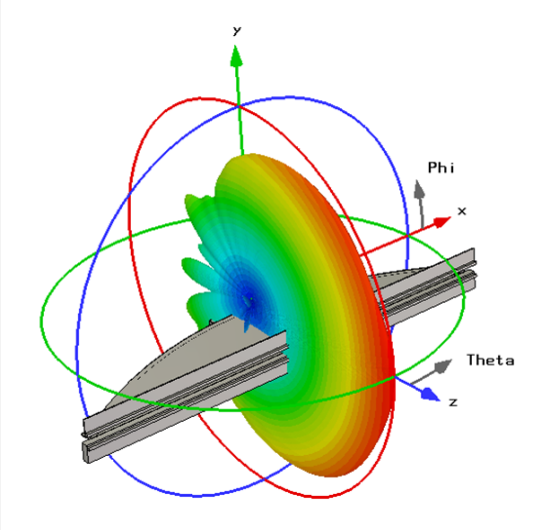

Figure 1.7: Coordinate system used within dissertation

later on. The focal depth must be chosen to be as large as possible to obtain a large f/D (focal depth to width) ratio and assure the best reflector illumination possible. A focal depth of 2.2λ is calculated to be the optimum value.

A pin and waveguide feed is implemented in the pillbox design to evaluate each system's performance.

1.2.3.1 Single Layered Pillbox Antenna with Pin Feed

Extending the inner conductor of a 50Ω coaxial cable to penetrate through one of the parallel plates at the reflector's focal point creates the feed pin seen in Figure 1.8.

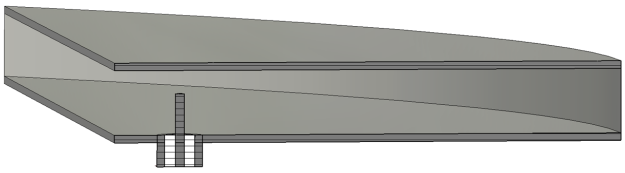

Figure 1.8: Model of a Single Layer Pillbox with a pin feed

The length of the pin is adapted through a parameter sweep to match the structure for the required bandwidth. The reflection coefficient in Figure 1.9 is found after optimisation and shows

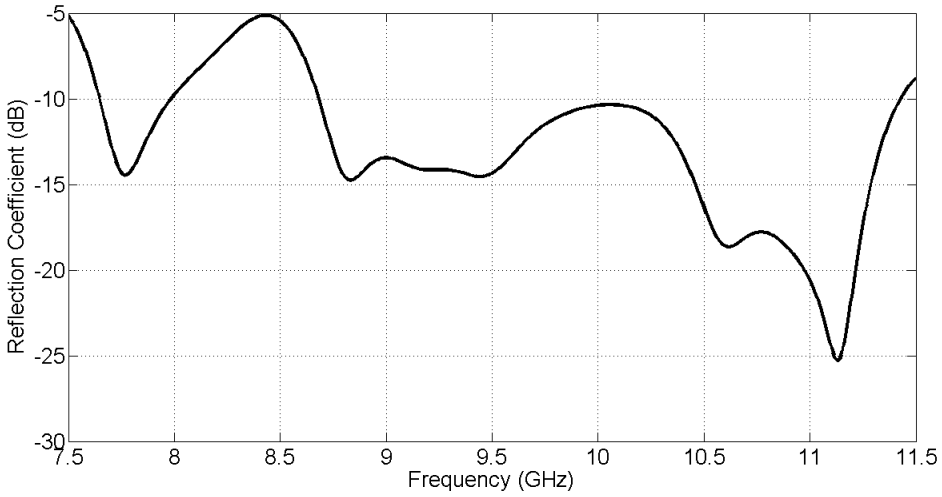

Figure 1.9: Reflection coefficient of Single Layer Pillbox with a pin feed

a $-10dB$ bandwidth of 27% at a centre frequency of $10GHz$.

The high side-lobes obtained in Figure 1.10 are primarily attributed to the large back lobe of the feed. Relative side-lobes of about $-10dB$ are obtained for higher frequencies which drop to $-8dB$ at lower frequencies.

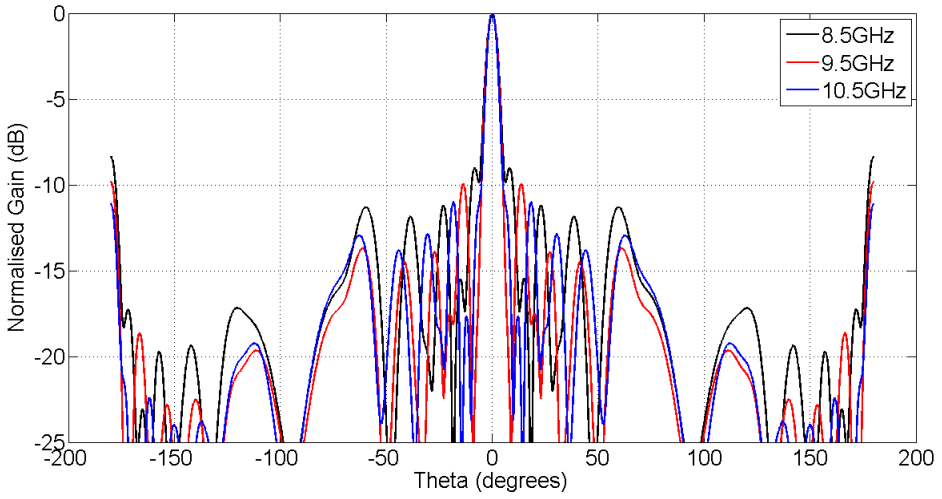

Figure 1.10: Azimuth far-field radiation pattern of Single Layer Pillbox with a pin feed

1.2.3.2 Single Layered Pillbox Antenna with Waveguide Feed

The pin feed is replaced by a waveguide feed which does not have the large back lobe of the pin feed. The waveguide feed is first designed separately from the system. Flares are attached to the sides and optimised for the best reflection coefficient. Once the optimal configuration is obtained, the waveguide is used as a feed in the pillbox structure.

Larger flares generally give a better reflection coefficient, but effectively increase the aperture of the waveguide, lowering the beam-width. The waveguide gives a wide $-10dB$ bandwidth as seen in Figure 1.11. Due to the large flares used to match the waveguide, the radiation pattern has a narrow beam-width, seen in Figure 1.12. This narrow beam-width will cause poor reflector illumination as well as an impedance mismatch due to the large amount of energy that will be reflected directly back into the feed.

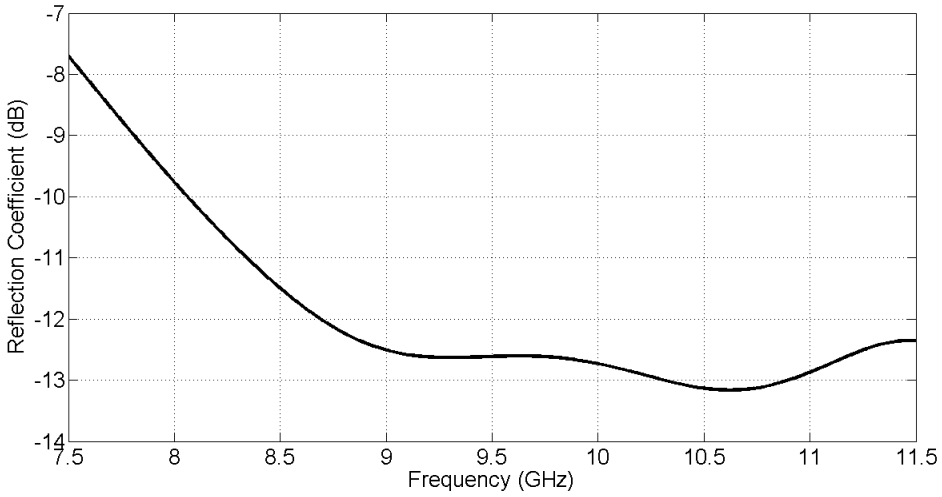

Figure 1.11: Reflection coefficient of flared waveguide

The waveguide is inserted at the aperture of the pillbox antenna. The offset of the waveguide is optimised to be located at the effective focal point of the reflector, shown in Figure 1.13.

From Figure 1.13 it is noted that the waveguide blocks a large part of the aperture. The parabolic reflector reflects rays incident on its centre directly back to the feed, this together with the narrow beam-width of the waveguide causes the majority of the energy to be reflected back into the waveguide, resulting in the impedance mismatch found in Figure 1.14.

One solution to this problem is to design the waveguide to have a wider beam-width and to

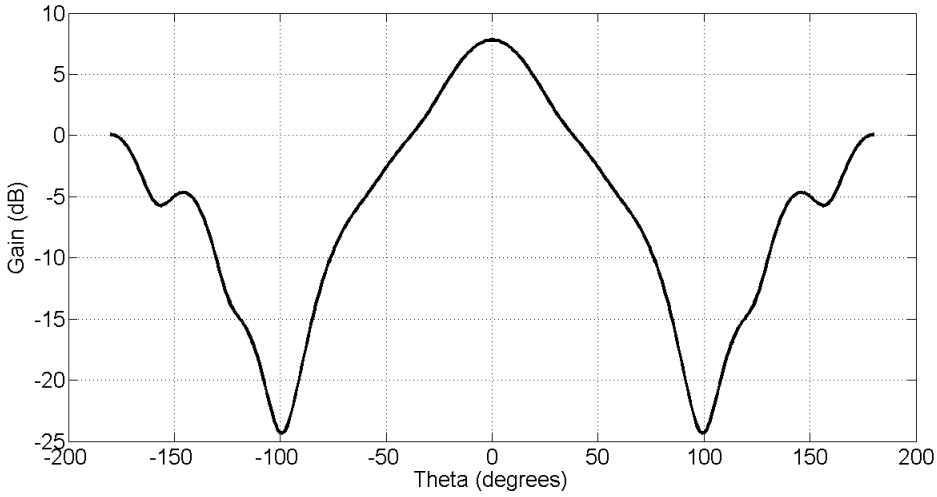

Figure 1.12: Radiation pattern of flared waveguide

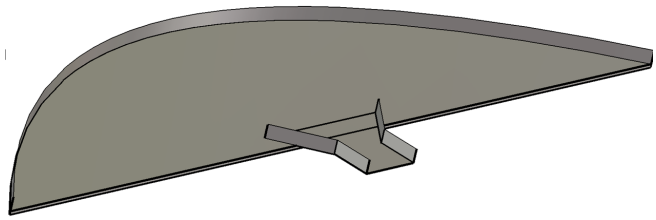

Figure 1.13: Model of a Single Layer Pillbox with a waveguide feed

radiate less energy in the centre through the use of stubs. Enlarging the pillbox width should also decrease the amount of energy reflected back into the feed.

1.2.3.3 Offset Fed Single Layered Pillbox Antenna

Lower side-lobes can be obtained by removing the feed from the aperture. This can be accomplished by using an offset feed as shown in Figure 1.15.

Great success has been made with this design with $-45dB$ side lobes over a 15% frequency band [3]. Greater control over the far-field pattern is obtainable through shaping of the reflector.

Dimensional restrictions imposed on this antenna design do however not allow for the use of an offset fed pillbox due to the extra space required to implement it.

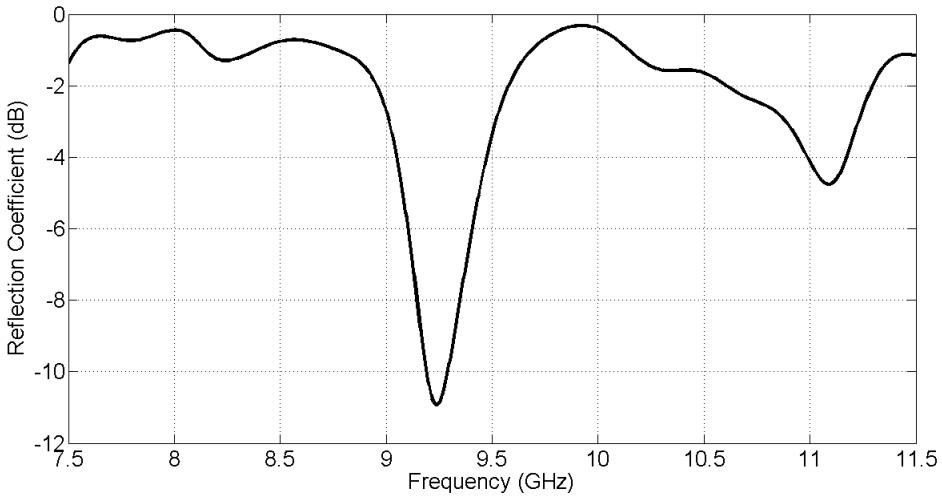

Figure 1.14: Reflection coefficient of Single Layer Pillbox with a waveguide feed

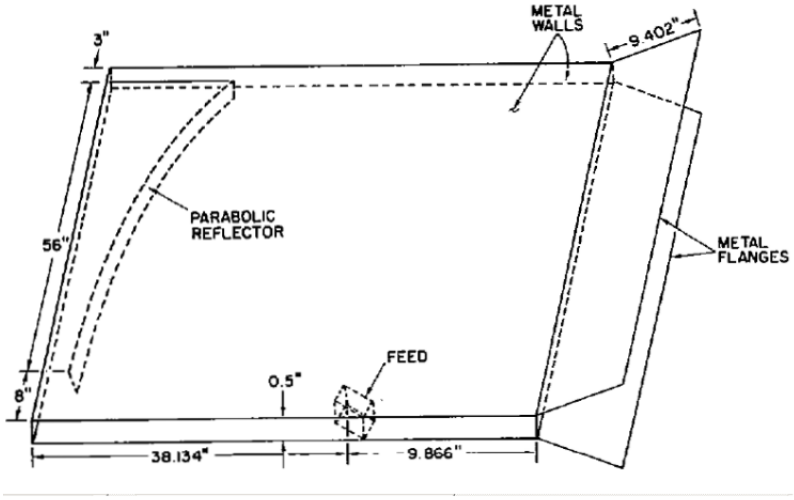

Figure 1.15: Diagram of a offset fed pillbox antenna, [3]

1.2.4 Conclusion on Limitations of Single Layered Pillbox Antenna

Acceptable bandwidth of 20% is obtainable from the pin feed, but not from the waveguide feed. Better results are obtained for a pin feed due to the large aperture blockage caused by the waveguide feed. The amount of energy reflected back into the waveguide might be decreased further by increasing the size of the antenna, effectively reducing the size of the waveguide relative to the aperture.

None of the antenna designs delivered side-lobes lower than $-10dB$. This is primarily due to the aperture blockage caused by the feed structures as well as the large back lobe in the case of the pin feed.

From these results it is concluded that the feed needs to be removed from the aperture to obtain the required performance. A multi-layered structure is proposed to solve the problem of aperture blockage.

CHAPTER 2
Multi-Layered Pillbox Antenna

2.1 Introduction to Multi-layered Pillbox Antennas

This section describes the design of a multi-layered pillbox antenna which is obtained by moving the feed of a single layer pillbox to a separate layer, Figure 2.1. A compensated transition structure is designed to effectively couple energy from one layer to the next which is then adapted for different angles of incidence. It is shown that a tapered feed structure can be optimally matched and optimised to yield a practical radiation pattern to the reflector. Finally a double layer pillbox antenna is designed and simulated to incorporate the designed compensated transition and tapered feed. This antenna is found, through simulation, to yield the required azimuth side-lobe levels, but yields an asymmetric elevation pattern and requires a deep structure.

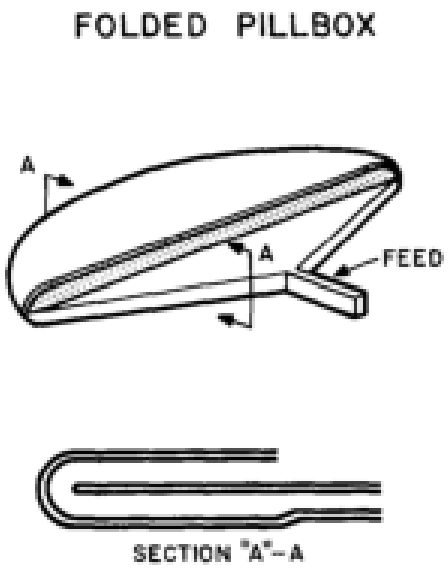

Figure 2.1: Double Layer Pillbox from literature, [1]

The main obstacle to a multi-layered pillbox is identified as the transition between separate layers. Common transitions together with transitions found in the literature are examined, but found to be inadequate for this application. The solution is found to be a compensated transition which is manufacturable and is shown through simulations to yield a reflection coefficient of less than $-27dB$ at different angles of incidence for a 20% bandwidth.

A rectangular waveguide is tapered at a determined angle to create the feed layer. It is shown that blending the transition between the rectangular and the tapered waveguide allows the feed to be matched to achieve a $-30dB$ reflection coefficient over the required 20% frequency band. It is further shown that the taper angle determines the radiation pattern beam-width, allowing one to design the feed according to the antenna requirements.

The double layer pillbox antenna is finally designed to incorporate the compensated transition and tapered feed layer. Although simulation results show the antenna to yield azimuth side-lobes of less than $-30dB$, an asymmetrical elevation pattern is obtained. The protruding feed layer is identified as the primary limitation to the double layer design as it results in the structure being deep, causes an asymmetric elevation pattern and also inhibits the use of an impedance matching structure at the aperture which would lower the antenna's reflection coefficient to below the acquired $-16.5dB$.

2.2 Design of Double Layered Pillbox Antenna

The double layer pillbox is designed in three separate stages. A structure is designed to be implemented in the 180° transition, which allows for optimal coupling between separate layers. This structure needs to be manufacturable and easy to implement in a pillbox structure. The feed is designed to be matched for the required bandwidth as well as radiate the optimal pattern to the reflector. Finally the feed and transition structure is incorporated into a double layer pillbox structure.

2.2.1 Transition Structure

An 180° transition is required for the transition from the one layer to the next, it needs to be well matched for a large bandwidth and manufacturable. Due to the different angles of incidence of the rays on the reflector, illustrated in Figure 2.2, the transition needs to be adapted for optimal coupling at different angles of incidence.

Most double layer pillbox designs make use of a simple slot in the common wall between the layers at the transition [4], [2]. This design has been successful for designs requiring less bandwidth and for pillboxes with large f/D ratios where the angle of incidence does not vary as much. This slotted transition is further investigated and found inadequate for the required specifications.

It will be shown that using a rounded transition yields better matching and can be better

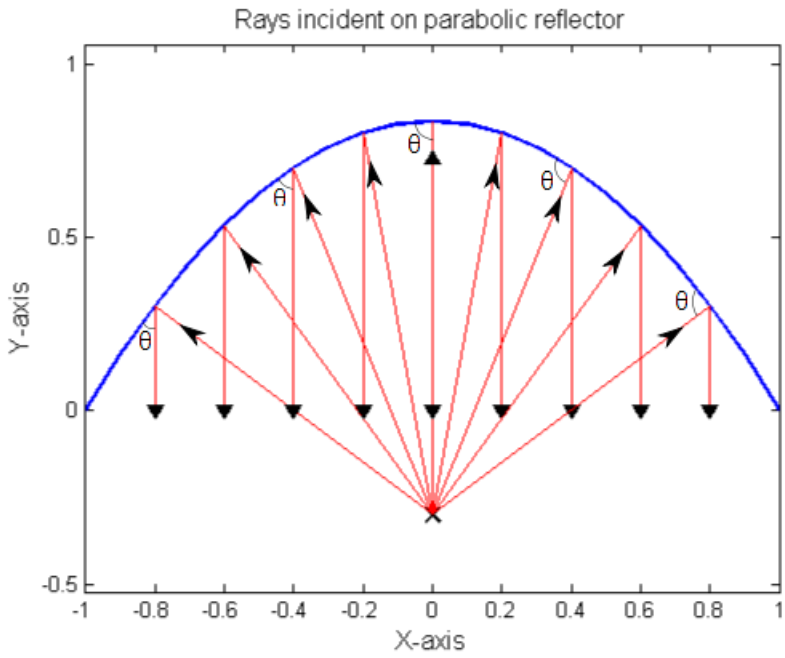

Figure 2.2: Diagram illustrating rays incident on parabolic reflector at different angles

adapted to different angles of incidence. This structure is however difficult to manufacture around the contour of the reflector.

Coupling holes [5] implemented in a H-plane antenna have been found to have a reflection of less than $-10dB$ over a 10% frequency band. These coupling holes can be designed for different angles of incidence as needed in a pillbox design.

Transitions are designed using the different configurations with a 1.2mm plate thickness and a spacing of 10.16mm between parallel plates to be compared to each other.

2.2.1.1 Slotted Transition

Cutting a slot into the common plate between the two layers allows energy from one layer to couple to the next. The width of the slot, Figure 2.3, is varied to optimise the transition for the lowest possible reflection for the required frequency band.

The slotted transition is simulated in *CST MWS* using the periodic boundary function in the frequency domain solver. Periodic boundaries at the sides of the model shown in Figure 2.4 allows the model to be effectively infinitely long and allows for different scan angles which make simulations for different angles of incidence possible. The slot width is optimised to obtain the

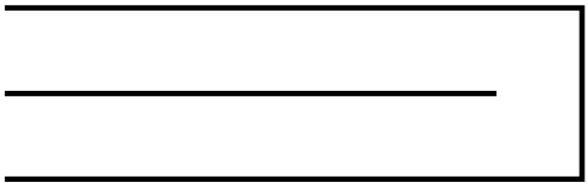

Figure 2.3: Diagram illustrating a slotted transition structure

minimum reflection coefficient in the required frequency band for different angles of incidence. Optimal results obtained are shown in Figure 2.5 for the corresponding width dimensions acquired at different angles of incidence which are shown in Table 2.1. This transition can be well matched for perpendicular angles of incidence, but struggles with some oblique angles. Implementing the slot into a pillbox antenna is not practical due to the large variation in the required slot width at different angles of incidence as well as the poor performance at some angles.

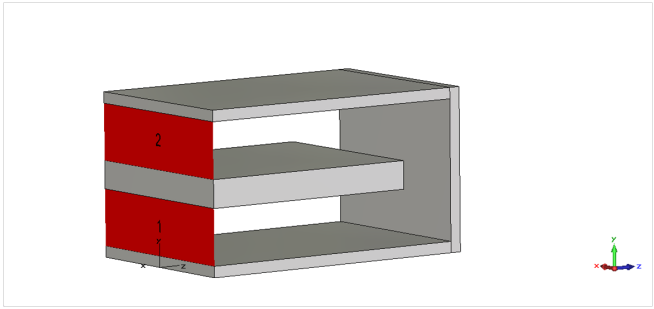

Figure 2.4: Model of slotted transition

Angle, θ (degrees)	Width(mm)
90	22.4
80	22
70	21.5
60	19
50	10
40	8.2

Table 2.1: Slot width necessary in slotted transition for impedance matching at different angles of incidence

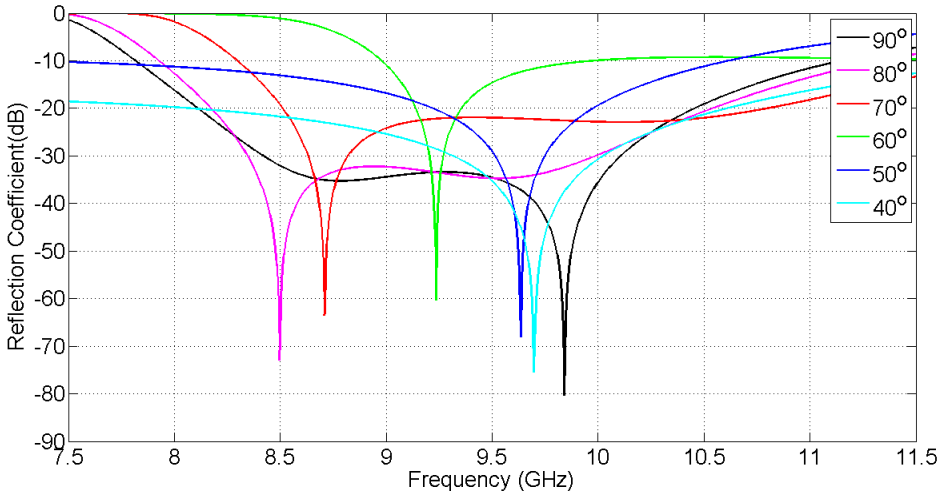

Figure 2.5: Reflection coefficient of slotted transition at different angles of incidence

2.2.1.2 Rounded Transition

Rounding the edges of the slotted transition creates a round transition, Figure 2.6. The radius of curvature adds an extra parameter for matching which, together with the slot width, can be optimised for optimal coupling.

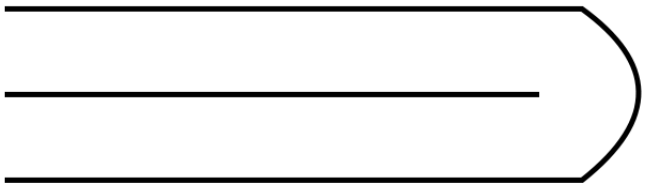

Figure 2.6: Diagram illustrating a round transition structure

Using the same techniques used for the slotted transition, the round transition is optimised for different angles of incidence at a fixed slot width of 1mm into the bend. Optimised values for the radius of the curve in Table 2.2 show much smaller values than needed in the slotted transition with less variation required for different angles. A reflection coefficient off less than $-23dB$ is found for all angles of incidence over the required frequency band in Figure 2.7. It is found that this structure performs better than the slotted transition with improved matching obtained for

different angles of incidence and less required variation in parameters. The drawback to this design is however the difficulty in manufacturing the curved structure along a curved path.

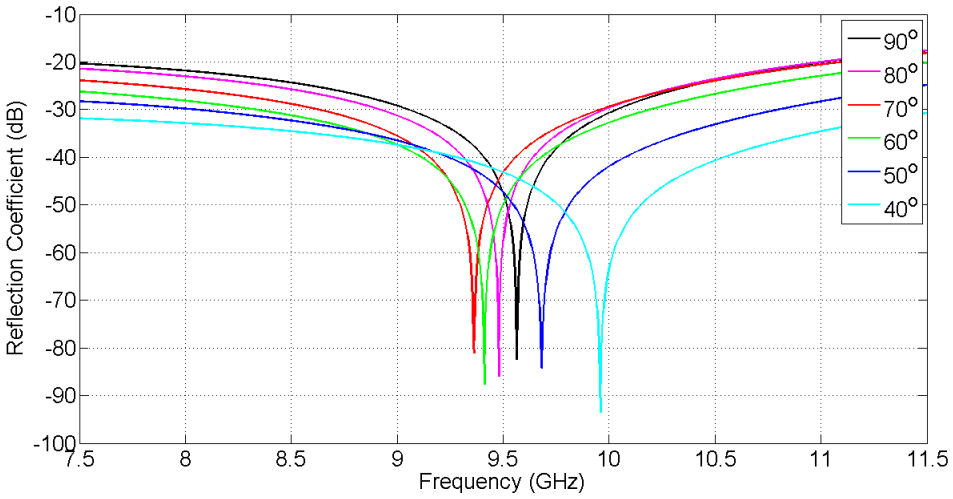

Figure 2.7: Reflection coefficient of round transition at different angles of incidence

Angle, θ (degrees)	Radius(mm)
90	10.6
80	10.5
70	10.4
60	10.2
50	9.9
40	9.7

Table 2.2: Curve radius necessary in round transition for impedance matching at different angles of incidence

2.2.1.3 Compensated Transition

It was decided to design a hybrid between the slotted transition and the round transition. This hybrid needs to have the manufacturing simplicity of the slotted transition together with the good performance of the round transition. The round edges of the round transition are replaced by rectangular extrusions, Figure 2.8, which are meant to create an electrically rounded transition.

It is shown through the use of the same simulation techniques discussed for the slotted tran-

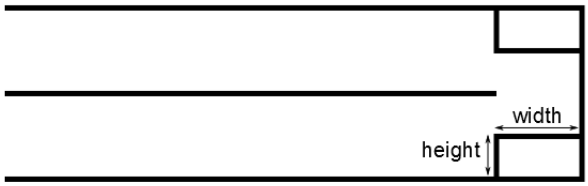

Figure 2.8: Diagram illustrating a compensated transition structure

sition that this structure can be optimised using the width and height of the extrusions as parameters. Varying the height of the extrusion predominantly affects the higher frequency null as can be seen in Figure 2.9(a) where the height is varied from 2mm to 4mm while maintaining a constant depth of 7mm. The lower frequency null is predominantly affected by the extrusion depth as seen in Figure 2.9(b) where the depth is varied from 6mm to 8mm while maintaining a constant height of 2.5mm.

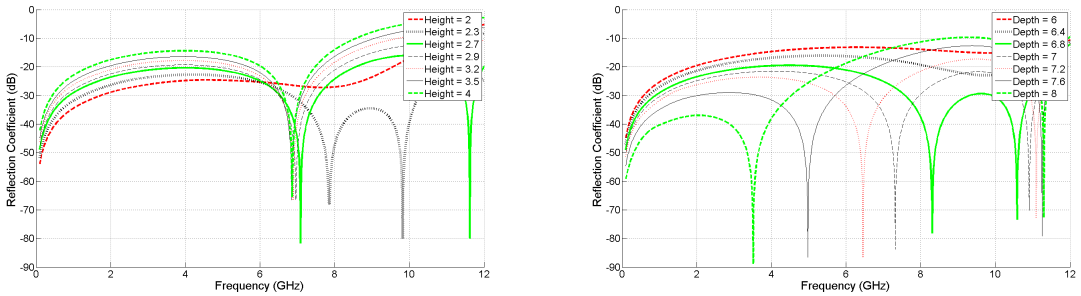

(a) Constant depth of 7mm

(b) Constant height of 2.5mm

Figure 2.9: Reflection coefficient of compensated transition at varying extrusion parameters with constant a) depth and b) height

An compensated transition structure can now be designed for a low reflection coefficient over the required frequency band at different angles of incidence. The height of the extrusion is first varied to obtain the required higher frequency null. A height of 2.5mm was found to be satisfactory for rays perpendicular to the reflector. Maintaining a constant height for all angles of incidence ensures manufacturability while the width is optimised for different angles of incidence. Values for the width in Table 2.3 are acquired through the same procedure used for both the slotted and round transition. It is noted that a relatively small width is required for optimal

coupling with a minimal variation between different angles of incidence. A reflection coefficient of less than $-27dB$ is obtained in Figure 2.10 for the required frequency band for a wide range of angles of incidence.

Angle, θ (degrees)	Width(mm)
90	7
80	7
70	7
60	7
50	7.1
40	7.4

Table 2.3: Compensated transition width necessary for impedance match at different angles of incidence with a height of 2.5mm

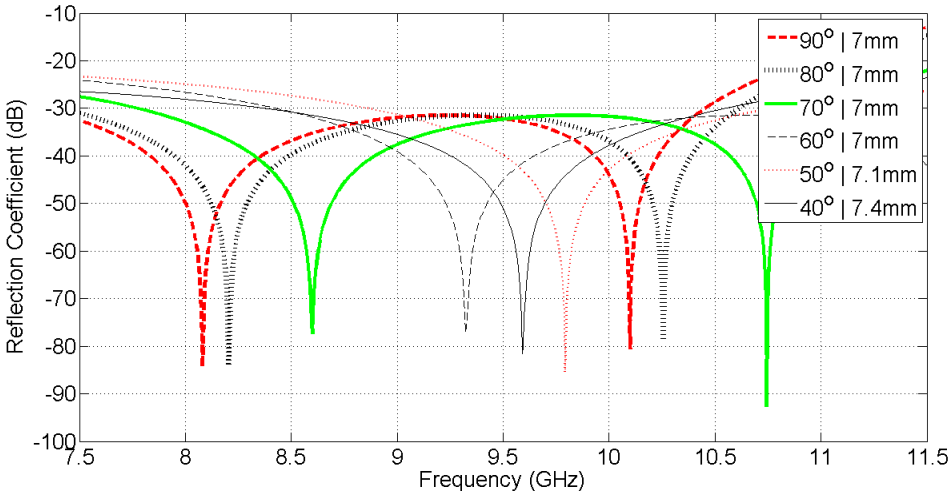

Figure 2.10: Reflection coefficient of compensated transition at different angles of incidence

It is thus found that the compensated transition offers a manufacturable structure to be used in an 180° transition. High coupling is obtained for a large bandwidth. A reflection coefficient of less than $-27dB$ is obtained for incident angles ranging from 90° to 40° through a 20% bandwidth.

2.2.1.4 Transition Curve along Reflector

To acquire the correct gap size for each angle of incidence, a curve is required relative to the reflector to represent the extrusion depth. An arbitrary number of rays are launched from the reflector's focal point and their intersection with the reflector calculated. With the angle of the incident ray and the gradient of the reflector curve at the intersection point known, the angle of incidence can be calculated from equation (A.2).

From Figure 2.11 the length of an incident ray, L, within the bend for a given incident angle, θ, is calculated to determine the gap size required at that intersection point.

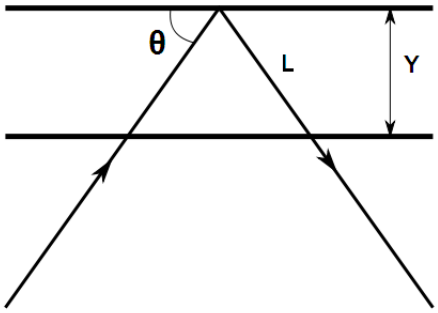

Figure 2.11: Diagram showing the model used to derive the compensated curve for incident rays relative to the reflector

With the required gap size for each angle of incidence calculated, a curve can be synthesised for the compensator transition relative to the reflector as seen in Figure 2.12. Although the length of an incident and reflected ray within the bend at any point on the reflector varies to some degree, this difference is small enough to ignore without degrading the performance. Thus the same curve is used for the top and bottom extrusions.

2.2.2 Feed Structure for Multi-layered Pillbox Antennas

The feed to be used in the double layer pillbox is designed separately. A feed is required that has minimal reflection loss and yields a feasible distribution. The feed has a WR-90 waveguide input port which is tapered to the width of the parabolic reflector. It will be shown that blending the transition between the rectangular input port and the tapered section, Figure 2.13, allows for impedance matching. Further investigation shows that the angle of the taper controls the

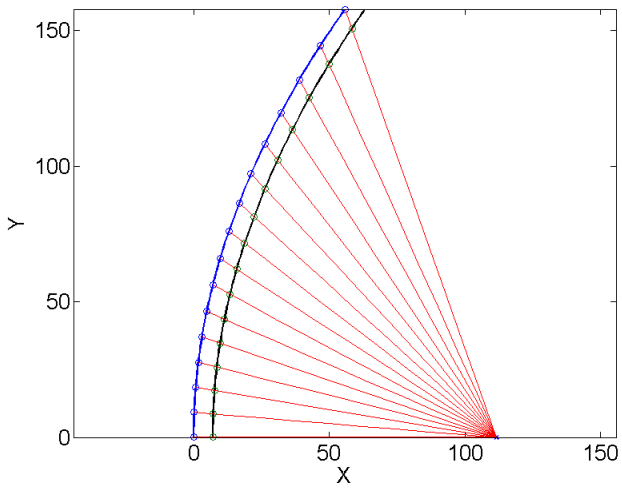

Figure 2.12: Diagram showing the compensator curve required for matching at different angles of incidence

feed distribution.

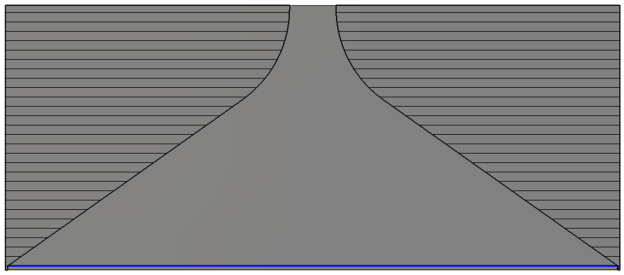

Figure 2.13: Model of the feed used in the Double Layer Pillbox

The radius of the blend is optimised to obtain the reflection coefficient in Figure 2.14 at a radius of 55mm. A reflection coefficient of less than $-30dB$ is obtained for the required frequency band.

It is shown that the angle of the taper is dependent on the focal depth of the parabolic reflector used in the antenna. Varying the focal depth and thus the angle of the taper has an effect on the field distribution that the feed will deliver to the reflector. Keeping in mind that the f/D ratio needs to be larger than 0.25 to keep the feed outside the reflector, the f/D ratio of the feed

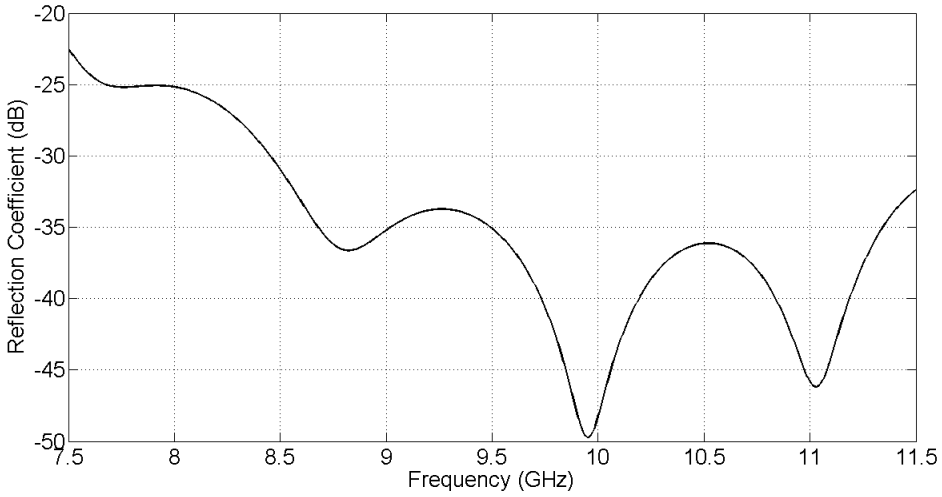

Figure 2.14: Reflection coefficient of the feed used in the Double Layer Pillbox

model is varied and the E-field at centre frequency is obtained through simulation as seen in Figure 2.15. It is noted that a lower f/D ratio concentrates power more to the centre of the feed, whereas the distribution flattens with a higher f/D ratio.

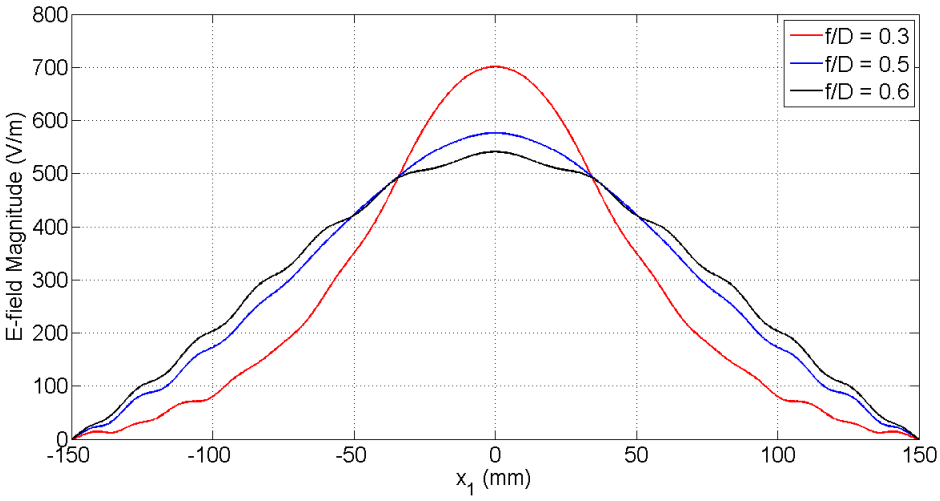

Figure 2.15: E-field distribution of the feed at different f/D ratios

To determine which distribution has the best side-lobe level, a far-field distribution is required. The near-field distribution in Figure 2.15 is transformed to a far-field distribution through the use of a Fourier-Transform [7] which is further discussed in Chapter.4.6.1. The far-field patterns

of the respective distributions are shown in Figure 2.16. It can be seen from the far-field pattern that the lower f/D ratio gives a wider beam-width with a shoulder that could become a side-lobe. It was decided to use a f/D ratio of 0.5, this distribution theoretically yields relative low side-lobes together with a narrow beam-width.

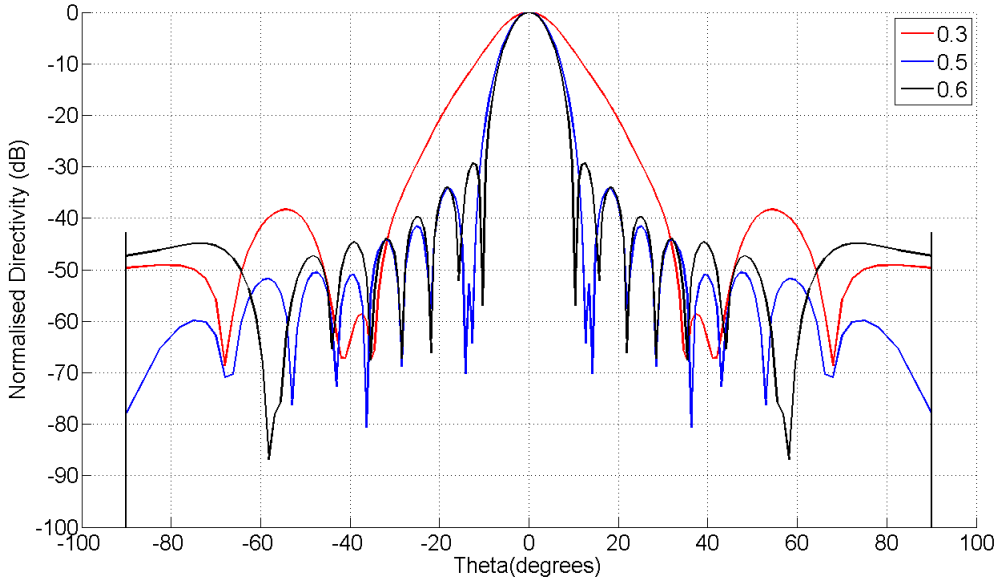

Figure 2.16: Theoretical far-field pattern at different f/D ratios for Double Layer Pillbox feed

2.2.3 Model of Double Layered Pillbox Antenna

The structures designed for the feed and transition are incorporated into a double layer pillbox antenna with a width of 10λ, Figure 2.17. This width is chosen for reasonable simulation time while keeping the antenna size large enough to achieve acceptable results. Due to the large f/D ratio chosen, the feed is positioned within the radiating space in front of the antenna. To reduce scattering from the feed layer, the open space next to the feed is filled with PEC.

Space is not optimally used in this model where the antenna is designed for performance, rather than being compact.

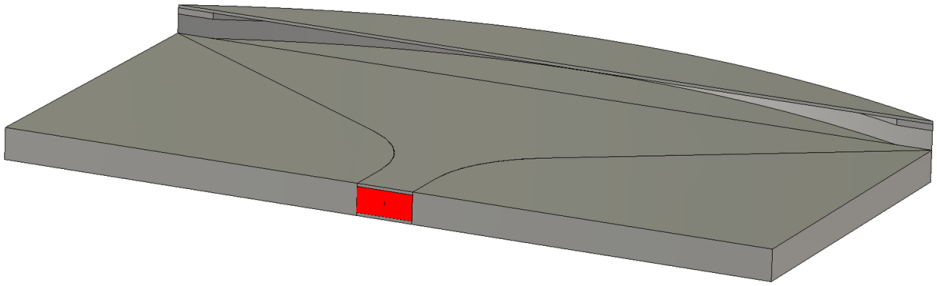

Figure 2.17: Model of Double Layer Pillbox

2.3 Results Obtained for Double Layered Pillbox Antenna

The double layer pillbox is simulated in *CST MWS*. Results obtained for the reflection coefficient are shown in Figure 2.18 whereas the azimuth and elevation far-field patterns are shown in Figure 2.19.

From the reflection coefficient in Figure 2.18(a) it is seen that the antenna is well matched for the required frequency band. A reflection coefficient of $-16.5dB$ is obtained within the stipulated 20% bandwidth. Figure 2.18(b) shows the reflection coefficient in the time domain from where it can be seen that most of the reflection occur at 2.5ns. This is roughly the time it would take the signal to reach the aperture and be reflected back to the input port which indicates that the majority of the reflection coefficient can be attributed to reflections at the aperture.

Side-lobe levels of less than $-30dB$ are obtained from the azimuth far-field gain patterns, Figure 2.19(a), with $-35dB$ side-lobes at centre frequency. The elevation pattern, Figure 2.19(b), shows that the antenna does not have the fan-beam elevation pattern as required. This is due to the feed layer protruding into the radiating space of the antenna. A large back-lobe is present for this model, but is not of any concern at this time as the final antenna configuration will need the antenna to be stacked, which will significantly reduce the back-lobe. If needed, other techniques can be implemented without affecting the antenna performance, such as inserting absorbing material.

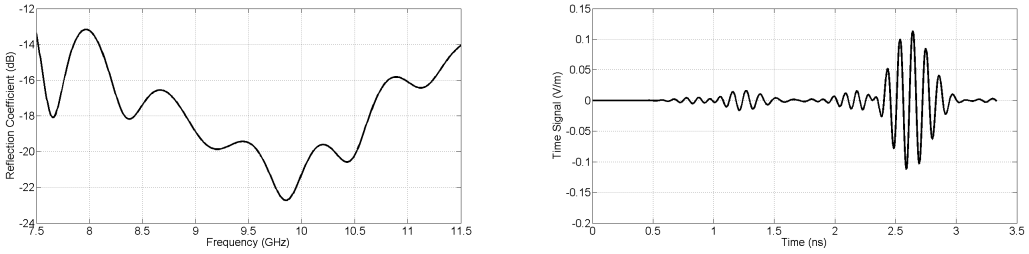

(a) Frequency Domain (b) Time Domain

Figure 2.18: Reflection coefficient of Double Layer Pillbox in a) frequency and b) time domain

2.4 Conclusion on Double Layered Pillbox Antenna

In this section a compensated transition was designed to yield a reflection coefficient of $-27dB$ over the 20% frequency band as well as being manufacturable. The compensated transition was shown to be easily adapted for different angles of incidence and then implemented into the pillbox design.

The feed was designed to yield a feed distribution that allowed the antenna to have a far-field distribution with low-side lobes and an acceptable beam-width. Optimisation allowed for a reflection coefficient of less than $-30dB$ to be obtained for the required frequency band.

Simulated results proved the double layer pillbox to be an improvement on the single layer pillbox. Side-lobes of less than $-30dB$ were obtained in the azimuth plane for the required frequency band. A reflection coefficient of $-16.5dB$ shows that the antenna is well matched for the required bandwidth with the unmatched aperture contributing to the most reflection.

Manufacturability was considered in the design of the transition which should prove to be the most difficult component to manufacture. The parallel plate structure of the antenna should prove to be cost effective and manufacturable.

It was found that the acquired asymmetrical elevation pattern was due to the feed layer protruding into the radiating space. This problem should be solved by folding the feed layer back, creating a triple layer structure.

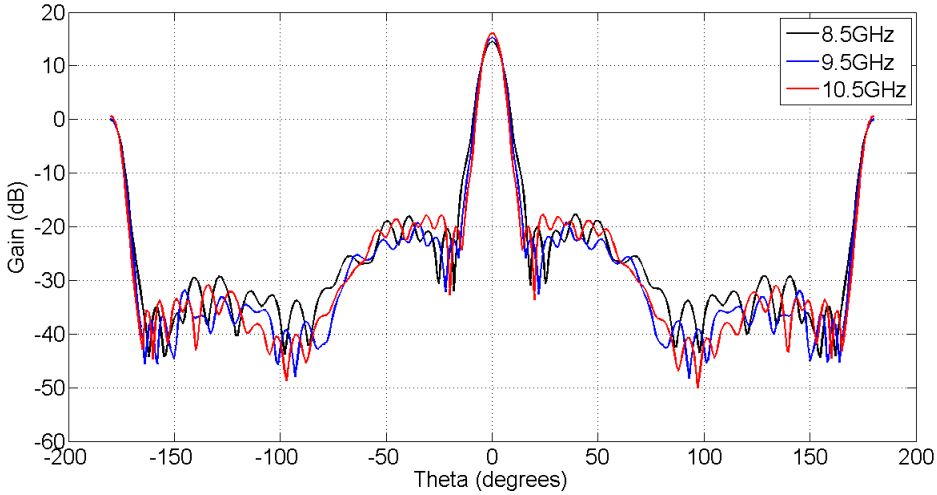

(a) Azimuth Pattern

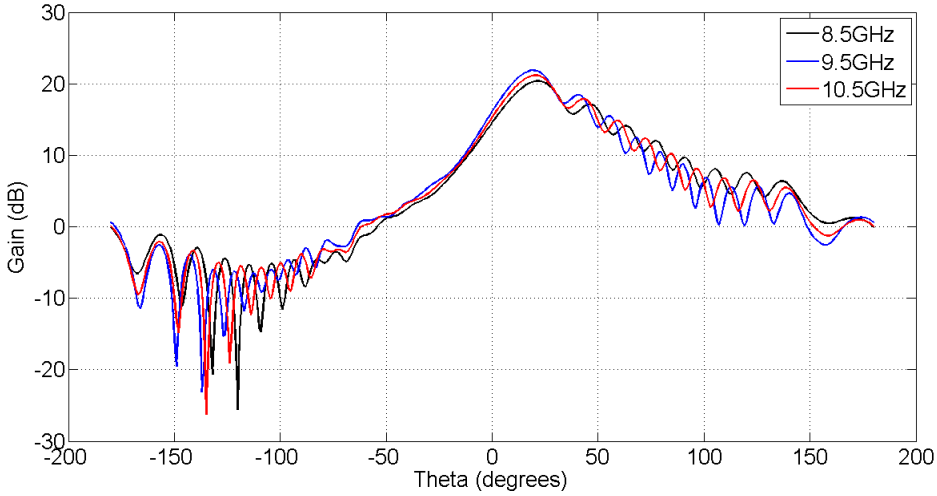

(b) Elevation Pattern

Figure 2.19: Far-field results of Double Layer Pillbox in a) Azimuth and b) Elevation plane

CHAPTER 3
Compensated Transition Transmission Line

This section describes the process of transforming the compensated transition to a transmission line model. The compensated transition is broken into smaller segments which are then individually shown to be accurately transformed to transmission line models. Adding the smaller segments together results in a transmission line model with which the compensated transition can be designed.

Designing the compensated transition requires one to do a series of parameter sweeps. Optimum dimensions for the compensators need to be acquired each time the frequency range, plate spacing or plate thickness changes. This process could be extremely time consuming, taking more time than the rest of the design elements combined.

It is proposed to streamline this part of the design by transforming the compensated transition structure to a transmission line model. This should allow one to obtain the optimal compensator parameters by inserting the required system parameters into a single algorithm.

3.1 Process of Transforming the Compensated Transition to a Transmission Line Model

The compensated transition is broken up into separate waveguide structures where the transmission line parameters can be calculated through equations derived in the Wave Guide Handbook [8].

Due to the symmetry of the structure it can be simplified by using only the one half of the structure as illustrated in Figure 3.1. After a sufficient transmission line model has been obtained for the half structure, the model can simply be mirrored and added to the existing model.

The stepped corner obtained from the half model can further be simplified as a structure comprising of an E-plane corner and a change in height of a rectangular waveguide. Transmission line models for both these structures can be obtained from the Wave Guide Handbook[8] but some deviation will occur due to the close proximity of the two sections.

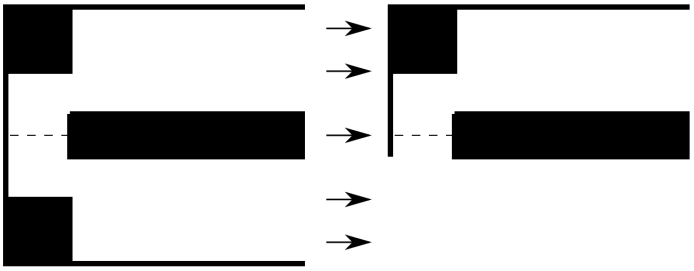

Figure 3.1: Simplification due to symmetry in compensated transition

3.1.1 E-plane Corner Transmission Line

The E-plane corner consists of a rectangular waveguide with a 90° bend as shown in Figure 3.2. With a reference position at T' and a plate spacing of b used, the transmission line model in Figure 3.3 can be used to represent the E-plane corner.

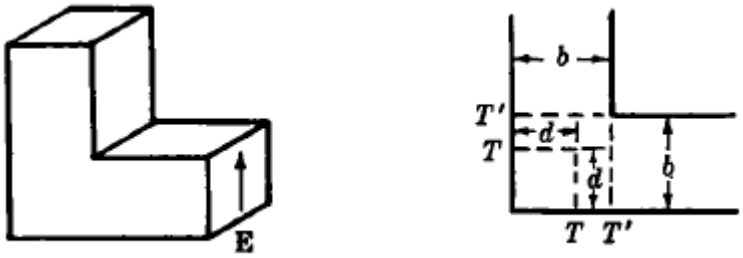

Figure 3.2: Rectangular E-plane corner diagram, [8]

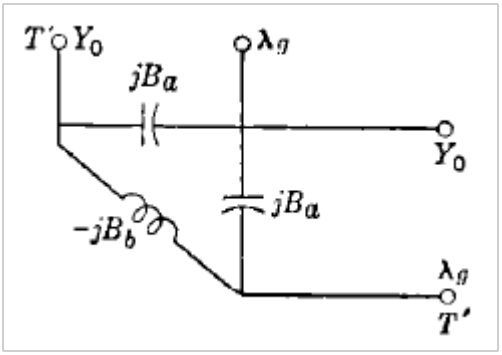

Figure 3.3: Rectangular E-plane corner transmission line model, [8]

Values for the inductance, B_b, and capacitance, B_a, can be obtained for different values of b through the use of equations derived in [8]. The inductance is first calculated by substituting equations (3.3) to (3.7) in equation (3.1) to obtain a value for B_a. A value for the capacitance can then be calculated with equation (3.2).

$$\frac{B_a}{Y_0} = \frac{2b}{\lambda_g}\left\{-\frac{cot(\pi x)}{x} + \frac{1}{\pi x^2} + \frac{\pi}{6} - ln(2) - \left[\frac{A_0 e^{-\frac{\pi}{2}} + (A_1 - A_2)e^{-\pi} + (1+5e^{-\pi})\frac{A_0^2}{16}}{1-(1+5e^{-\pi})\left(\frac{A_1-A_2}{4}\right)}\right]\right\} \tag{3.1}$$

$$\frac{2B_b}{Y_0} - \frac{B_a}{Y_0} = \frac{\lambda_g}{2\pi b}\left\{1 + \pi x cot(\pi x) - \pi x^2\left[5ln(2) - \frac{7\pi}{6} - 8\sum_{n=1}^{\infty}\frac{1}{n(e^{2\pi n}-1)}\right]\right.$$
$$\left. + \pi x^2\left[\frac{A_0' e^{-\frac{\pi}{2}} - (A_1 + A_2)e^{-\pi} + (1-3e^{-\pi})\frac{A_0'^2}{16}}{1+(1-3e^{-\pi})\frac{A_1+A_2}{4}}\right]\right\} \tag{3.2}$$

$$x = \frac{2b}{\lambda_g} \tag{3.3}$$

$$A_0 = \frac{4}{\pi}\frac{x^2}{1-x^2} \tag{3.4}$$

$$A_0' = A_0 - \frac{8}{sinh(\pi)} \tag{3.5}$$

$$A_1 = \frac{1}{\pi}\frac{x^2}{1-0.5x^2} \tag{3.6}$$

$$A_2 = 4\left[\frac{1}{\sqrt{1-x^2}(1-e^{-2\pi\sqrt{1-x^2}})} - \frac{1}{1-e^{-2\pi}}\right] \tag{3.7}$$

The capacitance and inductance for the structure is then calculated from the equations below.

$$C = \frac{B_a}{2\pi f} \tag{3.8}$$

$$L = \frac{1}{B_b 2\pi f} \tag{3.9}$$

A transmission line model is simulated using the diagram in Figure 3.4 using *AWR* with the inductance and capacitance values in Table.3.1 and an input and output impedance of 377Ω. These values were calculated at a centre frequency of $10GHz$. The resulting reflection coefficient is shown in Figure 3.5 where it is compared to the corresponding *CST MWS* simulated results.

Figure 3.5 shows good correlation between the simulated results and the transmission line model, showing that the calculated values for the inductance and capacitance are accurate enough to represent the model.

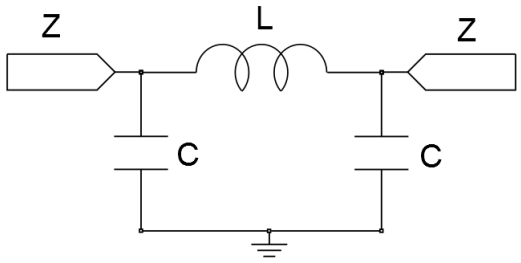

Figure 3.4: Rectangular E-plane corner lumped element transmission line model

b(mm)	*C(nF)*	*L(uH)*
5	0.01322	0.006369
8	0.02400	0.01051
11	0.04299	0.01579

Table 3.1: Inductance and capacitance values required to represent models with different plate spacing

3.1.2 E-plane Step Transmission Line

The E-plane step model consists of a rectangular waveguide with a step in its height as can be seen in Figure 3.6. The input height of b is reduced to b' with a reference position located at T. The equivalent transmission line model of the E-plane step is also found in Figure 3.6. The output impedance of the circuit is calculated through the use if equation (3.10) and a value for B is calculated using equation (3.11) or (3.12), depending on the b'/b ratio.

$$\frac{Y_0}{Y_0'} = \frac{b'}{b} = \alpha = 1 - \delta \tag{3.10}$$

$$\frac{B}{Y_0} \approx \frac{2b}{\lambda_g}\left[ln\left(\frac{2.718}{4\alpha}\right) + \frac{\alpha^2}{3} + \frac{1}{2}\left(\frac{b}{\lambda_g}\right)^2 (1-\alpha^2)^4\right], \alpha << 1 \tag{3.11}$$

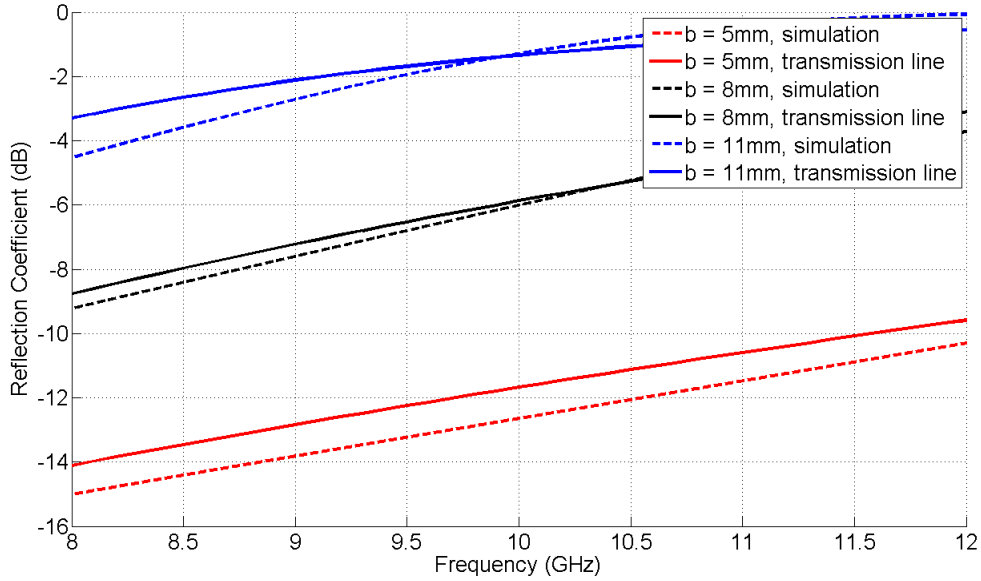

Figure 3.5: Reflection coefficient of E-plane corner calculated with *CST MWS* and transmission line theory

$$\frac{B}{Y_0} \approx \frac{2b}{\lambda_g}\left(\frac{\delta}{2}\right)^2\left[\frac{2ln\left(\frac{2}{\delta}\right)}{1-\delta}+1+\frac{17}{16}\left(\frac{b}{\lambda_g}\right)^2\right], \delta << 1 \tag{3.12}$$

Values are calculated for the output impedance as well as the capacitance at a frequency of $10GHz$ for a stepped model with an initial height of 11mm which is then stepped to values of 4mm, 6mm and 8mm. These values are used in the transmission line model shown in Figure 3.7. Table 3.2 shows the computed values which are used to calculate the reflection coefficient shown in Figure 3.8. Reasonably good correlation is found between the calculated and simulated results shown in Figure 3.8. This proves that this transmission line model is a good approximation for a stepped E-plane rectangular waveguide.

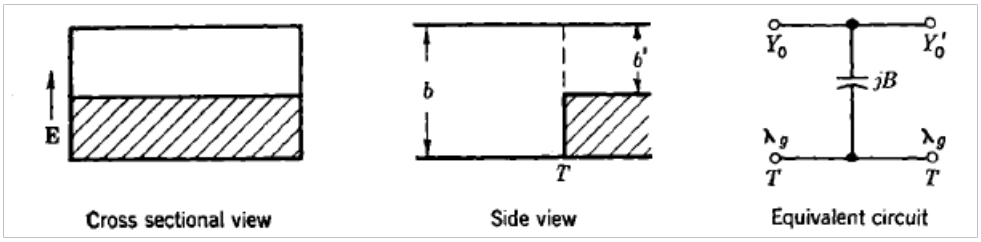

Figure 3.6: Stepped rectangular waveguide diagram, [8]

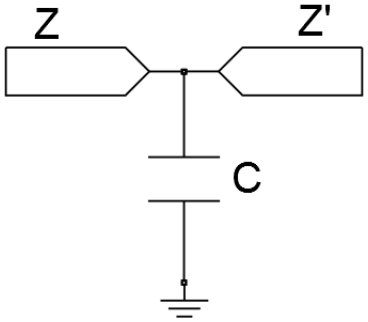

Figure 3.7: Transmission line model of stepped E-plane rectangular waveguide

$b'(mm)$	$C(nF)$	$Z'(\Omega)$
4	0.05092	136.993
6	0.02242	205.489
8	0.00812	273.985

Table 3.2: Output impedance and capacitance values required to represent stepped rectangular waveguide models with different step sizes

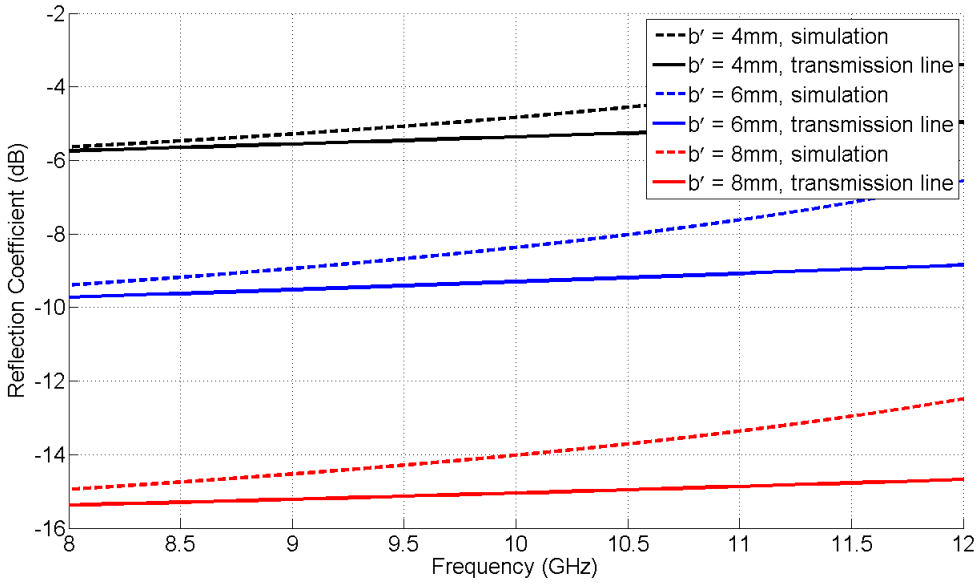

Figure 3.8: Reflection coefficient of stepped E-plane rectangular waveguide with b = 11mm, calculated with *CST MWS* and transmission line theory

3.1.3 Stepped E-plane Corner Transmission Line

The stepped E-plane corner is formed by adding a stepped waveguide structure to an E-plane bend as shown in Figure 3.9. The structure is stepped from an initial height, h, to a smaller height, b, and then bent 90°. Figure 3.10 shows the equivalent circuit model of the structure which is essentially the combined circuit models of the stepped waveguide and E-plane corner.

Values for C_s and Z_2 are calculated for a stepped waveguide, stepped from h to b. C_a and L are calculated for an E-plane corner with a plate spacing of b. Due to the close proximity of the two structures to each other, the accuracy of the transmission line formulas decreases. To compensate for this, the values for the inductance and capacitance in the corner need to be adapted. Through the use of multiple parameter sweeps it was determined that a good estimate to the change in capacitance and inductance is a 7% decrease in the inductance, L, and an extra capacitance, C_e, with a value of 10% of the combined value of C_s and C_a.

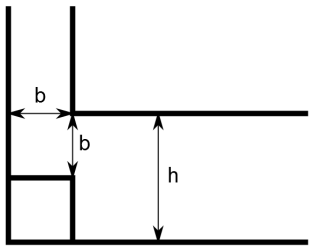

Figure 3.9: Stepped E-plane corner model

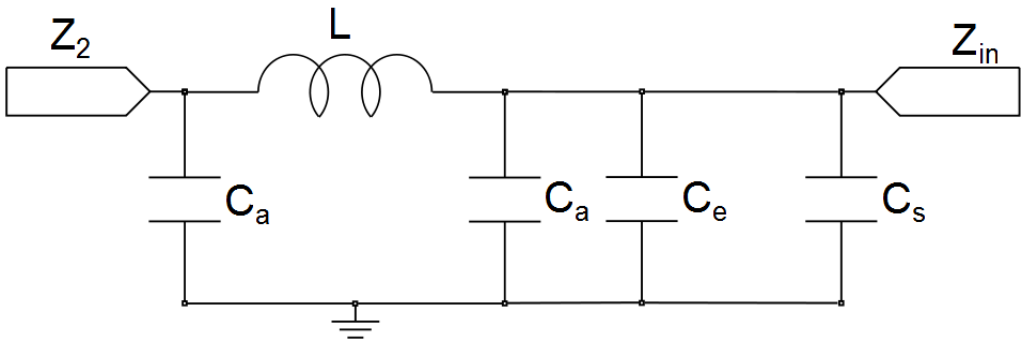

Figure 3.10: Transmission line model of stepped E-plane corner

Table 3.3 shows values calculated for the elements in Figure 3.10 for different values of h and

b. The reflection coefficient calculated for the transmission line model is compared to the *CST* results in Figure 3.11. A good correlation can be seen in Figure 3.11 between the results which shows that the equivalent circuit is an accurate representation of the stepped E-plane corner model.

$h(mm)$	$b(mm)$	$C_s(nF)$	$C_a(nF)$	$C_e(nF)$	$L(uF)$	$Z_2(\Omega)$
11	7	0.01419	0.03132	0.004551	0.005369	239.73
11	9	0.00381	0.03527	0.003907	0.009166	308.23
10	6.5	0.01179	0.02786	0.003965	0.005065	244.87
8.6	5.5	0.01056	0.02309	0.003364	0.004181	240.93

Table 3.3: Element values required to represent stepped corner models with different dimensions

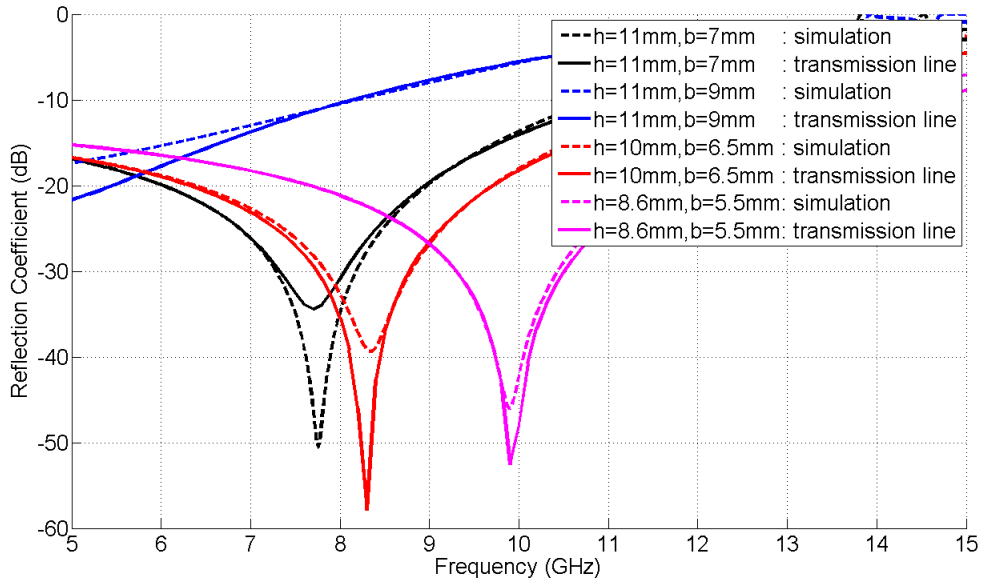

Figure 3.11: Reflection coefficient of stepped E-plane corner, calculated with *CST MWS* and transmission line theory

3.1.4 Full Stepped Bend Transmission Line

The mirror image of the stepped corner is attached to the original structure with a spacing of d between them, Figure 3.12. The equivalent circuit model, Figure 3.13, is obtained by adding two stepped corner models with a transmission line connecting them. This connecting transmission

line represents the spacing between the stepped corner structures.

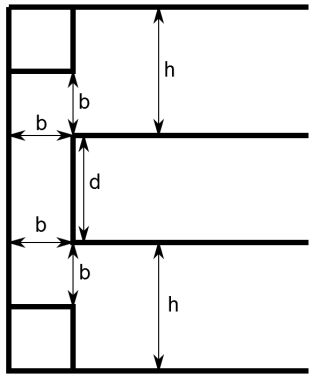

Figure 3.12: Full stepped bend model

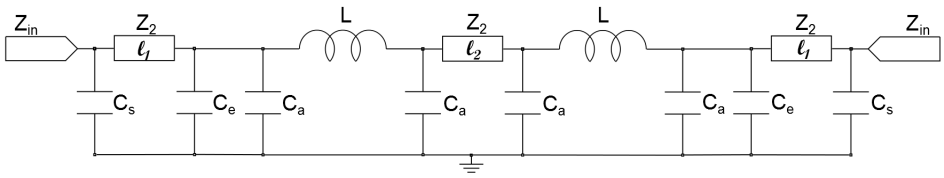

Figure 3.13: Transmission line model of full stepped bend

Values for the elements in Figure 3.13 are calculated using the method described for the stepped corner model. The effective length of the transmission line, l_2, is determined through parameter sweeps as being 70% of d. A model with dimensions of $h = 12mm$ and $b = 8mm$ is chosen to evaluate the effectiveness of the full stepped bend equivalent circuit. These dimensions were chosen as it delivers a reflection coefficient with two nulls located within the $5GHz$ to $12GHz$ range. Table 3.4 shows the calculated element values.

Figure 3.14 shows the reflection coefficient of the full stepped bend with constant $h = 12mm$ and $b = 8mm$ while d is varied from $1mm$ to $8mm$. The reflection coefficient obtained from the equivalent circuit correlates relatively well with the simulated results with the nulls varying by a few MHz. This result shows that the derived equivalent circuit is a good representation for the full stepped bend model.

$h(mm)$	$b(mm)$	$C_s(nF)$	$C_a(nF)$	$C_e(nF)$	$L(uF)$	$Z_2(\Omega)$
12	8	0.01325	0.036004	0.004925	0.006515	251.15

Table 3.4: Element values required to represent full stepped bend

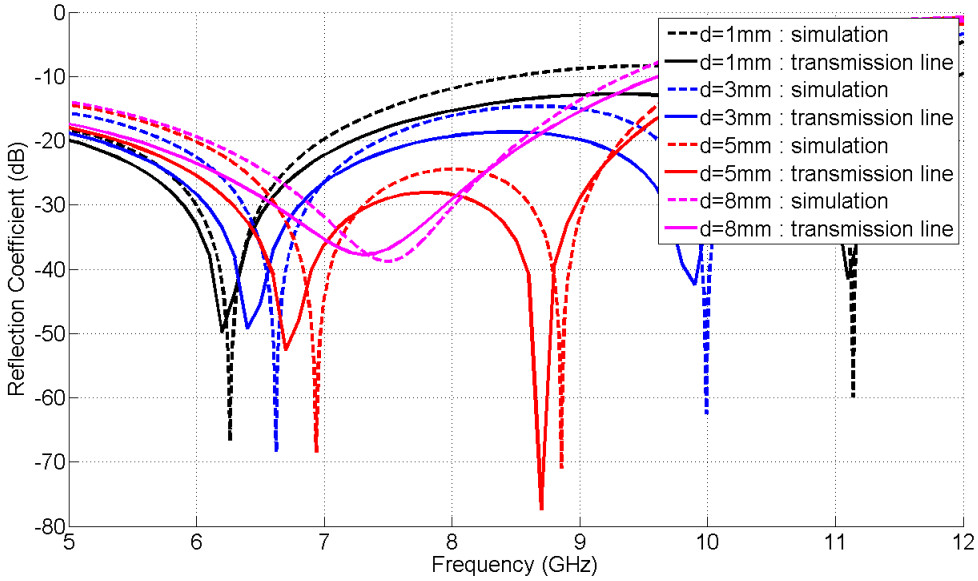

Figure 3.14: Reflection coefficient of full stepped bend with h = 12mm and b = 8mm, calculated with *CST MWS* and transmission line theory

3.2 Conclusion on the Transformation of the Compensated Transition to a Transmission Line Model

A transmission line model for the full stepped bend was obtained together with expressions relating the physical dimensions of the transition to the lumped elements of the transmission line model. It was shown that a transition can be relatively accurately modelled as a transmission line.

Expressions still need to be obtained for a model where the gap size is different to the distance between the extrusion and parallel plate. If these expressions are obtained, the compensated transition could be modelled as a transmission line.

CHAPTER 4
Triple Layer Pillbox Antenna

4.1 Introduction to Triple Layer Pillbox Antennas

In this section a triple layer pillbox antenna is designed by folding the feed layer of the double layer pillbox antenna back, removing the feed layer from the radiating space in front of the aperture. The removal of the feed from above the aperture allows for an impedance matching structure to be designed and implemented at the aperture, this structure is shown through simulation to be effective. A triple layer pillbox antenna is then designed and simulated. Simulated results show that the designed triple layer pillbox yields an adequate radiation pattern and reflection coefficient over the required bandwidth. Further verification of the validity of simulated results and the manufacturability of the proposed structure is done through the comparison of results obtained from different solvers, together with the use of parameter sweeps. After confirmation is done to establish the validity of the design, the construction and measurement process is discussed. It is shown that measured results agree well with simulated results, confirming that the triple layer pillbox conforms to the set antenna requirements.

The idea of a triple layer pillbox originated from Rotman, [4]. In this article a second bend was inserted into a double layer pillbox structure to allow for a second, auxiliary, reflector. This second reflector can then be mechanically moved with the feed to allow for scanning. This concept was adapted for the required specifications by folding back the feed layer of the double layer pillbox, creating a second, straight, bend as seen in Figure 4.1. This removes the feed layer from the radiating space in front of the aperture, making the structure more compact and symmetrical at its aperture. The input port for the antenna is now located at the back of the structure which makes feeding it easier.

An additional benefit to removing the feed layer from the radiating space is that a structure can be inserted at the aperture for more effective impedance matching. The aperture compensator is designed using the principles of the compensated transition by placing rectangular extrusions above and below the aperture. It is shown through simulated results that a reflection coefficient of less than $-30dB$ over the 20% bandwidth is obtained for this structure.

Using the described techniques a small triple layer pillbox is designed for a width of 10λ which is then enlarged to 2.4m for a full scale model. Simulated results for both antennas show azimuth

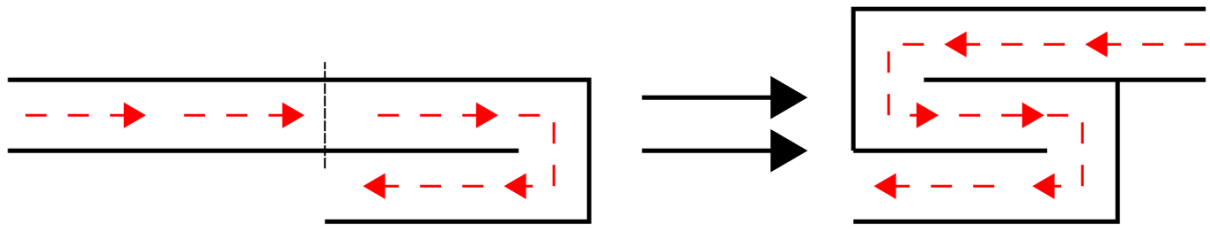

Figure 4.1: Diagram illustrating the conversion from a Double Layer Pillbox to a Triple Layer Pillbox

side-lobes of less than $-30dB$ together with a reflection coefficient of less than $-23dB$ over the required 20% frequency range. It is further shown that the triple layer pillbox yields the required symmetrical fan-beam elevation pattern.

Verification is done to determine whether obtained results are accurate and if the structure can be manufactured to obtain the simulated results. Results obtained from *CST* simulations are compared to results from *FEKO* and shown to agree down to $-25dB$ down the main beam which verifies the concept of using a triple layer pillbox antenna. It is shown that the effect of plate warping into the layers of the antenna, together with an offset of the plates into the transition areas degrades antenna performance, demonstrating that care need to be taken during the construction of these structures.

Construction is accomplished using stacked laser-cut aluminium sheets, this allows for a relatively cheap design which is easily assembled. The design of a coaxial cable to waveguide transformer is briefly discussed to be used to feed the manufactured model.

Due to the size of the antenna, a near-field measurement needs to be done. The theory of near to far-field transformation is discussed, followed by the theory of probe compensation. Different anechoic chamber configurations are then inspected to determine the optimal setup for measurements. Measured results show the antenna to yield $-27dB$ side-lobes across the 20% bandwidth.

4.2 Design Procedure for Triple Layered Pillbox Antennas

The triple layer pillbox is designed using the model obtained for the double layer pillbox in Chapter 2. The feed is folded back to create an extra layer and connected to the antenna with the addition of an extra bend. An aperture compensator structure is further implemented at the aperture of the antenna.

The feed used in the double layer pillbox has a taper of 35°. Using the same feed and a flat reflector surface at the new bend means that, from Table 2.3, no compensation is necessary for different angles of incidence. Extrusions compensated for 90° incidence is thus used for the entire bend.

A simple design for a structure at the aperture is needed for impedance matching. It was decided to use the same principles as were used for the compensated transition to design an aperture compensator. The aperture compensator is designed to maintain manufacturability by using rectangular extrusions positioned above and below the aperture.

4.2.1 Aperture Compensator Design

The aperture compensator consists of two extrusions located above and below the aperture as in Figure 4.2. Symmetry is maintained to insure a symmetrical elevation pattern when implemented into the antenna structure. The extrusions have three variables available for adaption; offset from the aperture, height and depth. It is assumed that all incoming rays will be perpendicular to the aperture and thus no compensation needs to be done for different angles of incidence.

The designed aperture compensator is well matched as seen in Figure 4.3. A reflection coefficient of $-30dB$ is obtained for the required frequency range. This result compares well to the reflection coefficients obtained from the other designed structures, resulting in that the aperture compensator would not degrade the overall performance of the antenna.

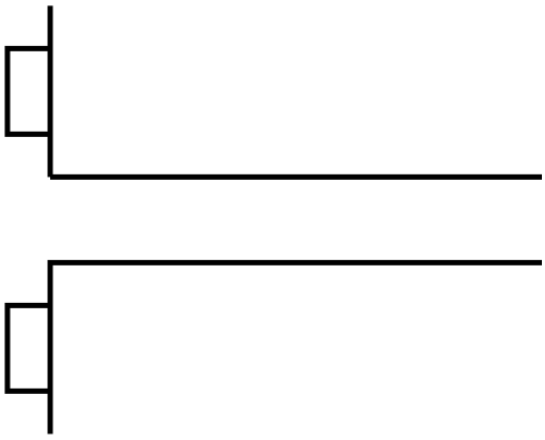

Figure 4.2: Diagram illustrating the aperture compensator structure

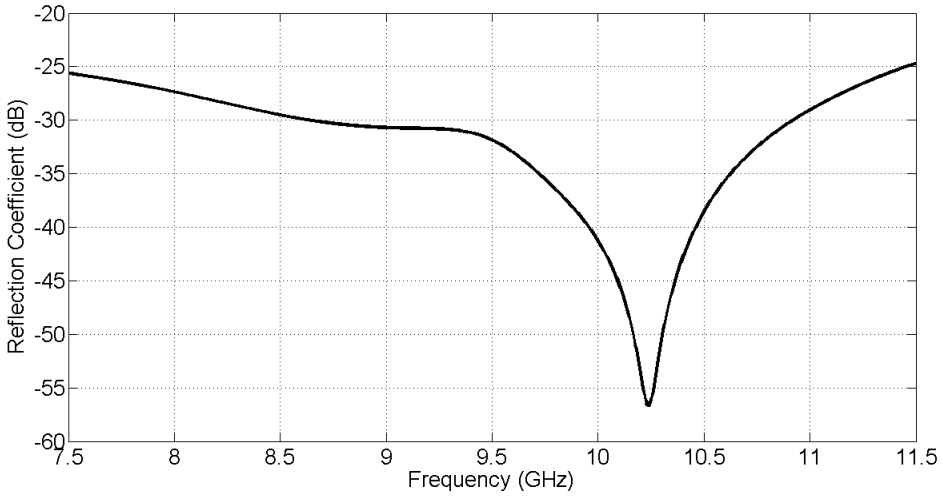

Figure 4.3: Reflection coefficient of aperture compensator

4.2.2 Triple Layer Pillbox Structure

The triple layer pillbox is made up of three layers, a feed layer, a middle layer and an aperture layer. The feed layer contains the feed structure and is connected to the middle layer through a bend with a straight reflector. The middle layer connects the feed layer to the aperture layer. A curved bend connects the middle layer to the aperture layer. The aperture layer terminates at the antenna's aperture. Aperture compensators are placed at the aperture to match the antenna to free space. A model of the triple layer pillbox, cut along the axis of symmetry, is shown in Figure 4.4.

The double layer pillbox antenna designed in Chapter 2 is used to design a triple layer pillbox antenna with a 10λ width. It is noted that this antenna is significantly more compact than the double layer pillbox was. A large f/D ratio still results in an ineffective use of space due to the large feed layer, but could easily be reduced to meet dimensional restraints.

4.3 Simulated Results for the Triple Layer Pillbox Antenna

4.3.1 Simulated Results for Small Triple Layer Pillbox Antenna

The designed small triple layer pillbox antenna with a 10λ width is simulated using *CST MWS*. Resulting far-fields are shown in Figure 4.5 with the reflection coefficient shown in Figure 4.6. Further inspection of the antenna's performance is done through the aperture fields shown in Figure 4.7.

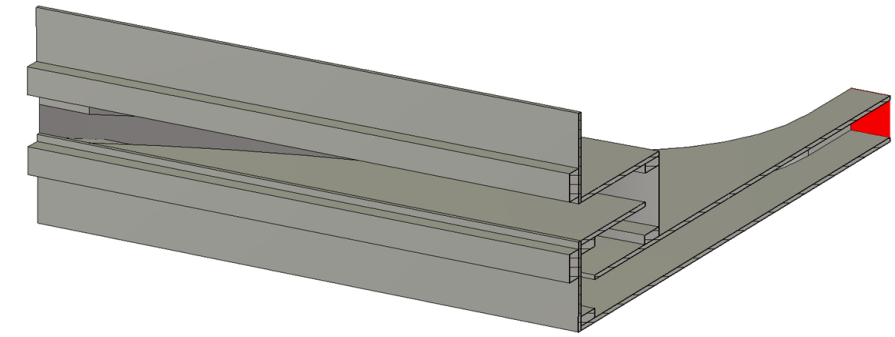

Figure 4.4: Model of Triple Layer Pillbox with cut plane

From Figure 4.5(a) a side-lobe level of at least $-30dB$ is obtained for the frequency band in the azimuth plane. This shows that the addition of an extra bend does not deteriorate the performance of the antenna. Symmetrical far-field distributions are obtained in the elevation pattern in Figure 4.5(b). Higher frequencies tend to have a lower beam-width due to higher gain. This can be solved through the use of frequency dependant structures at the aperture, but stacking multiple antennas should also solve the problem. A gain of $18.3dBi$ can also be seen from the far-field pattern

The reflection coefficient of the antenna in Figure 4.6 shows that the antenna is well matched with a reflection coefficient of less than $-23dB$ through the required frequency band. This shows that the extra inserted bend is well matched and that the aperture compensator works.

The phase and magnitude distributions of the E-fields are taken at the aperture of the antenna, Figure 4.7. The phase distribution, Figure 4.7(a), is flat along the length of the aperture as is expected from a parabolic reflector with a feed located at its focal point. The ripple present on the magnitude distribution causes degradation in the side-lobe levels and is presumed to be caused by internal scattering and reflections.

4.3.2 Simulated Results for Full Sized Triple Layer Pillbox Antenna

Design requirements require an antenna to be designed to adhere to the stipulated dimensional restraints. These restraints require that a much larger antenna with a 2.4m width be designed whose depth does not exceed 0.6m. Using the techniques discussed above an antenna is designed with an aperture width of 2.4m. The f/D ratio is chosen for optimal use of the given space as

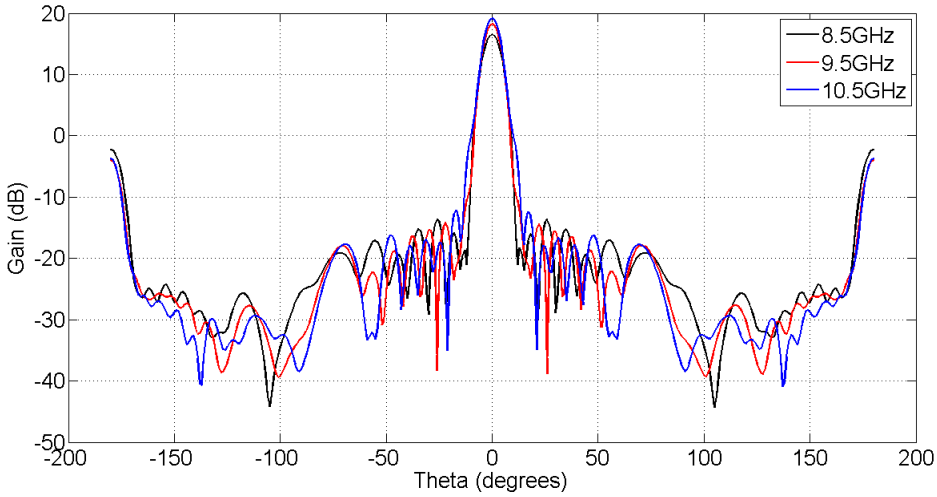

(a) Azimuth Pattern

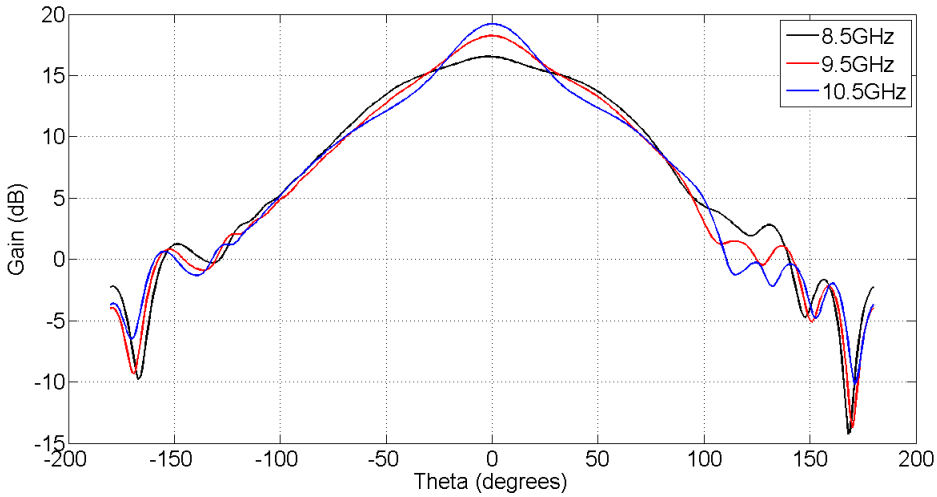

(b) Elevation Pattern

Figure 4.5: Far-field results of Triple Layer Pillbox in a) Azimuth and b) Elevation plane

$1/\sqrt{8}$.

The azimuth far-field pattern in Figure 4.8 shows side-lobe levels of $-28dB$ and a gain of $27dBi$. This is higher than obtained for the smaller antenna, but could be due to the smaller f/D ratio chosen. Little change is detected in the elevation pattern in Figure 4.9 which remains acceptable.

A higher reflection loss is obtained for the larger antenna with a reflection coefficient of $-20dB$, shown in Figure 4.10. This degradation is mostly due to the enlarged structure which causes

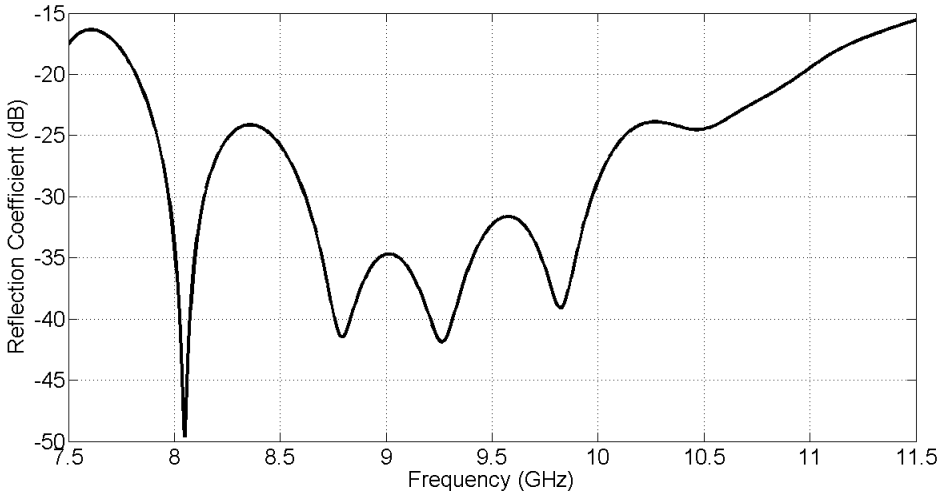

Figure 4.6: Reflection coefficient of Triple Layer Pillbox

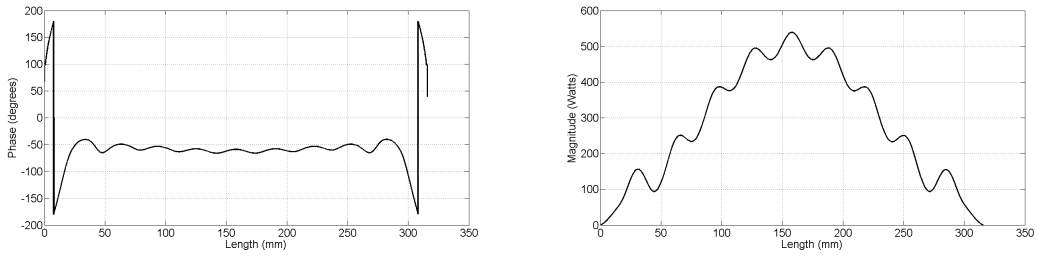

(a) Aperture phase distribution

(b) Aperture magnitude distribution

Figure 4.7: Aperture a) phase and b) magnitude distribution of Triple Layer Pillbox

extra internal reflections and thus more energy to be reflected back into the input port.

The antenna performs well with side-lobes at $-28dB$, a gain of $27dBi$ and a reflection coefficient of $-20dB$ for the required frequency band. The antenna dimensions are to specification with the depth and height well beneath the maximum allowed size.

Figure 4.11 shows the $3dB$ beam-width of the azimuth far-field pattern. The beam-width is less than 1° as required by specification, but can be enlarged by designing a smaller antenna if required.

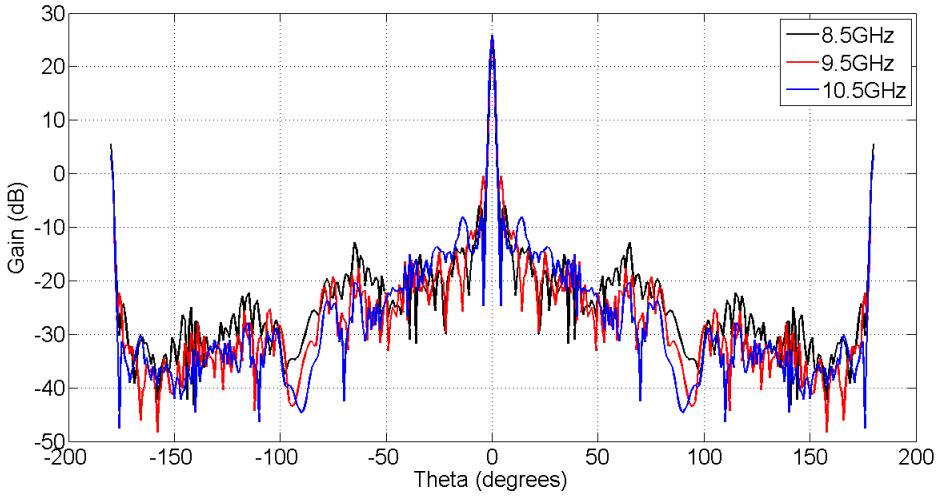

Figure 4.8: Far-field results of large Triple Layer Pillbox in azimuth plane

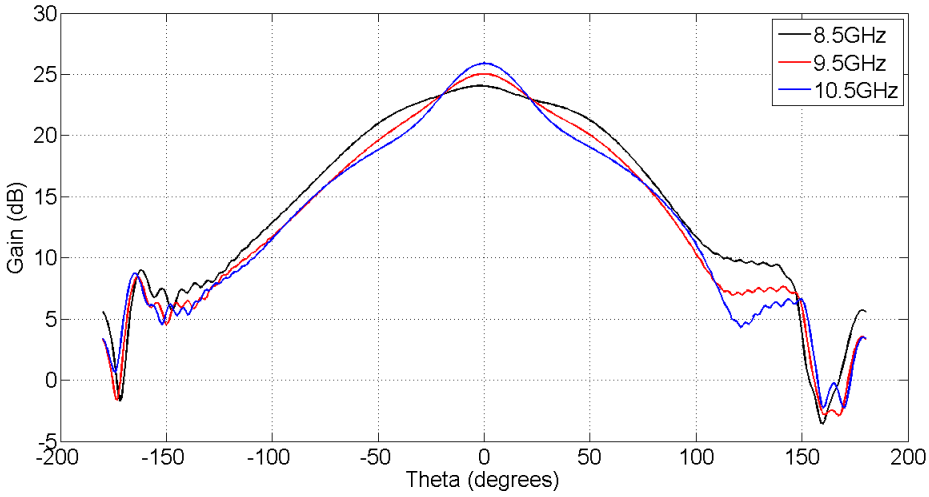

Figure 4.9: Far-field results of large Triple Layer Pillbox in elevation plane

4.3.3 Conclusion on Simulated Results of Triple Layered Pillbox Antenna

The designed triple layer pillbox yields simulated results equal to that of the double layer pillbox with improvements in the elevation pattern and reflection losses. Simulated side-lobe levels of less than $-30dB$ were obtained, together with a reflection coefficient of less than $-20dB$ over the frequency band. Results obtained for the full scale antenna show that although the performance is degraded to some extent, adequate performance is still obtained with $-28dB$ side-lobes and a reflection coefficient of less than $-20dB$.

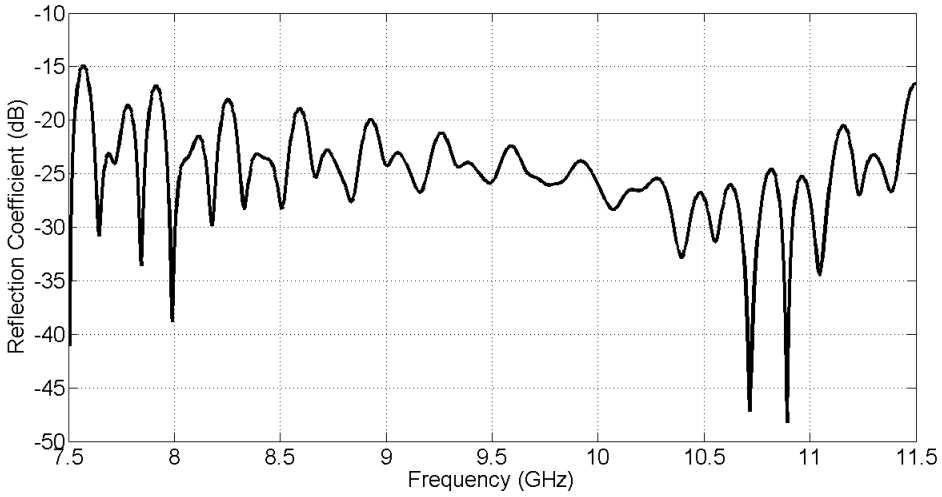

Figure 4.10: Reflection coefficient of large Triple Layer Pillbox

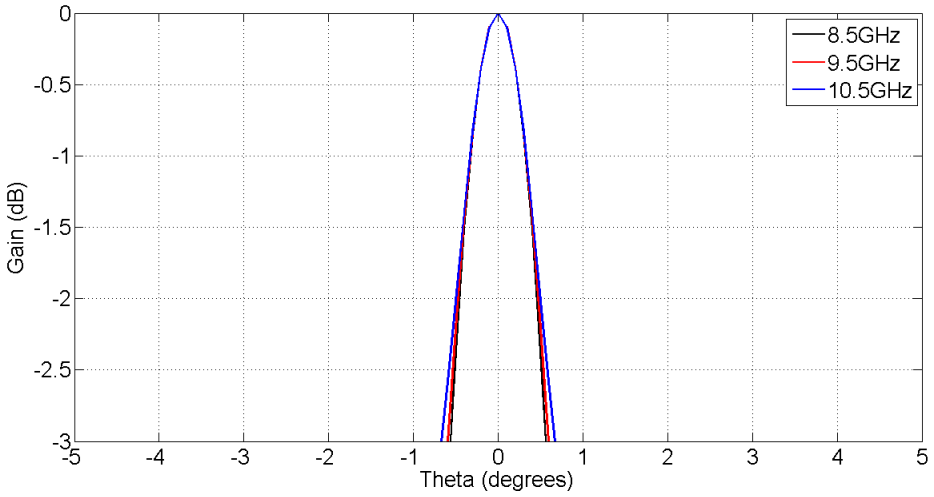

Figure 4.11: Beam-width of large Triple Layer Pillbox

The addition of an extra bend allows for a greater f/D ratio without affecting the elevation pattern. When considering dimensional restraints, a lower f/D ratio is considered to make optimal use of the given space for a more effective antenna structure.

Aperture compensators give the antenna a good impedance match at the aperture. This structure is designed to be easily manufacturable as it consists of two rectangular extrusions attached to the aperture.

From the performance results obtained from simulation and the mechanical structure of the

antenna, the triple layer pillbox promises to have high performance while having a structure that could be produced at low cost.

4.4 Simulated Results Verification and Manufacturing Tolerance of Triple Layer Pillbox Antenna

To verify whether the designed model can be built to yield the results obtained through simulation, the tolerance of the structure needs to be determined and the simulation results verified.

Verifying simulation results is done through the use of a different solver. *FEKO* uses different simulation techniques than *CST* and is used to verify the obtained results. The designed model is simplified and simulated using both *CST* and *FEKO*, the results are then compared for verification.

The tolerance of the structure is determined through observing changes in the side-lobe levels and reflection coefficient of the antenna with variation of suspect system parameters. The effect of plate warping is inspected through the addition of extrusions on the parallel plates of the antenna. Parameters such as the offset of the aperture extrusions from the aperture and the position of plates within the transition structures are also believed to be probable problems during manufacture and inspected.

4.4.1 Verification of Triple Layer Pillbox Simulated Results

The designed 10λ wide triple layer pillbox model is exported to *FEKO* for comparison. Due to *FEKO*'s meshing algorithm, the plate thickness of all plates in the *CST* model is reduced to zero to reduce the number of mesh cells to a realistic value.

Results obtained in *FEKO* and *CST* are compared in Figure 4.12 at the centre frequency and edge frequencies. Comparison shows a good correlation in results down to $-25dB$ on normalised results. Resource limitations in computing power leads to poor meshing in *FEKO* which could explain the difference in results.

4.4.2 Manufacturing Tolerance of Triple Layer Pillbox

The tolerance of the structure needs to be obtained to determine whether the antenna is manufacturable and where extra care need to be taken in the manufacturing process to achieve desirable results.

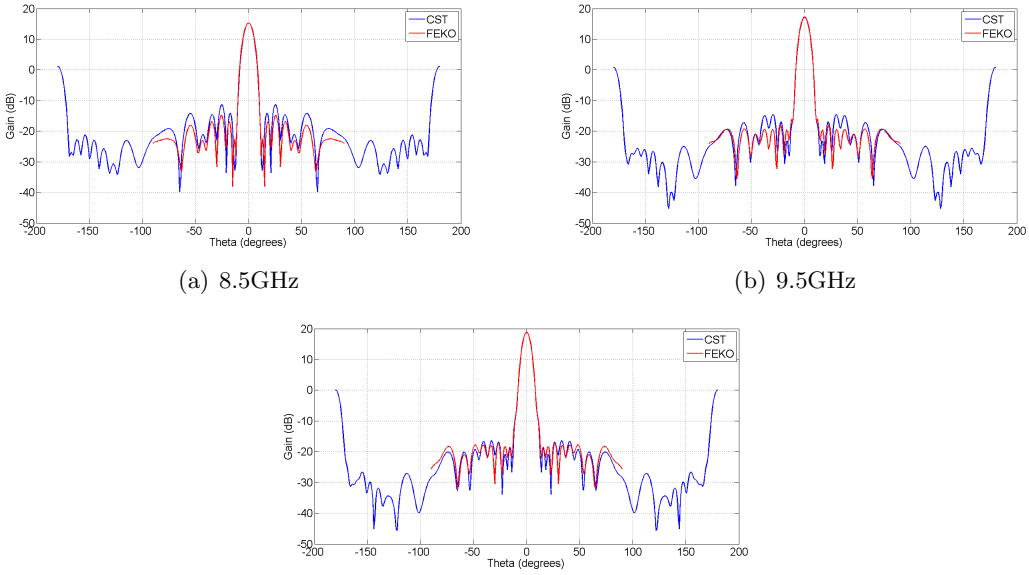

(a) 8.5GHz

(b) 9.5GHz

(c) 10.5GHz

Figure 4.12: Far-field results of Triple Layer Pillbox from *CST* and *FEKO*

Structures which may possibly be difficult to manufacture to the precise designed values are identified as the gap sizes in the bends as well as the offset values of the aperture compensators. Another big concern is the effect that the warping of the parallel plates could have on performance.

Due to the concern of warping plates, which is more prone in larger structures, it was decided to design a larger antenna on which to do the tolerance analysis. An antenna with an aperture width of 800mm is designed through the design procedure discussed in Chapter 4.

4.4.2.1 Parametric Tolerance of Triple Layer Pillbox Structure

Gap sizes may be difficult to manufacture to the designed values due to the precision to which it is designed. The middle plates may be difficult to position within the bend to this degree of accuracy, especially in the reflector bend where there is limited support for the middle plate. To determine the effect of miss alignment both plates are moved individually within the bend to vary the individual gap sizes.

Depending on the mechanical design model, the positioning of the aperture compensators could also prove difficult. The offset of the compensators are varied independently to simulate both the effect of asymmetry on the effectiveness of the aperture compensator and the effect of a variance from the designed value.

From Figure 4.13 it is found that varying the offset of the top and bottom aperture compensators independently yields the same results due to the symmetrical nature of the structure. A $3dB$ degradation in the reflection coefficient is found after a 1mm shift towards the aperture. Varying any of the other parameters has less of an effect on the impedance match of the antenna.

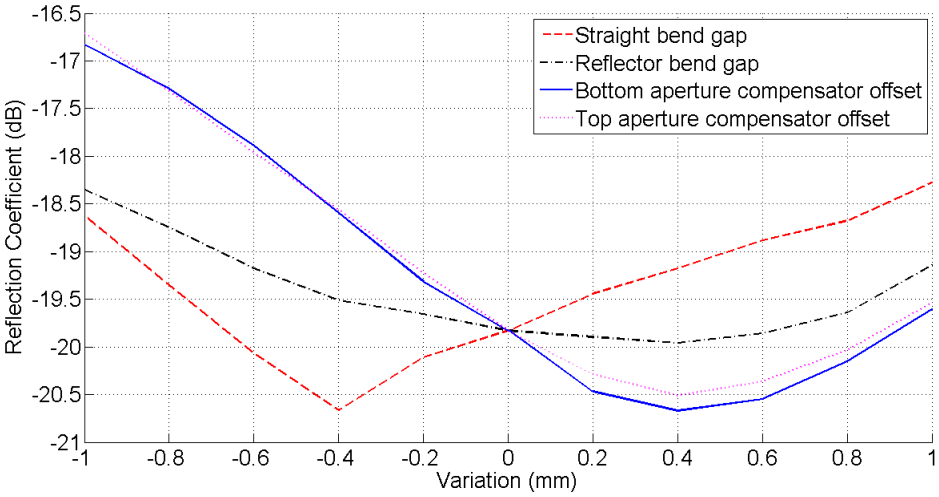

Figure 4.13: Variation in maximum reflection coefficient value for frequency band with change in indicated parameter values

The change in side-lobe levels are shown in Figure 4.14. Tolerance of the straight bend gap in Figure 4.14(a) show that a $3dB$ degradation in the side-lobe levels over the frequency band occur after a 0.6mm deviation from designed values. Figure 4.14(b) shows the same behaviour for the reflector bend where $3dB$ degradation occur after a 0.5mm deviation in parameter values. As expected, deviations in the offset values of the aperture compensator have little effect on the far-field pattern of the antenna and hence the side-lobe levels, as seen in Figure 4.14(c) and Figure 4.14(d).

4.4.2.2 Plate Warping Tolerance of Triple Layer Pillbox Structure

Plate warping could occur if adequate support is not introduced between the parallel plates. This could cause the plates to warp into the cavity containing the propagating waves. To simulate the effect of warping on the system, an extrusion is made on a scaled surface of each separate plate, Figure 4.15.

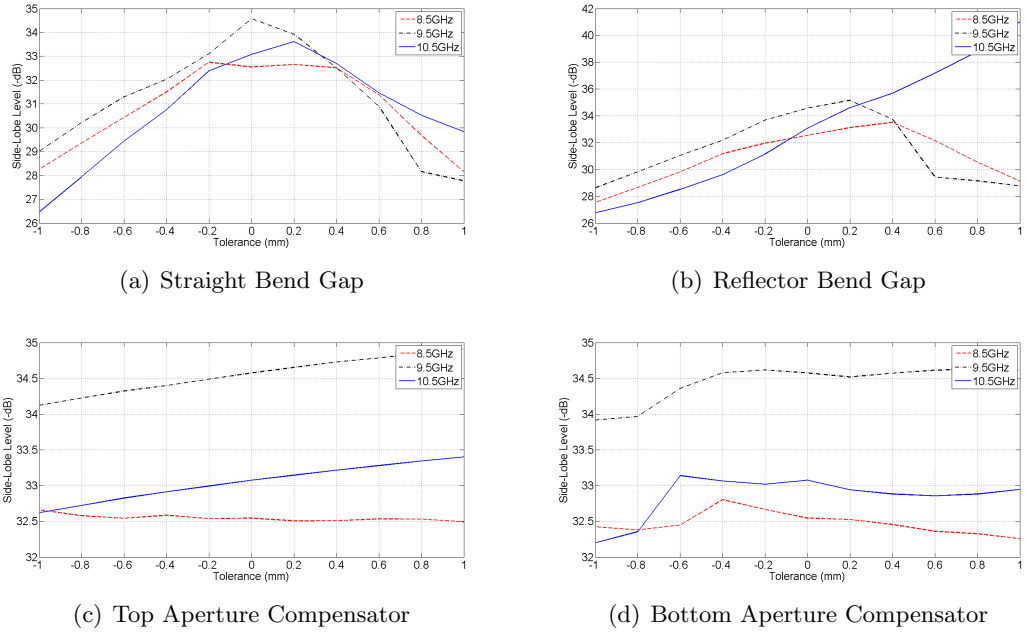

(a) Straight Bend Gap

(b) Reflector Bend Gap

(c) Top Aperture Compensator

(d) Bottom Aperture Compensator

Figure 4.14: Variation in side-lobe levels with change in indicated parameter values at different frequency values

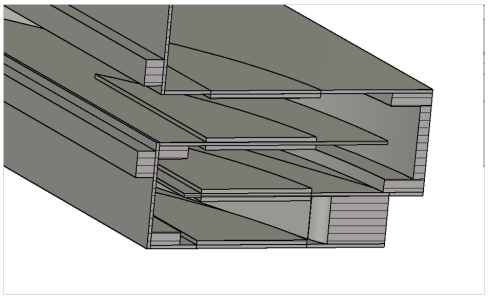

Figure 4.15: Model used to test tolerance of plate warping

The effect of warping on the antenna's side-lobe level is shown in Figure 4.16. Figure 4.16(a) shows the effect of warping of the outer most plate of the aperture layer on side-lobe levels and Figure 4.16(b) the inner plate of the aperture layer. Warping of either one of these plates start to cause a degradation of $3dB$ after about 1.2mm warping. Figure 4.16(c) and Figure 4.16(d) show the effect of warping into the middle layer. It is found that warping of about 1mm into the middle layer causes a $3dB$ degradation in side-lobe levels. Warping of plates into the feed layer causes a $3dB$ degradation at 1.2mm as shown in Figure 4.16(e) and Figure 4.16(f).

Figure 4.17 shows the effect of warping on the reflection coefficient. A $3dB$ degradation in

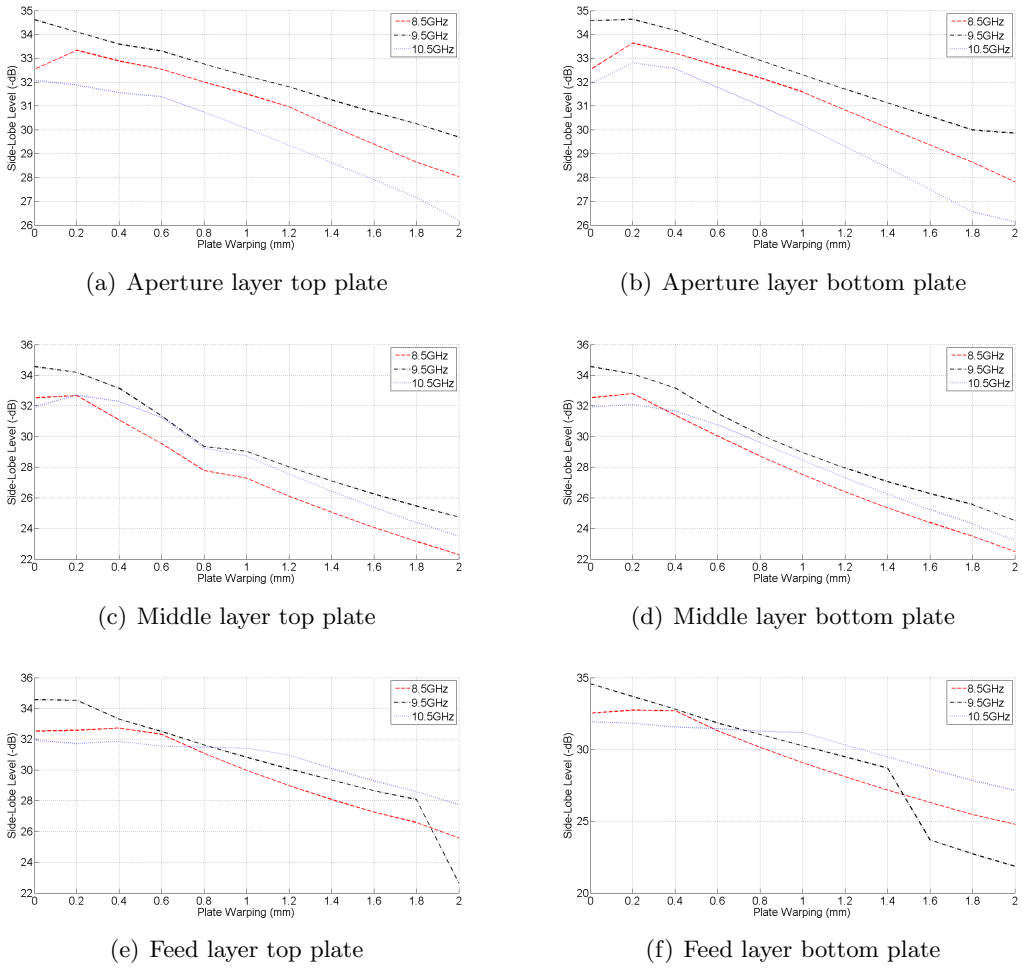

(a) Aperture layer top plate

(b) Aperture layer bottom plate

(c) Middle layer top plate

(d) Middle layer bottom plate

(e) Feed layer top plate

(f) Feed layer bottom plate

Figure 4.16: Variation in side-lobe levels with plate warping at different frequency values

the reflection coefficient is caused by a 1.6mm warping into the aperture layer. Warping into the other layers only starts to cause a $3dB$ degradation at 1.2mm.

4.4.3 Conclusion on Triple Layer Pillbox Simulated Results and Tolerance

Comparison of *CST* and *FEKO* results show some variation which is probably due to the rough meshing used in *FEKO*. *FEKO* results still show low side-lobes of at least $-27dB$. From this comparison it can be assumed with greater certainty that the results obtained in *CST* are reliable and should be practically attainable if the structure is manufactured to specification.

It was found that the position of the middle plates within the bends have a tolerance of roughly 0.5mm before side-lobe levels start to degrade significantly. Great care has to thus be taken in

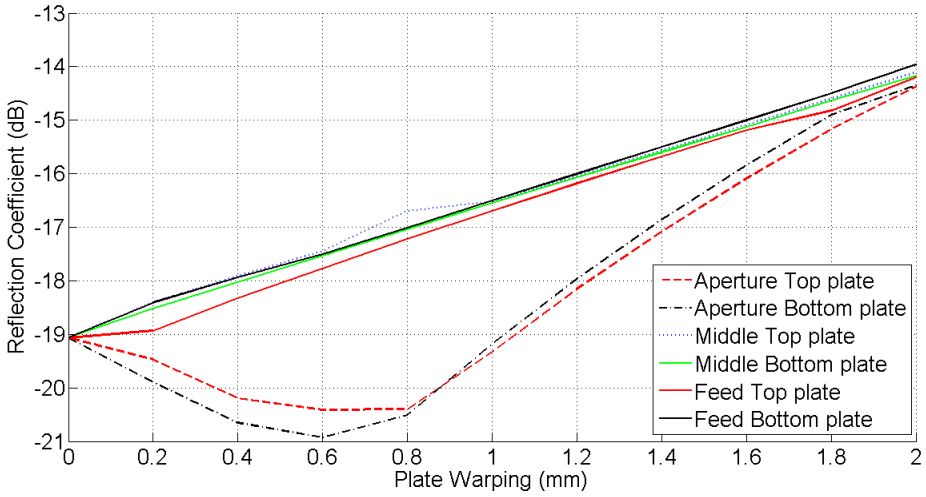

Figure 4.17: Variation in maximum reflection coefficient value in frequency band with plate warping

the manufacturing process while positioning the plates in order to achieve the required results. The aperture compensators have a tolerance of 1mm and only affect the reflection coefficient of the antenna, this tolerance is acceptable and should not prove too difficult to manufacture.

From tests done to determine the acceptable degree of warping of the parallel plates it was found that warping of any plate into any layer have a great effect on the performance of the antenna. Warping of about 1mm into a layer causes side-lobe levels to deteriorate significantly.

Overall the antenna is manufacturable with reasonable tolerance. The greatest concern in manufacturing is the effect that the warping of the plates have on performance, especially the plates in the aperture layer. These plates are the most prone to warping due to their limited structural support and will require extra support, especially with big structures.

4.5 Triple Layer Pillbox Construction

Simulation results and manufacturability need to be verified by constructing the triple layer pillbox antenna and then doing measurements to determine whether the antenna performs as expected.

The antenna is constructed using stacked, laser-cut, aluminium plates to verify that the antenna performs as expected when using this cheap construction method. Parallel plates are connected using screws, allowing for an easy assembly process.

4.5.1 Design of a Manufacturable Triple Layer Pillbox Structure

The triple layer pillbox antenna is designed to be manufactured from stacked, laser-cut, aluminium plates. It was decided to design for an aperture width of 20λ to keep construction costs down while making the construction process the same as will be used for larger sized antennas, as will be used in practice. A pin feed is used to replace the waveguide feed for measurement purposes.

Only standard aluminium sheet thicknesses can be used to build up the structure of the antenna, eliminating the need for machining. The antenna is redesigned to allow for standard sheet thicknesses of 1.2mm, 2mm, 3mm and 8mm. The height of the compensators located in the compensated transitions is increased to 3mm to allow the use of a single 3mm sheet per compensator. Plate spacing is increased to 11mm which can be obtained by placing an 8mm plate on top of the 3mm plate used for the compensated transition.

Aperture compensators are redesigned to have an offset of 2.2mm with a depth and height of 4mm. This is done to make manufacturing easier at the cost of a higher reflection coefficient at the aperture. Due to the low bandwidth of the pin feed, this should however not affect the antenna's reflection coefficient much. Construction of the aperture compensators is done by using two 3mm plates together with a 2mm plate instead of the 8mm plate in the middle layer. The 2mm plate is placed on top of the 3mm plate used for the compensated transition and extended 4mm to the front of the antenna to serve as a mounting position for another 2mm plate with a width of 4mm.

The bottom aperture compensator is made up of two 2mm plates, each with a width of 4mm which is stacked on top of each other and onto a 1.2mm vertical plate at the correct offset. This section is connected to the bottom plate of the antenna at the aperture through the use of an 8mm aluminium block. Figure 4.18 shows a diagram of the cross-section of the triple layer pillbox if assembled using laser-cut plates.

4.5.1.1 Coaxial Cable to Waveguide Transformation

The waveguide feed is replaced by a pin feed for measurement purposes. Figure 4.19 shows the model used to optimise the coaxial cable to waveguide transition. Parameters used for optimisation are the pin length and pin offset within the structure. A waveguide port is used to terminate the structure.

Figure 4.20 shows the reflection coefficient obtained after optimisation. A reflection coefficient

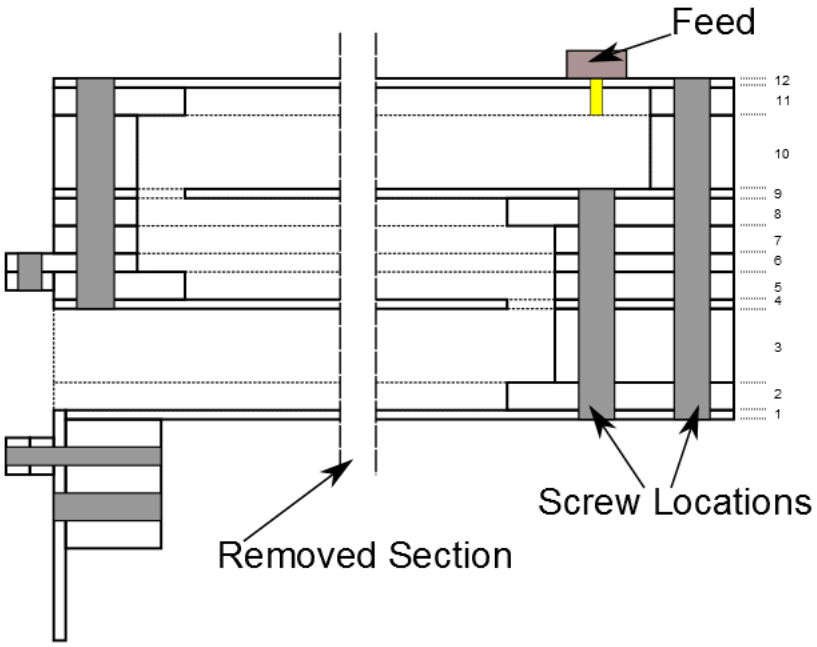

Figure 4.18: Diagram of Triple Layer Pillbox assembled from parallel plates

of $-17dB$ is acquired for the transition model within the required frequency band.

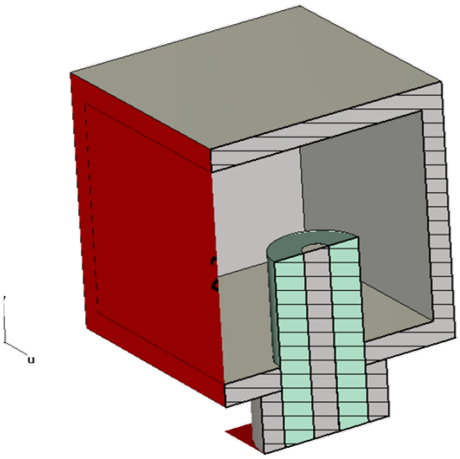

Figure 4.19: Model of pin feed

The designed triple layer pillbox antenna is simulated with a pin feed as well as with a waveguide feed. Figure 4.21 compares the reflection coefficient obtained from using a pin feed to that obtained from using a waveguide feed. It can be seen that the reflection coefficient of the

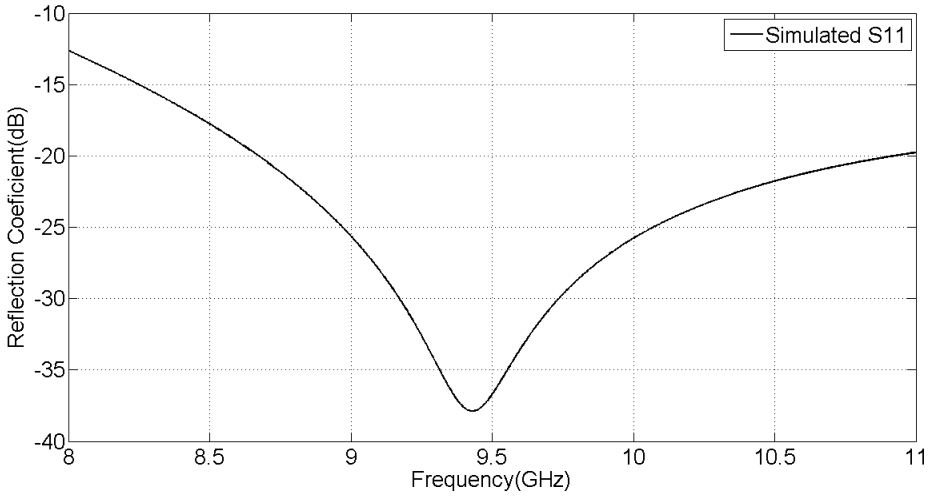

Figure 4.20: Reflection coefficient of pin feed

model with a pin feed is poorer at the lower frequencies, but still adequate.

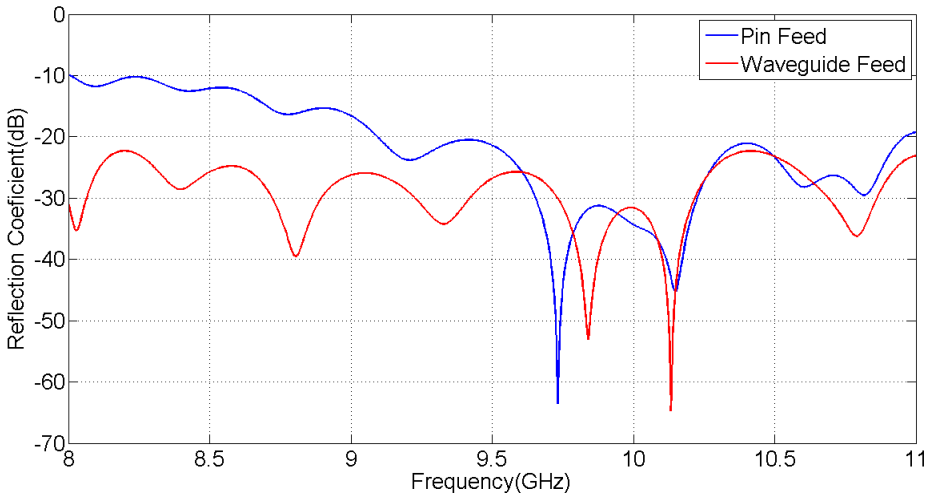

Figure 4.21: Reflection coefficient of manufacturable Triple Layer Pillbox with pin feed compared to waveguide feed

4.5.2 Assembling Triple Layer Pillbox from Stacked Plates

Plates are connected to each other through the use of M3(3mm) screws, using counter-sink screws where needed. Holes are positioned along the edges of all the cavities and are positioned 20mm, less than a wavelength, apart. This ensures thorough connectivity between the parallel

plates. Figure 4.22 shows the final model of the pillbox antenna with screw hole positions.

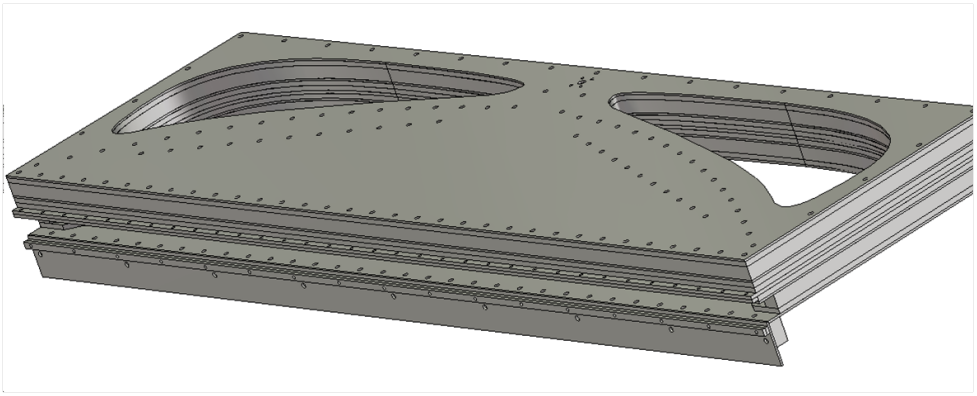

Figure 4.22: Model of Triple Layer Pillbox assembled from parallel plates

A female SMA connector with extruded pin and Teflon is used for the pin feed. The pin and Teflon are machined to a length of 6.7mm to allow for an extrusion of 5.5mm above the 1.2mm plate on which it is mounted. The pin and Teflon are chosen to be the same length to make machining easier.

Referring to Figure 4.18, the antenna is assembled from the top down. The SMA connector is first attached to plate 12 using counter-sunk M2 screws. Counter-sink holes are drilled into plates 1, 4 and 9. A piece of expanded polystyrene with a thickness of 11mm is inserted into the cavity created by plates 9 to 12 which is then screwed together using counter-sunk M3 screws. The constructed top layer is shown in Figure 4.23. Plate number 9 is shown here at the top with the counter-sunk M3 screws and compensated transition gap visible.

In the second phase of the construction process, plates 4 to 8 are placed on to the assembled top layer structure with polystyrene filling the cavity. These plates are then fastened using counter-sunk M3 screws as seen in Figure 4.24. The counter-sunk M3 screws and second compensated transition gap in plate 4 can be seen here.

Before attaching the last plates, the bottom aperture compensator structure needs to be assembled. This is done by attaching the two 2x4mm plates onto the vertical 1.2mm plate and 8mm block through the use of M2(2mm) counter-sink screws. This structure is then attached to plate 1 through counter-sink M3 screws as seen in Figure 4.25.

The remaining plates are then positioned with polystyrene in the cavity and screwed together

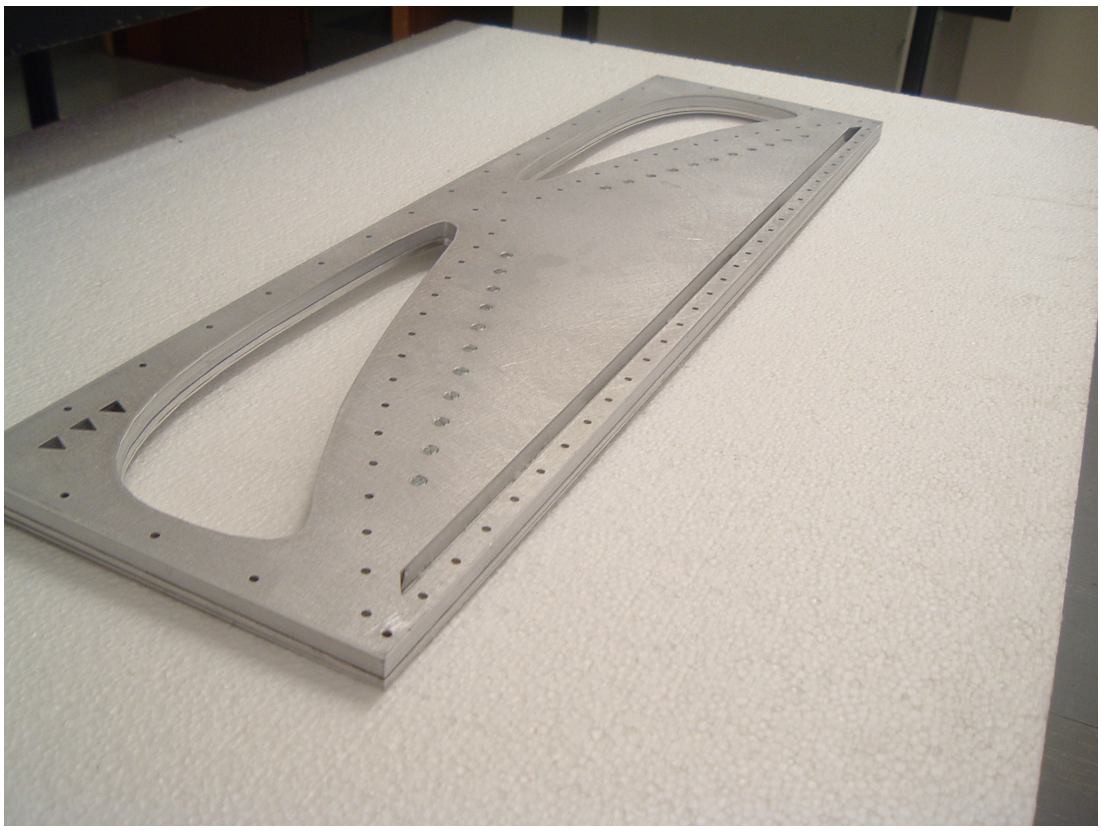

Figure 4.23: Constructed top layer of Triple Layer Pillbox, assembled from parallel plates

using M3 cheese-head screws. Finally the top aperture compensator is completed by placing the 2x4mm plate at the bottom of the extruding part of plate 6 and fastening it with M2 screws. The fully constructed antenna is seen in Figure 4.26 with plate 1 at the top.

4.6 Triple Layer Pillbox Measurements

Due to the limited size of the available anechoic chamber, near-field measurements are done which are in turn transformed to the far-field to obtain the antenna's radiation pattern. A discussion is given on the theory of near to far-field transformation, showing the process of obtaining far-field radiation patterns from measured near-fields.

In the following section the obtained far-field patterns are then compensated for the probe pattern. Here the theory of probe compensation is discussed and formulas derived for the measurement configuration used.

The effect of different setup configurations within the anechoic chamber is then investigated

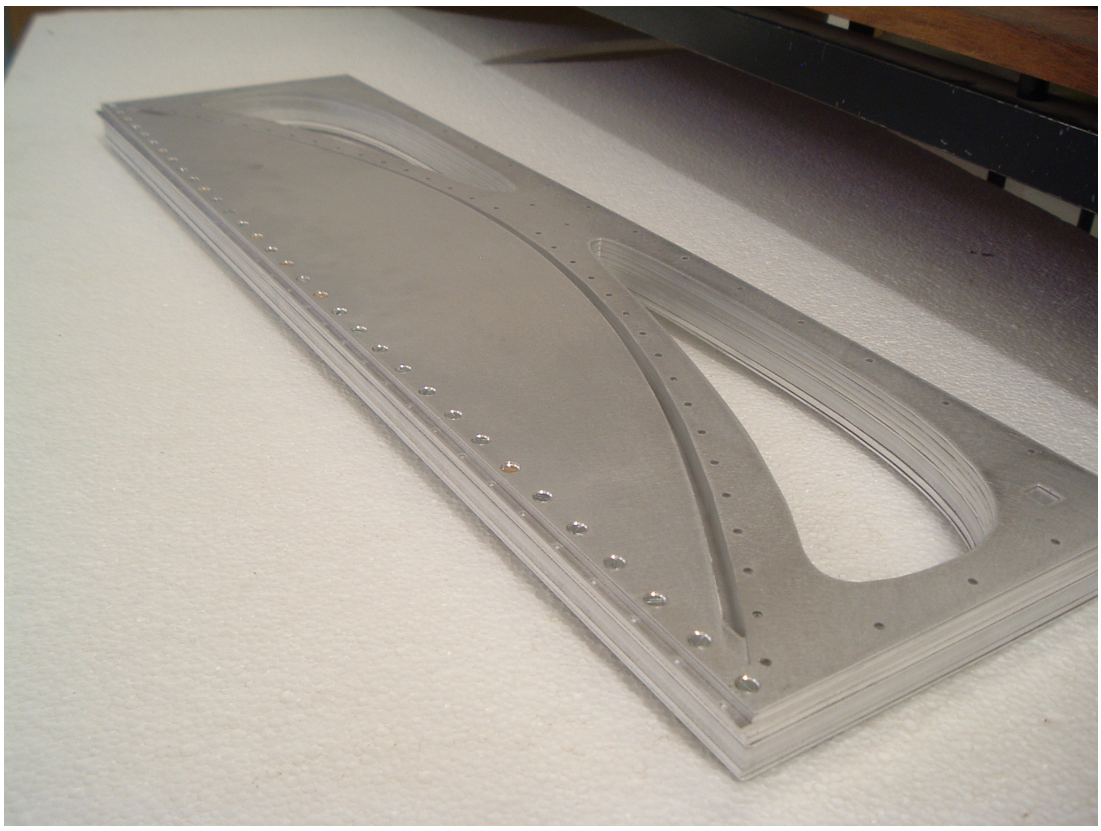

Figure 4.24: Constructed top two layers of Triple Layer Pillbox, assembled from parallel plates

to determine the optimal configuration to obtain the most accurate measurements.

Measurements are then done on the constructed triple layer pillbox antenna using the techniques discussed. Antenna performance is evaluated based on the acquired results.

4.6.1 Theory on Near to Far-field Transformation

The minimum distance, R, between the AUT (Antenna Under Test) and probe at which accurate far-field measurements can be taken is, [10],

$$R \geq \frac{2D^2}{\lambda} \tag{4.1}$$

where D is the AUT's aperture width. The designed antenna with a 0.6m aperture width would thus require an anechoic chamber which is at least 24m long, which is not readily available. It is thus necessary to take near-field measurements and convert them to the far-field to obtain the antenna's radiation pattern.

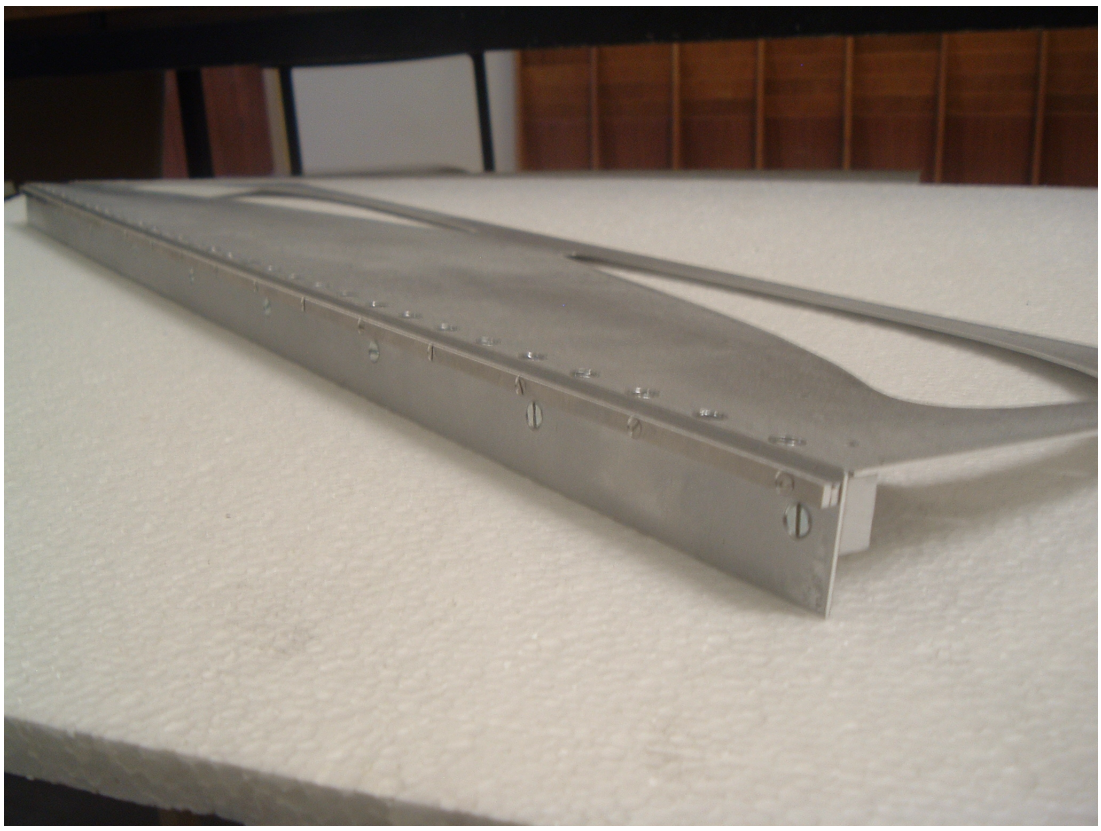

Figure 4.25: Constructed bottom aperture structure of Triple Layer Pillbox, assembled from parallel plates

E-field measurements are taken at a distance of 2λ up to 3λ between the probe and AUT. These measurements are then converted to the spectral domain through the use of a 2-D Fourier transform, [7],

$$F(k_x, k_y, z = 0) = \Im(E(x, y, z = 0)) \tag{4.2}$$

or

$$F(k_x, k_y, z = 0) = \int_{-\infty}^{\infty}\int_{-\infty}^{\infty} E(x, y, z = 0)e^{j(k_x x + k_y y)}dxdy, \tag{4.3}$$

which is solved with FFT algorithms. The spectral coordinates, k_x, k_y and k_z, are derived from the cartesian coordinates from

$$k_x = \frac{2\pi m}{M\Delta x}, k_y = \frac{2\pi n}{N\Delta y}, \tag{4.4}$$

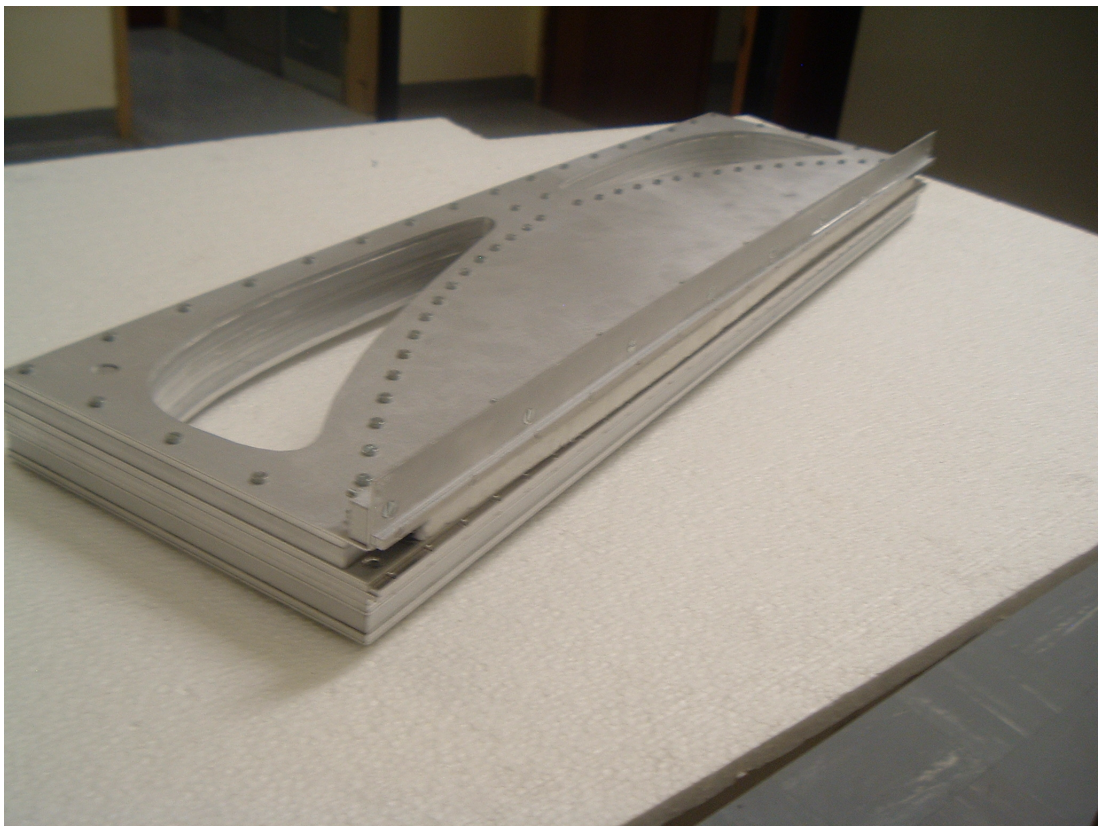

Figure 4.26: Constructed Triple Layer Pillbox, assembled from parallel plates

$$k_z = \begin{cases} +\sqrt{k_0^2 - (k_x^2 + k_y^2)}, & \text{when } k_0^2 \geq k_x^2 + k_y^2 \\ -j\sqrt{(k_x^2 + k_y^2) - k_0^2}, & \text{when } k_0^2 < k_x^2 + k_y^2 \end{cases} \tag{4.5}$$

where

$$M = \frac{a}{\Delta x} + 1, \quad N = \frac{b}{\Delta y} + 1, \tag{4.6}$$

here a and b are the respective width and height of the measurement plane. The vectors, m and n are described through

$$-\frac{M}{2} \leq m \leq \frac{M}{2} - 1, \quad -\frac{N}{2} \leq n \leq \frac{N}{2} - 1. \tag{4.7}$$

The antenna's far-field pattern is obtained from the spectral pattern through, [10],

$$E_{far-field}(k_x, k_y) = j\frac{e^{-jk_0 r}}{\lambda r}\frac{k_z}{k_0}F(k_x, k_y). \tag{4.8}$$

The spectral coordinates are related to the spherical coordinates through

$$k_x = k_0 sin(\theta) cos(\phi), \tag{4.9}$$

$$k_y = k_0 sin(\theta) sin(\phi), \tag{4.10}$$

$$k_z = k_0 cos(\theta). \tag{4.11}$$

4.6.2 Theory on Probe Compensation

Due to the non-uniform pattern of the probe, compensation needs to be done on the measured far-field pattern of the AUT. In order to do this, the probe's pattern needs to be known. To determine the probe's pattern a theoretical approach is needed as found in [11] for rectangular waveguides.

The theoretical 2-D spectral far-field pattern of an open-ended WR-90 waveguide is shown in Figure 4.27 with cuts along the $\Phi = 0°$ and $\Phi = 90°$ of the spherical pattern shown in Figure 4.28.

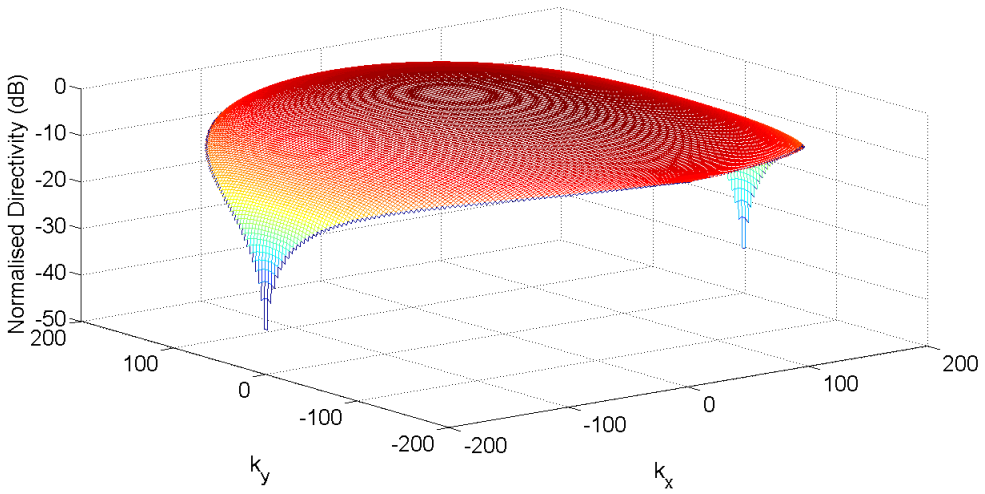

Figure 4.27: 3-D Open-ended WR-90 waveguide probe far-field pattern

To decouple the probe's pattern from the antenna's pattern, the antenna-to-antenna coupling formula from [10] is transformed to the coordinate system used in measurements in Appendix.B. The pillbox antenna is y-polarised and thus only the y-polarised, S_y, pattern is used,

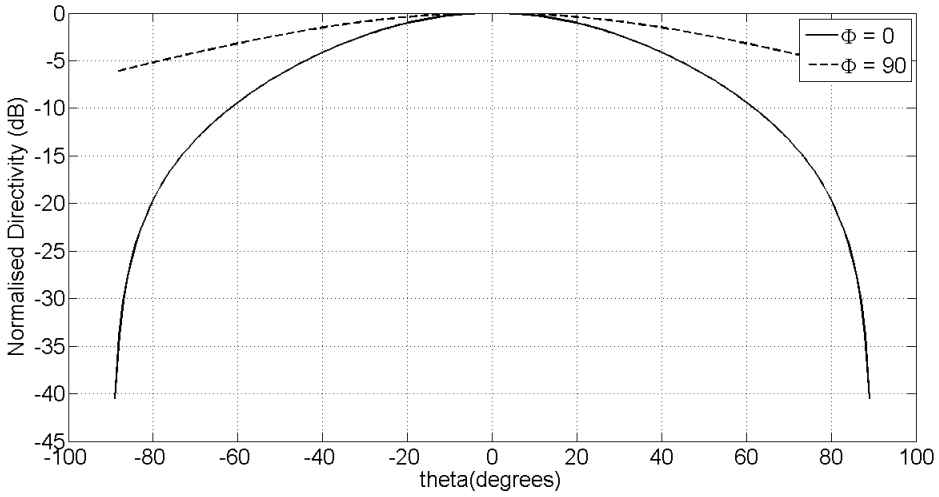

Figure 4.28: Open-ended WR-90 waveguide probe far-field pattern at $\Phi = 0°$ and $\Phi = 90°$

$$\begin{aligned} S_y(\alpha,\beta) &= \frac{j}{\lambda}\left\{(\beta^2-1)P_x^C(\alpha,-\beta)A_x(\alpha,\beta)\right. \\ &\quad +(\beta\alpha)P_y^C(\alpha,-\beta)A_x(\alpha,\beta) \\ &\quad -(\alpha\beta)P_x^C(\alpha,-\beta)A_y(\alpha,\beta) \\ &\quad \left.+(1-\alpha^2)P_y^B(\alpha,-\beta)A_y(\alpha,\beta)\right\}\frac{e^{-jk_z z0}}{\gamma}. \end{aligned} \tag{4.12}$$

The direction cosines, α, β and γ are calculated from k_x/k_0, k_y/k_0 and k_z/k_0 respectively. $S(\alpha,\beta)$ is the measured far-field pattern, $P(\alpha,-\beta)$ the probe's theoretical far-field pattern and $A(\alpha,\beta)$ the antenna's actual far-field pattern.

Both the probe and AUT is y-polarised and it is thus assumed that the x-polarised components are negligibly small. This assumption allows equation (4.12) to be significantly simplified. The compensated antenna far-field pattern is now calculated through

$$A_y(\alpha,\beta) = \frac{\lambda}{j}\frac{1}{(1-\alpha^2)}\frac{S_y(\alpha,-\beta)\gamma e^{jk_z z_0}}{P_y(\alpha,-\beta)}. \tag{4.13}$$

4.6.3 Optimal Chamber Setup Configuration

In near-field measurements the AUT needs to be positioned on a pedestal at a distance of between 2λ and 3λ from the measurement probe. This close proximity between the probe and

AUT causes increased scattering from the antennas and also the pedestal on which the AUT is mounted. To reduce the effects of scattering an optimum setup configuration is thus required within the anechoic chamber.

A pedestal needs to be used that causes the least amount of scattering. To determine which configuration works best an open-ended waveguide with WR-90 dimensions is measured on different pedestals and its measured radiation pattern compared to the theoretical pattern. The pedestals used are a polystyrene block, a metal stand and one of the walkway blocks used in the anechoic chamber.

Figure 4.29 shows the azimuth and elevation far-field patterns of the open-ended waveguide measured while mounted on a metal stand. The metal stand elevates the antenna 1.6m from the ground and consists of a metal pipe with a stand at one end and a mounting position for the antenna on the other. Asymmetry can be seen in both the azimuth and elevation patterns, significant ripples are also noted in both the patterns.

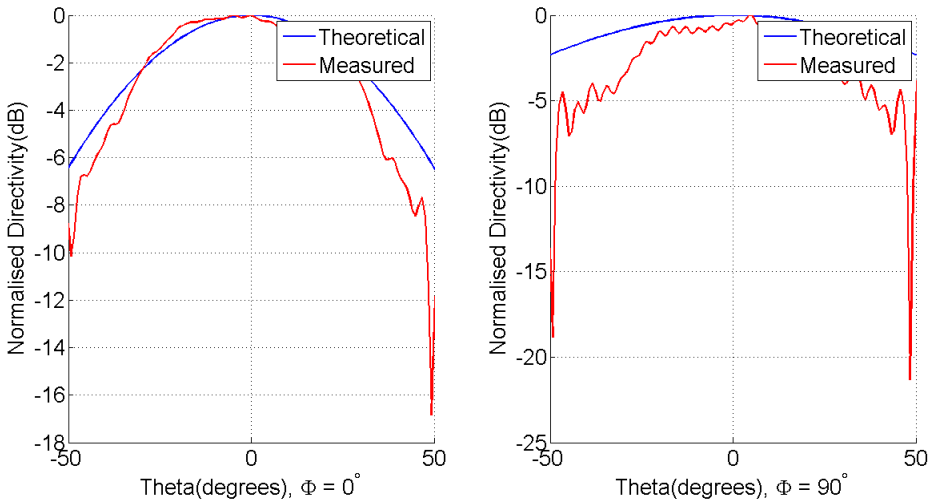

Figure 4.29: Normalised directivity of open-ended waveguide mounted on metal stand

A polystyrene block with a height of 1.8m is used to acquire the radiation pattern found in Figure 4.30. A much smoother and symmetrical pattern is found for the polystyrene block than is found for the metal stand.

One of the walkway blocks used in the anechoic chamber is tipped on its side, with its walking surface faced towards the measurement probe. To add some height, a block of polystyrene with

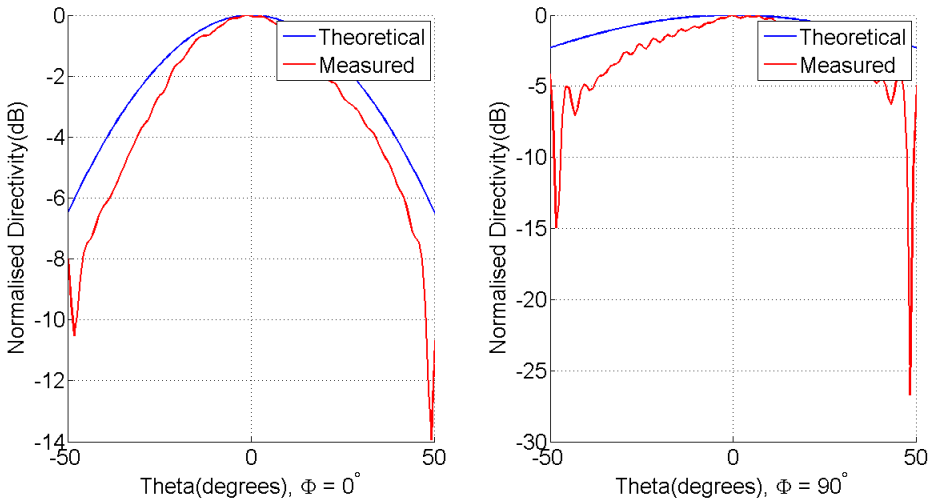

Figure 4.30: Normalised directivity of open-ended waveguide mounted on Polystyrene block

a height of 30cm is put on top of the walkway block as shown in Figure 4.31. Figure 4.32 shows the far-field pattern when using the walkway block as a stand. Both the elevation and azimuth patterns appear to be similar to the ones obtained from using the polystyrene block.

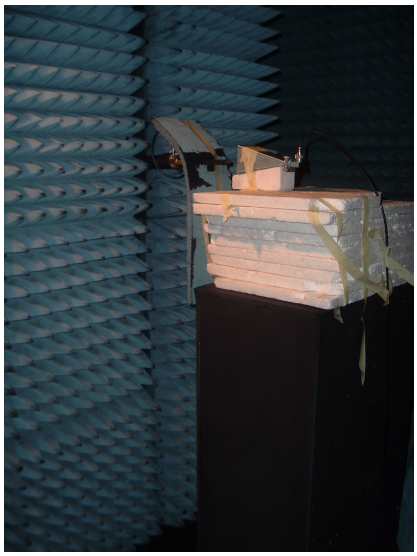

Figure 4.31: Horn mounted on walkway block

From the results obtained from the different configurations it was decided to use the walkway block as a pedestal. This configuration is easier to setup than the large block of polystyrene and

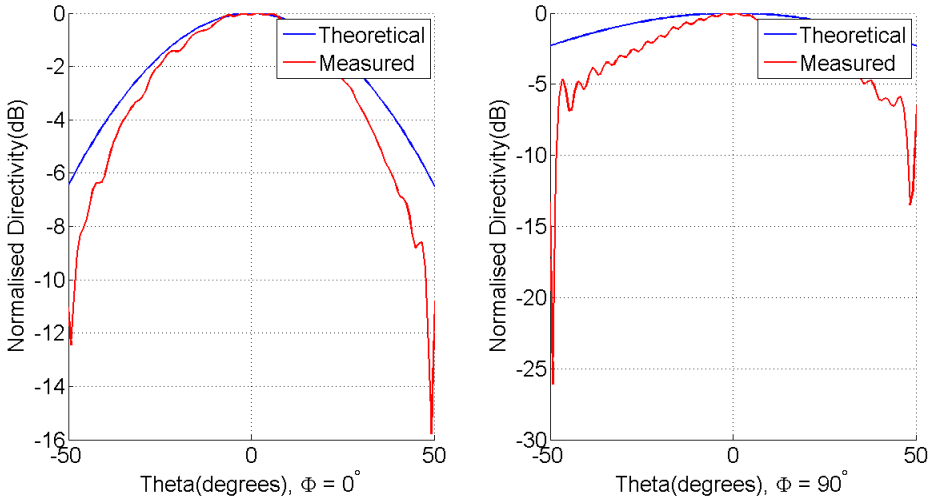

Figure 4.32: Normalised directivity of open-ended waveguide mounted on walkway block

yields results closest to the expected results.

4.6.4 Measured Results for Triple Layer Pillbox Antenna

Measurements were taken at a distance of 60mm, 70mm, 80mm and 90mm between the AUT and probe. These results were then averaged to decrease the effect of scattering within the anechoic chamber and improve the accuracy of the results.

In Figure 4.33 a 2-D near-field measurement is shown at centre frequency at an offset of 70mm. Measurements were taken at 10mm increments for 1200mm along the x-axis and 500mm along the y-axis. The increment size was chosen to be less than $\lambda/2$ to satisfy the Nyquist sampling criterion, [7]. The minimum length of each axis can be calculated from, [10],

$$\theta_{max} = arctan\left(\frac{L-D}{2z}\right) \tag{4.14}$$

where θ_{max} is the maximum angle at which the far-field pattern will be accurate, z is the offset between the AUT and probe, D the AUT aperture width and L the length of the measurement plane.

Figure 4.34 shows the normalised magnitude of the near-field measurement along the x-axis, normal to the aperture, compared to the simulated result. The measured result compares well to the simulated result at the centre, but starts deviating at the edges.

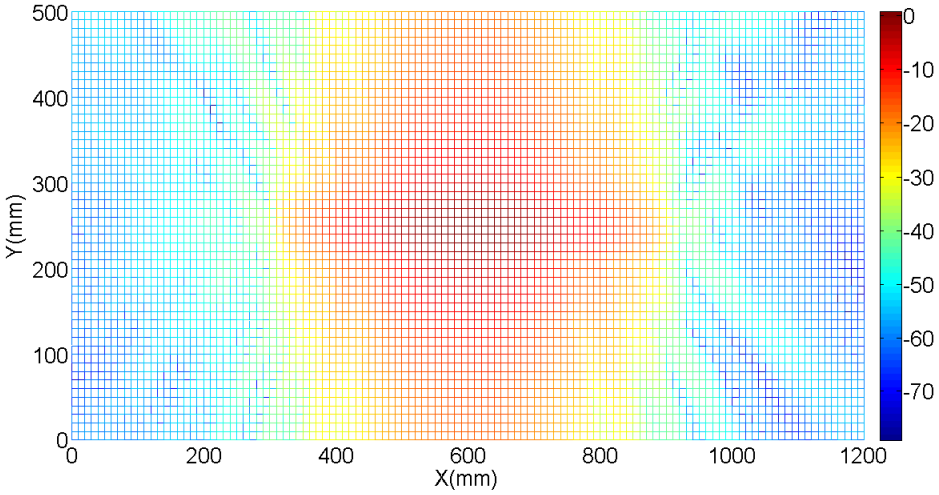

Figure 4.33: Normalised magnitude of 2-D near-field measurement of Triple Layer Pillbox antenna in dB

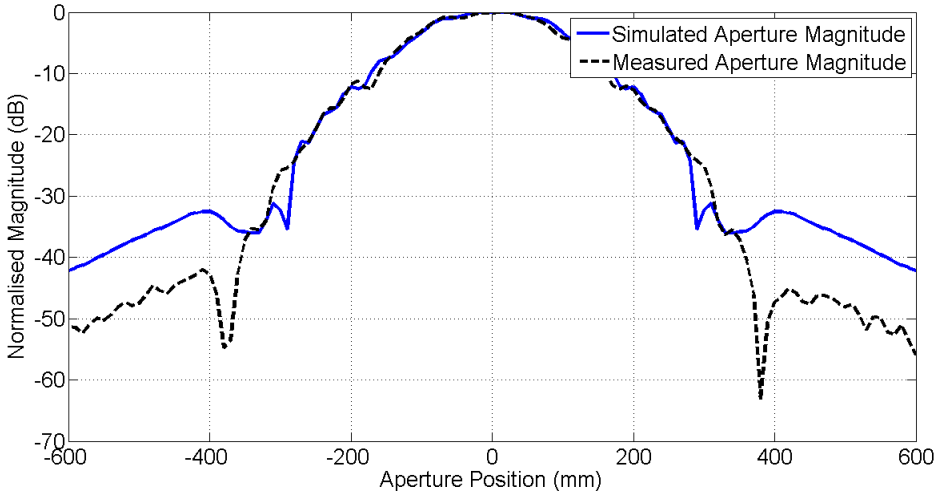

Figure 4.34: Normalised magnitude of near-field measurement along the x-axis of the Triple Layer Pillbox antenna in dB compared to simulated results

The phase shown in Figure 4.35 is taken along the same line as the magnitude. The measured phase also compares well to the simulated phase.

A near to far-field transform is done on each measurement. The resulting azimuth far-field patterns at centre frequency are shown in Figure 4.36. It can be seen that the far-field patterns correlate well to each other in the main lobe, but deviate by up $1dB$ in the side-lobes.

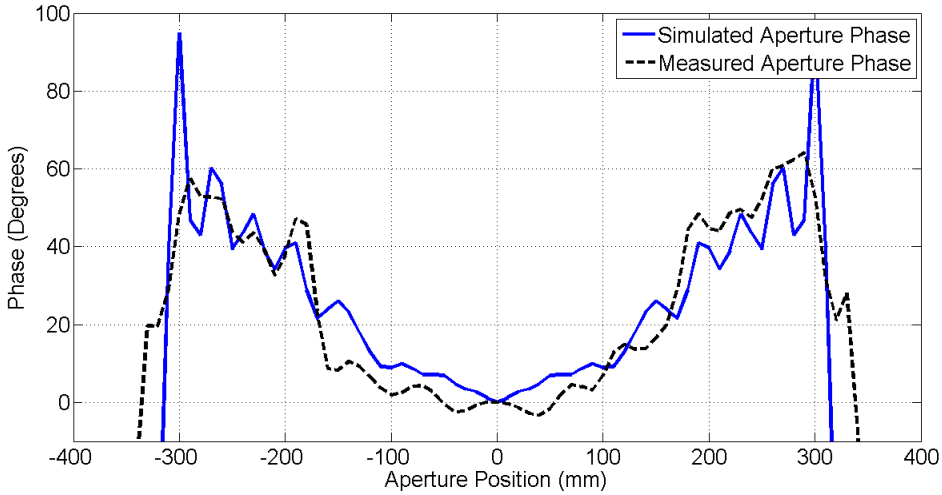

Figure 4.35: Phase of near-field measurement along the x-axis of the Triple Layer Pillbox antenna in dB compared to simulated results

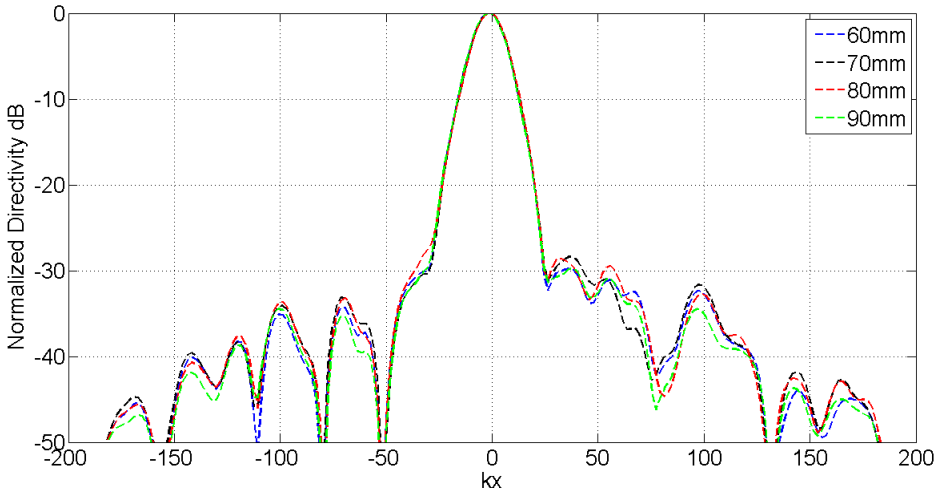

Figure 4.36: Azimuth far-field results obtained from near-field measurements taken at different distances between the probe and Triple Layer Pillbox

The four patterns are averaged and probe compensation done, Figure 4.37. Probe compensation raises the outer side-lobes, but does not increase the relative side-lobe level significantly.

The measured azimuth far-field pattern over the 20% bandwidth is found in Figure 4.38. The highest side-lobes are found at the lower frequencies at $-27dB$. This is larger than the $-30dB$ side-lobes found through simulation, Figure 4.39, and can be attributed to manufacturing

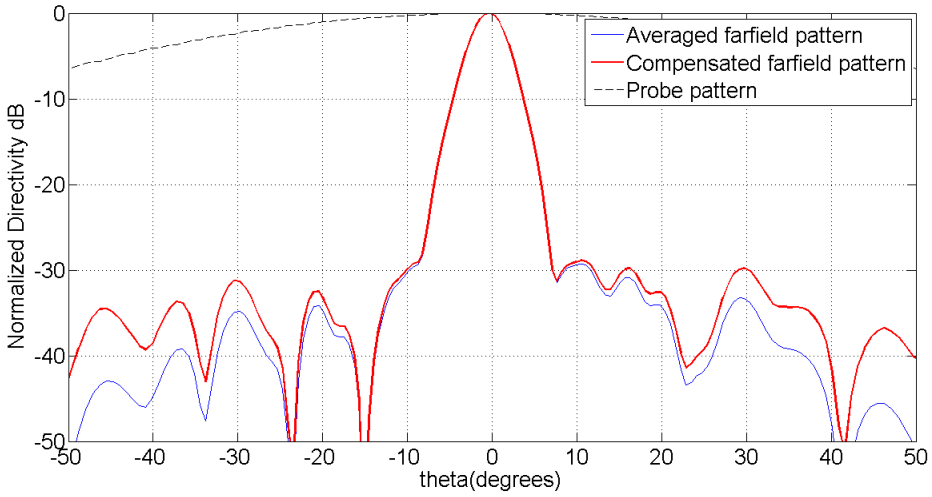

Figure 4.37: Azimuth far-field pattern of Triple Layer Pillbox at centre frequency after probe compensation is done

tolerances and measurement errors. Figure 4.40 shows the far-field elevation pattern at $8.5GHz$, $9.5GHz$ and $10.5GHz$ which does not look as expected due to reflections off the ground and stand. The measured and simulated results correlate well enough to prove the concept.

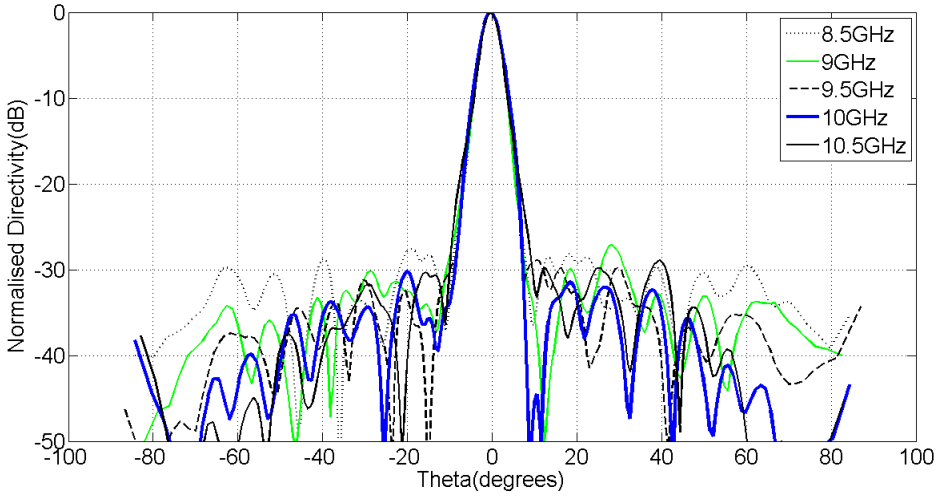

Figure 4.38: Measured azimuth far-field pattern of Triple Layer Pillbox over 20% bandwidth

The reflection coefficient of the triple layer pillbox antenna was measured using a VNA (Vector

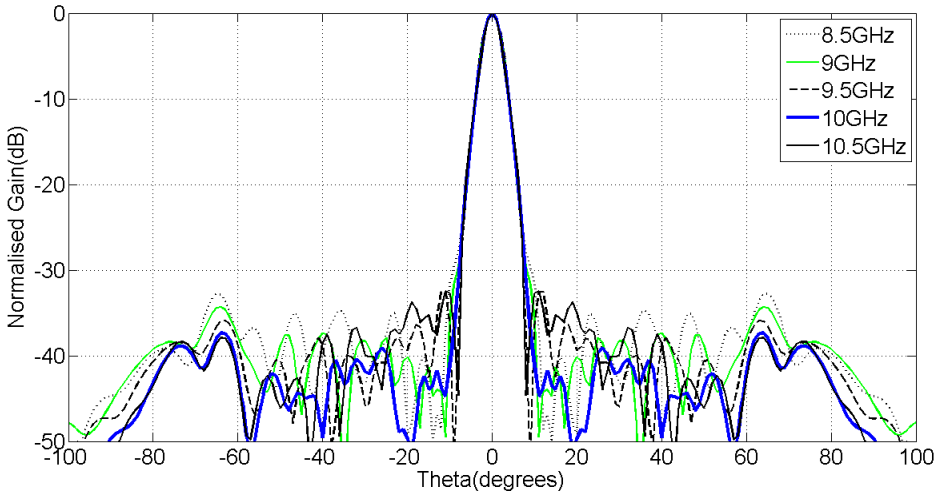

Figure 4.39: Simulated azimuth far-field pattern of constructed Triple Layer Pillbox over 20% bandwidth

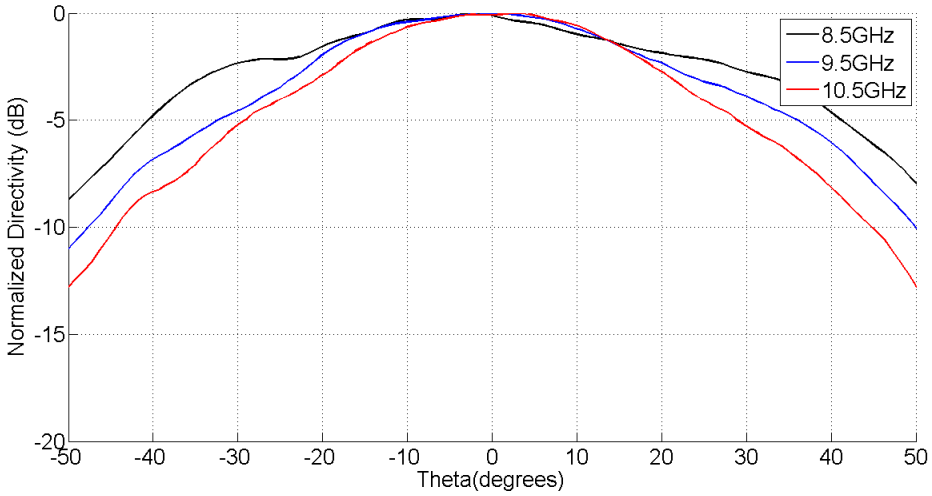

Figure 4.40: Measured elevation far-field pattern of Triple Layer Pillbox over 20% bandwidth

Network Analyzer) in an open room. A reflection coefficient of less than $-10dB$ is measured for the 20% frequency band as shown in Figure 4.41. This compares well to the simulated result also shown in Figure 4.41.

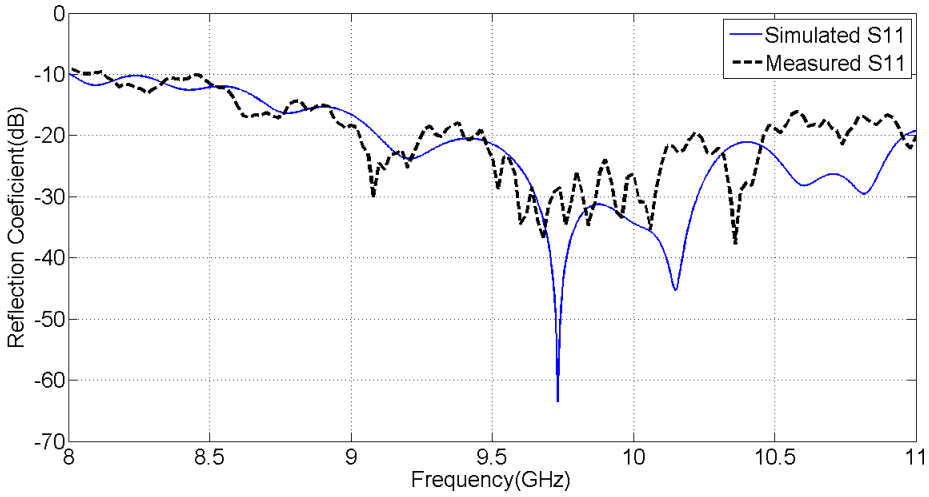

Figure 4.41: Measured reflection coefficient of Triple Layer Pillbox compared to its simulated result

4.6.5 Conclusion on Triple Layer Pillbox Measurements

The triple layer pillbox antenna was constructed using stacked laser-cut aluminium plates which were bolted together. The resulting mechanical design was easy to assemble and relatively cheap.

Algorithms for near to far-field transformation as well as probe compensation were derived and implemented successfully. Probe patterns were shown to be theoretically calculated using literature.

An optimal measurement setup was found to comprise of one of the anechoic chamber walk way blocks which was positioned on its side with polystyrene on the top for extra height.

Measured results correlated well with the simulated results with side-lobes of less than $-27dB$ acquired within the frequency band. The use of a pin feed simplified the measurement process, but resulted in a poorer reflection coefficient. A reflection coefficient of less than $-10dB$ was still obtained from measurements which agree with the simulated value.

CHAPTER 5
Dual Reflector Shaping

5.1 Introduction to Dual Reflector Shaping

This section describes the use of dual reflector shaping in a triple layer pillbox antenna. A discussion is given on the theory of dual reflector shaping, focussing on the process of obtaining an algorithm to synthesise shaped curves which would yield a required power distribution for an arbitrary source distribution. These synthesised curves are further validated theoretically through the use of ray tracing techniques. Algorithms are derived to transform simulated fields in the feed model to rays. This is done in order to obtain an accurate model for the input feed distribution which allows the synthesised curves to be implemented into a physical model. Curves are synthesised for two antenna designs, one with an aperture distribution which would yield low side-lobes and another which would yield higher gain. Both antennas are first simulated, then constructed and measured using the techniques discussed in Chapter 4.5. A brief discussion is given on gain measurement theory which is used to determine the gain realised for the high gain and low side-lobe antennas respectively.

Due to the good transmittance obtained in the compensated transitions, the triple layer pillbox can be modelled as a two-dimensional structure which comprises two reflectors and a source. These reflectors can be shaped to yield a desired aperture distribution through the use of GO (Geometric Optics), [12], for a given input source distribution. This allows the antenna to be designed to achieve a required radiation pattern, giving the designer more control. Expressions are derived with which to synthesise dual shaped curves using Snell's Law, the Conservation of Energy and the Theorem of Malus. It is shown that these expressions can be solved simultaneously for arbitrary input and output power distributions. The synthesised curves are validated through ray tracing techniques which are shown to effectively be the described curve shaping process in reverse.

An accurate model of the feed system is attained to be used as input to the curve synthesis algorithm. Fields are obtained within the feed structure through simulation along a line. These fields are then transformed to rays through either the use of the Poynting vector or by taking the gradient of the phase difference between consecutive rays. Values for the point of origin, phase and power of each ray is then calculated to be used in the dual curve shaping algorithms.

Two dual shaped triple layer pillbox antennas are designed for different radiation patterns to illustrate the effectiveness in using dual reflector shaping to achieve specified aperture distributions. One antenna is designed to achieve low side-lobes through the use of a Gaussian power distribution, whereas the other antenna is designed for higher gain through the use of a cosine power distribution. Both antennas are shown through simulation to achieve their required results. The low side-lobe antenna is shown to achieve centre frequency side-lobes of $-40dB$ while obtaining a reflection coefficient of less than $-25dB$ for the 20% bandwidth. Simulation further show that $2dB$ more gain is acquired for the higher gain antenna while obtaining a reflection coefficient of less than $-20dB$ for the 20% bandwidth.

Both antennas are constructed and measured to verify that the simulated results are obtainable. It is found that the low side-lobe antenna only yielded $-34dB$ side-lobes instead of the simulated $-40dB$ side-lobes which are shown to be possibly attributed to manufacturing tolerances. Measured results for the high gain antenna are shown to correlate well to the simulated data, confirming that the design process used to design dual shaped triple layer pillbox antennas is practical.

5.2 Theory of Dual Reflector Shaping

Dual reflector shaping algorithms are derived from GO principles in Galindo, [12], through the use of Snell's Law, the law of Conservation of energy flow and the theorem of Malus. The law of Conservation of energy flow dictates the power distribution, whereas the theorem of Malus is used to determine the phase distribution. Snell's Law together with the law of Conservation of energy flow and the theorem of Malus is used to determine the gradient of the reflectors required to acquire the necessary aperture distribution.

5.2.1 Optical Principals Relevant to Dual Reflector Shaping

5.2.1.1 Snell's Law

Snell's Law [13] states that,

$$n_1 sin\theta_1 = n_2 sin\theta_2 \tag{5.1}$$

where n_1 is the refraction index of the medium in which the incident ray travels and θ_1 the angle at which the incident ray intercepts the boundary between mediums. The same applies to n_2 and θ_2 for the reflected ray.

When applied to an ideal reflection where an incident ray intercepts a metal boundary, the reflected ray propagates in the same medium as the incident ray and thus $n_1 = n_2$. This causes (5.1) to become

$$sin\theta_1 = sin\theta_2 \tag{5.2}$$

which shows that the angle of incidence, θ_1, is equal to the reflected angle, θ_2.

5.2.1.2 Conservation of Energy

The law of conservation of energy [13] states that the power in any section of a ray tube must be the same as in any other section of that ray tube,

$$S_1 * A_1 = S_2 * A_2. \tag{5.3}$$

Here S_1 and S_2 represent the power density at section 1 and 2 respectively. The area of each section is represented by A_1 and A_2.

5.2.1.3 Theorem of Malus

The theorem of Malus states that a normal congruence after any number of reflections and refractions is again a normal congruence, [13]. This essentially means that if a system of rays is orthogonal to a surface of constant phase, the rays will again be orthogonal to a surface after any number of reflections.

5.2.2 Derivation of Dual Shaping Procedure

5.2.2.1 Algorithms Describing Power Distribution

Using the principle of the conservation of energy, 5.2.1.2, the correlation between the input angle, θ_1, of a ray to its position in the aperture, x_2', can be obtained.

The power density across an area of a ray tube at the input needs to be equal to the power density across an area of the same ray tube at the output. Thus,

$$I(\theta_1)A_1 = P(x_2')A_2, \tag{5.4}$$

where $I(\theta_1)$ is the power density at the input for a ray with a given angle, θ_1, at a point with a cross section with an area A_1. $P(x_2')$ is the power density at the aperture of the antenna at

position x_2' for the same ray tube with a cross section area of A_2.

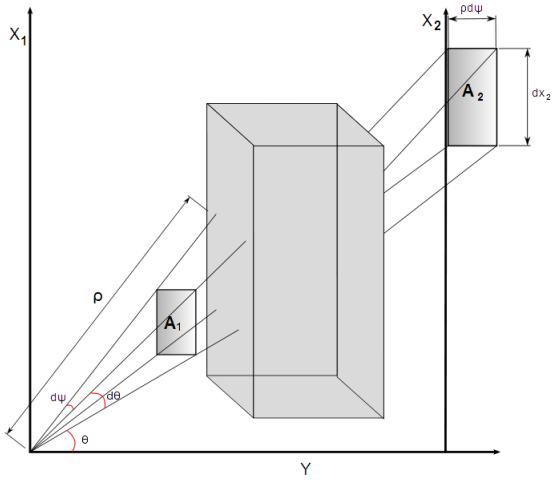

Figure 5.1: Diagram illustrating the flow of power in a ray tube through the system

Figure 5.1 illustrates the change in the cross-section dimensions of a ray tube through a system. The area of the cross-section of the ray tube increases from A_1 at its input to A_2 at the aperture. From Figure 5.1 the area A_1 can be written as the product of the elevation and azimuth angular widths, $d\theta$ and $d\Psi$ respectively, of the ray tube as $d\theta d\Psi$.

It can be assumed that the rays become essentially parallel in the azimuth plane after the first reflection, [14], leaving the azimuth width the same through the system as $\rho d\Psi$, where ρ is the distance from the source to the first reflector. A_2 is expressed in Cartesian coordinates as the product of the width, $\rho d\Psi$, and length, dx_2', of the outgoing ray bundle as $\rho d\Psi dx_2'$. Equation (5.4) now becomes,

$$I(\theta_1)d\theta_1 d\Psi \equiv P(x_2')\rho d\Psi dx_2'. \tag{5.5}$$

It is noted that the expression is in two different coordinate systems with $d\theta_1 d\Psi$ in cylindrical coordinates and $\rho d\Psi dx_2'$ in Cartesian coordinates. Both sides are transformed to the same Cartesian coordinate system by multiplying both sides with their corresponding x-axis positions. The equation is simplified to

$$I(\theta_1)x_1 d\theta_1 d\Psi = P(x_2')x_2'\rho d\Psi dx_2' \tag{5.6}$$

where $x_1 = \rho sin(\theta_1)$,

$$I(\theta_1)\rho sin(\theta_1) d\theta_1 d\Psi = P(x_2')x_2'\rho d\Psi dx_2' \tag{5.7}$$

$$I(\theta_1)sin(\theta_1) d\theta_1 = P(x_2')x_2' dx_2'. \tag{5.8}$$

A relationship between the input angle and output location, $\theta(x_2')$, for any ray with a specified input and output power distribution can be calculated through integration of (5.8).

5.2.2.2 Algorithms Describing Path Length

The aperture phase distribution is a function of the distance each ray travels within the dual reflector system. Each ray travels from its source, is reflected of the sub-reflector and then the main-reflector, before reaching the aperture as shown in Figure 5.2. The total path length of each ray is expressed as

$$C_p(x_2') = r_1(\theta_1, y_1) + r_2(\theta_1, y_1, x_2, y_2) + r_3(x_2, y_2, x_2') + C_\theta(\theta_1) \tag{5.9}$$

where $C_p(x_2')$ represents the total path length of a ray cutting the aperture at x_2' and has an input phase $C_\theta(\theta_1)$. The total path length within the system comprises of the distance from the origin to the first reflector, r_1, the distance between the first and second reflector, r_2, and the distance between the second reflector and the aperture, r_3.

Expressions for r_1, r_2 and r_3 are obtained from Figure 5.2 as

$$r_1(\theta_1, y_1) = [\beta_y(\theta_1) - y_1]sec(\theta_1) \tag{5.10}$$

$$r_2(\theta_1, y_1, x_2, y_2) = \sqrt{(x_2 - x_1)^2 + (\alpha(\theta_1) + \beta_y(\theta_1) + y_2 + y_1)^2} \tag{5.11}$$

$$r_3(x_2, y_2, x_2') = \sqrt{(x_2' - x_2)^2 + y_2^2} \tag{5.12}$$

where β_x and β_y represent the point of origin for each ray. The offset between β_y and the second reflector is given by α. Ray intersection points on the reflectors are represented by x_1 and y_1 for the first reflector and x_2 and y_2 for the second reflector.

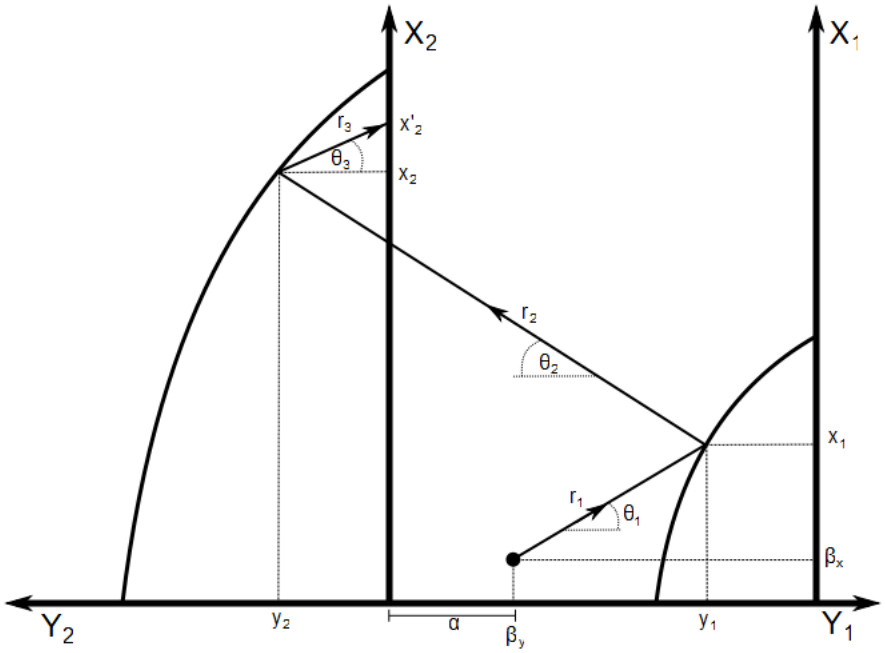

Figure 5.2: Cross-section diagram of dual reflector system

A surface normal to two consecutive rays is inserted at the aperture as shown in Figure 5.3. According to the theorem of Malus both rays have equal phase at this surface, leaving the difference in phase at the aperture between the rays equal to dC_p. With the distance between these rays on the x-axis equal to dx'_2, an expression for the relationship between dC_p and dx'_2 can be found as,

$$\frac{dC_p}{dx'_2} = sin(\theta_3) \tag{5.13}$$

which can be substituted into (5.12) to obtain

$$r_3 = \frac{y_2}{\sqrt{1 - (\frac{dC_p}{dx'_2})^2}}. \tag{5.14}$$

The path length of each ray within the system can now be expressed as a function of $\theta_1, y_1, x_1, x_2, y_2$ and x'_2. This will allow for a design where the system can be designed to deliver any required aperture phase distribution, C_p, for a given input phase distribution, C_θ.

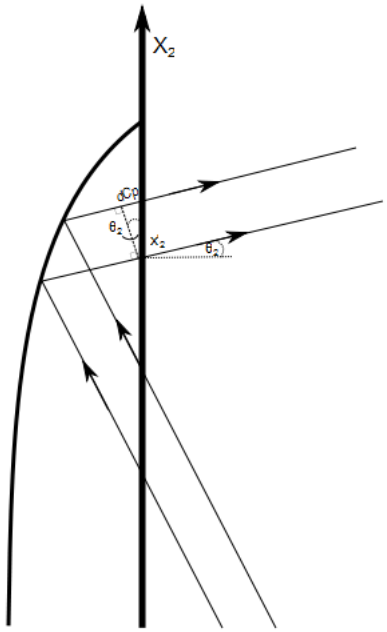

Figure 5.3: Diagram illustrating phase difference at aperture according to theory of Malus

5.2.2.3 Algorithms Describing Reflector Curvature

Each reflector's curvature is calculated to guide rays through the system as required by the conditions set through equations (5.8) and (5.9). The curvature of both reflectors is determined through the use of Snell's law. A straight line with a gradient of dy/dx is place at each point on the curvature as seen for the first reflector in Figure 5.4.

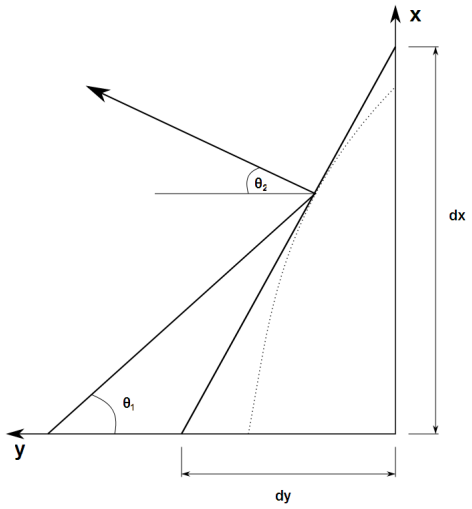

Figure 5.4: Diagram illustrating the reflection of a ray off a curved surface

Through the use of geometry, the gradients of both reflectors are expressed as a function of the respective ray's incident and reflected angle. An expression for the first reflector is obtained as

$$\frac{dy_1}{dx_1} = tan\left[\frac{\theta_1 - \theta_2}{2}\right] \tag{5.15}$$

and an expression for the second reflector is obtained as

$$\frac{dy_2}{dx_2} = -tan\left[\frac{\theta_2 - \theta_3}{2}\right] \tag{5.16}$$

where,

$$\theta_2 = -arctan\left[\frac{x_2 - x_1}{\alpha + \beta + y_2 - y_1}\right] \tag{5.17}$$

and

$$\theta_3 = -arctan\left[\frac{x_2' - x_2}{y_2}\right]. \tag{5.18}$$

Gradients for both curves are now expressed as functions of $\theta_1, y_1, x_1, x_2, y_2$ and x_2'.

5.2.2.4 Curve Expression Formulation

An expression is derived in which the expressions derived in sections 5.2.2.1, 5.2.2.2 and 5.2.2.3 are solved simultaneously. Reflector curves are synthesised from this expression which will be used in the dual shaped reflector design to achieve a specified power and phase aperture distribution for a given input power and phase distribution.

In order to solve the derived expressions simultaneously Galindo chose to use the expression dy_1/dx_2' to incorporate the required equations. This expression is expanded to

$$\frac{dy_1}{dx_2'} = \frac{dy_1}{dx_1}\frac{dx_1}{dx_2'}, \tag{5.19}$$

which is the product of (5.15) and dx_1/dx_2'. The term dx_1/dx_2' is further expanded to

$$\frac{dx_1}{dx_2'} = \frac{\delta x_1}{\delta \theta_1}\frac{d\theta_1}{dx_2'} + \frac{\delta x_1}{\delta y_1}\frac{dy_1}{dx_2'}. \tag{5.20}$$

An expression for x_1 is derived from Figure 5.2 as

$$x_1 = [\beta_y(\theta_1) - y_1]tan\theta_1 - \beta_x(\theta_1) \tag{5.21}$$

from where $\delta x_1/\delta y_1$ and $\delta x_1/\delta\theta_1$ in (5.20) can be derived,

$$\frac{\delta x_1}{\delta y_1} = -tan(\theta_1), \tag{5.22}$$

$$\frac{\delta x_1}{\delta \theta_1} = \frac{d\beta_y}{d\theta_1}tan(\theta_1) + (\beta_y(\theta_1) - y_1)sec^2(\theta_1) - \frac{d\beta_x}{d\theta_1}. \tag{5.23}$$

Substituting (5.20), (5.22) and (5.23) into (5.19),

$$\frac{dy_1}{dx_2'} = \frac{\left[\frac{d\beta_y}{d\theta_1}tan(\theta_1) - \frac{d\beta_x}{d\theta_1} + (\beta_y(\theta_1) - y_1)\,sec^2(\theta_1)\right]\frac{d\theta_1}{dx_2'}\frac{dy_1}{dx_1}}{\left(1 + \frac{dy_1}{dx_1}tan(\theta_1)\right)}, \tag{5.24}$$

gives an expression from which $y_1(x_2')$ can be derived after expressions for $\theta_1(x_2')$, $x_1(y_1, x_2')$, $y_2(y_1, x_2')$ and $x_2(y_1, x_2')$ are derived.

An expression for $\theta_1(x_2')$ can be derived from (5.8) by integrating both sides and using boundary conditions specified for $\theta_{1_{min}}, \theta_{1_{max}}, x'_{2_{min}}$ and $x'_{2_{max}}$,

$$\int_{\theta_{1_{min}}}^{\theta_1} I_1(\theta_1)sin\theta_1 d\theta_1 = K\int_{x'_{2_{min}}}^{x_2'} P(x_2')x_2'dx_2'. \tag{5.25}$$

Once $\theta_1(x_2')$ is obtained, $x_1(y_1, x_2')$ is derived from (5.21). Expressions for $y_2(y_1, x_2')$ and $x_2(y_1, x_2')$ is obtained by substituting (5.10) - (5.12) into (5.9) as shown in Appendix.C which gives

$$y_2 = -\frac{\left[(x_1 - x_2')^2 + (\alpha + \beta_y - y_1)^2 - B^2\right]}{2\left((\alpha + \beta_y - y_1) + \frac{\frac{dC_p}{dx_2'}(x_1 - x_2') + B}{\sqrt{1 - \left(\frac{dC_p}{dx_2'}\right)^2}}\right)} \tag{5.26}$$

$$x_2 = x_2' + \frac{[(x_1 - x_2')^2 + (\alpha + \beta - y_1)^2 - B^2]}{2\left((x_1 - x_2') + \frac{(\alpha + \beta_y - y_1)\sqrt{1 - \left(\frac{dC_p}{dx_2'}\right)^2} + B}{\left(\frac{dC_p}{dx_2'}\right)}\right)} \tag{5.27}$$

where

$$B = C_p - (\beta_y - y_1)sec\theta_1 - C_\theta(\theta_1). \tag{5.28}$$

Expressions for all the applicable variables with respect to x_2' and y_1 are now available to be used in (5.19). The differential equation of (5.19) is solved to obtain $y_1(x_2')$. With $y_1(x_2')$ obtained, values for x_1, x_2 and y_2 is calculated with which both curves are synthesised.

5.2.3 Numerical Solution to Dual Shaped Algorithms

Curves need to be synthesised from the derived expressions to be used in the dual shaped triple layer pillbox antenna. A numerical solution is required to solve for arbitrary input and output values of phase and power.

Matlab is used to obtain numerical solutions to (5.24) and (5.25). Results obtained from these equations are then used to obtain curves for both reflectors.

Second-order Trapezoidal integration is used to obtain $\theta_1(x_2')$ in (5.25). Figure 5.5 shows that this is an accurate method to solve (5.25) where $I(\theta_1)$ is arbitrarily chosen as $cos(\theta_1)$ and $P(x_2')$ as $cos\left(\frac{\pi}{2}\frac{x_2'}{x_{2_{max}}'}\right)$. The integral equation,

$$\int_0^{\theta_1} cos(\theta_1)sin(\theta_1)d\theta_1 = K\int_0^{x_2'} x_2' cos(\frac{\pi}{2}\frac{x_2'}{x_{2_{max}}'})dx_2', \tag{5.29}$$

is solved both analytically and numerically with boundary conditions $\theta_{min} = 0°$, $\theta_{max} = 40°$, $x_{2_{min}} = 0$ and $x_{2_{max}} = 1$, then compared in Figure 5.5. Both solutions give exactly the same result, proving that this numerical integration method works for this type of integral.

Equation (5.19) is a first-order, non-linear, differential equation. An accurate numeric method to solve this type of differential equation is the fourth order Runge-Kutta method, [17].Using the Runge-Kutta method and an initial value of $y_1(x_2' = x_{2max}') = 0$, $y_1(x_2')$ is calculated.

With $\theta_1(x_2')$ and $y_1(x_2')$ calculated, expressions for $y_1(x_1)$ and $y_2(x_2)$ can now be obtained from the equations derived in Chapter.5.2.2.4. Curves for both reflectors are now available to be implemented into the dual shaped triple layer pillbox.

5.2.3.1 Arbitrarily Shaped Curves as an Example

Curves are generated for arbitrary input and output values to test the procedure previously described. A constant phase distribution is chosen for the input and output of the system, with a single source point for all the rays. Boundary conditions of $x_2 = 1, x_1 = 0.4x_2$ and $\theta_1 = 30°$

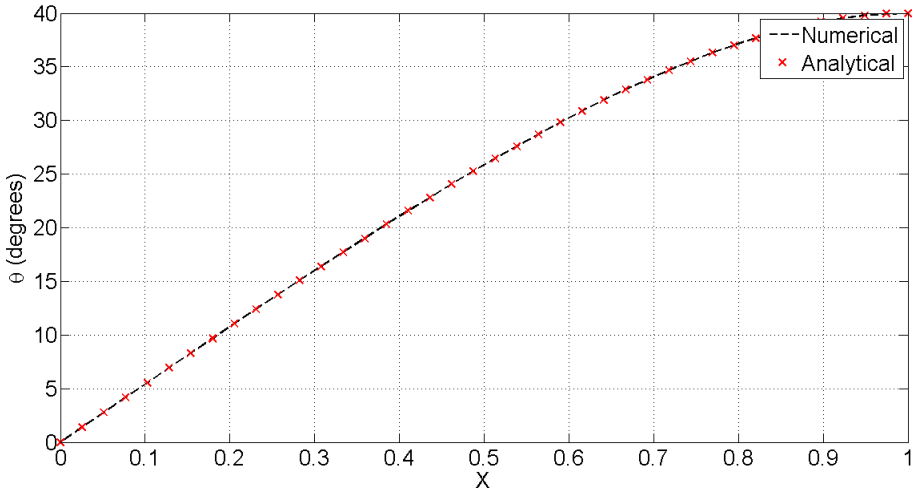

Figure 5.5: Trapezoidal integration compared to analytical results

are chosen arbitrarily. The input power distribution is set to $I(\theta_1) = cos^{16}(\theta_1)$ and the output power distribution to $P(x_2) = cos(\frac{\pi}{2}\frac{x_2}{x_{2max}})$ to obtain a realistic model.

Figure 5.6 shows the curves obtained from the above mentioned input values. It can be seen that the specified boundary conditions are met. There is however no data to show whether or not the required output phase and power distributions are obtained.

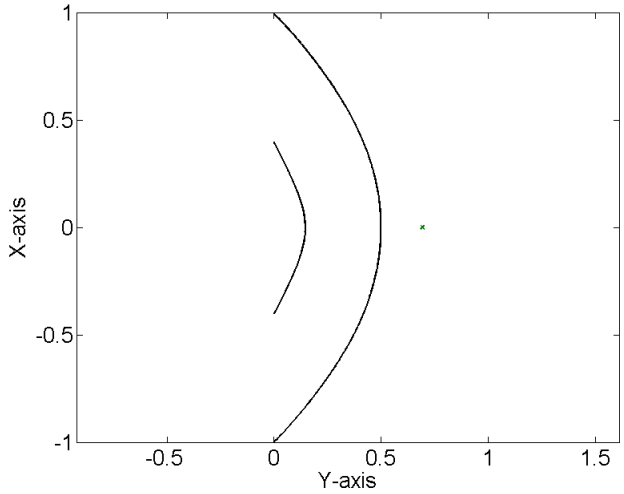

Figure 5.6: Dual shaped curves synthesised from arbitrary input and output values

5.2.4 Discussion on the Ray Tracing Procedure

An algorithm is required to verify that the synthesised curves would produce the required phase and power distributions at the aperture. This algorithm is obtained through the use of ray tracing algorithms.

A ray is launched from its starting position, $[\beta_y(\theta_1), \beta_x(\theta_1)]$, at an angle of θ_1 to the horizontal axis. The point at which the ray intersects with the sub-reflector is determined through interpolation. The gradient of the sub-reflector curve at the intersection point is used to calculate the ray's angle of incidence to the reflector. Using Snell's law the angle, θ_2, of the reflected ray to the horizontal axis can be determined. The same process is then repeated for the second reflection at the main-reflector, producing a value for θ_3 from which the position of the ray in the aperture, x_2', can be determined. This process is repeated for a number of rays to acquire the distribution for the entire aperture.

With the intersection value of each ray with the aperture, x_2', and its input angle, θ_1, known, the expression $\theta_1(x_2')$ is obtained. From (5.8) the power distribution at the aperture can be calculated from

$$P(x_2') = \frac{I(\theta_1) sin\theta_1}{x_2'} \frac{d\theta_1}{dx_2'}. \tag{5.30}$$

The aperture phase is calculated from the sum of the input phase, $C_\theta(\theta_1)$, and the phase delay within the system, $r_t(\theta_1)$, as

$$C_p(x_2) = C_\theta(\theta_1) + r_t(\theta_1), \tag{5.31}$$

where the total phase delay within the system is calculated from the path length of each ray.

5.2.4.1 Ray Tracing for Arbitrarily Shaped Curves

The derived ray tracing algorithm is used on the curves synthesised in Chapter.5.2.3.1 to verify whether the dual shaped curves yield the required aperture distribution.

To illustrate the ray paths within the dual curved system, a few rays are plotted in Figure 5.7. This graph is however not useful by itself other than providing a means to visualize the internal working of the curved system.

Figure 5.8 compares the required aperture distribution to the distribution acquired through ray tracing. The realised aperture distribution mostly agrees with the specified distribution.

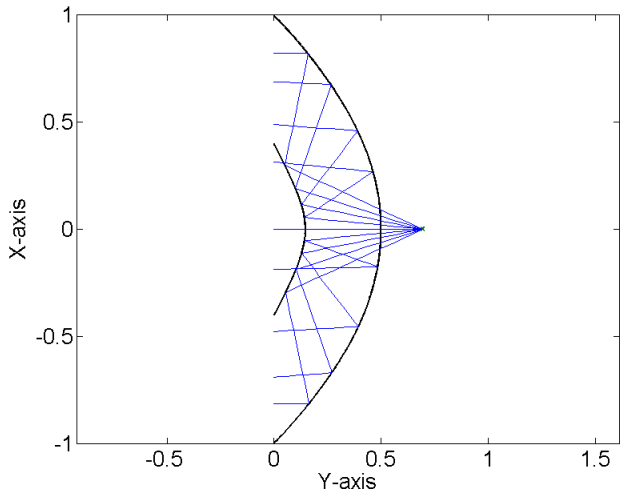

Figure 5.7: Arbitrary dual shaped curves with ray tracing

There are some variations from the intended power distribution at the edges and bore-site, $\theta_1 = 0°$. The variation at bore-site is due to the gradient of the curve becoming zero, causing a mathematical problem due to division by zero occurring. Variations at the edges are probably due to inaccurate calculations of the ray trajectories which causes some rays inbound at the edge of the reflector to 'miss' the reflector. This causes discontinuities in $\theta(x_2')$ which in turn causes irregularities in the calculated power distribution. The phase distribution shows noise caused by the abovementioned inaccurate calculations. A variation of $0.08°$ from the constant phase required is obtained which could be attributed to errors in the ray tracing algorithm.

Through ray tracing the working of the synthesised curves is verified by yielding the same results as are required from the dual shaped curves.

5.2.5 Calculating Input Values for Dual Shaped Algorithms

For the synthesised curves to be successfully implemented into a practical antenna design, arbitrary input values cannot be chosen for the system. It cannot be assumed that all rays necessarily originate from the same source point, $\beta(\theta_1)$, and thus the source point of each ray needs to be calculated. Accurate values of the input phase, $C_\theta(\theta_1)$, and power, $I(\theta_1)$, for the system needs to be obtained.

Fields are obtained on a straight line within the feed through the use of *CST MWS*. These fields are acquired for a Cartesian coordinate system and it is thus necessary to transform these

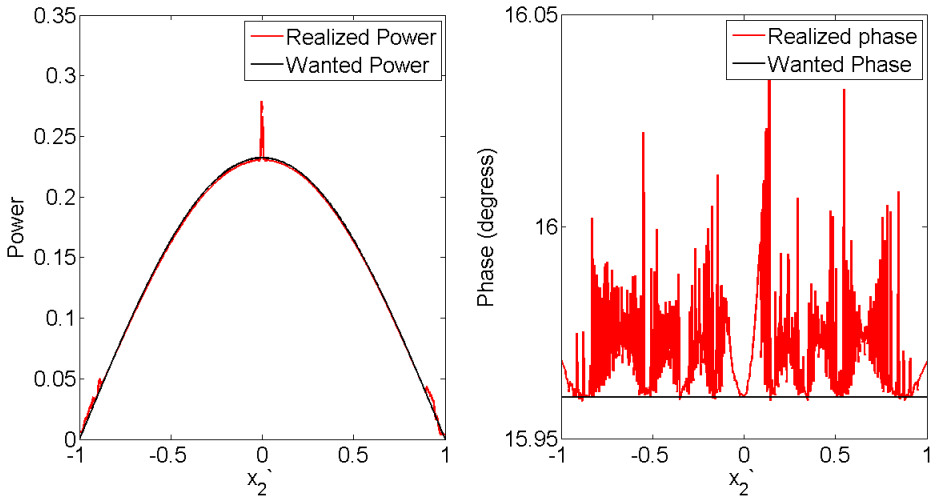

Figure 5.8: Aperture distribution of arbitrary dual shaped curves

fields to a polar coordinate system to be used as an input to the curve synthesis algorithm. To obtain $x(\theta)$, the angle of each ray incident on the straight line must be obtained as seen in Figure 5.9. This can be done by calculating the Poynting vector [15] at each point on the line or by taking the gradient of the phase difference between consecutive rays using the theorem of Malus to find its origin. The transformation can also be done by doing a near to far-field transform on the fields along the line, it was however decided not to do this as this is not a free space problem.

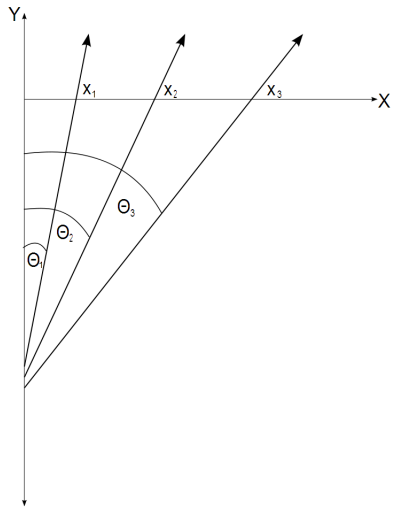

Figure 5.9: Diagram illustrating the rays incident on measurement line at different angles on incidence

5.2.5.1 Deriving Expressions Relating Radial to Cartesian Coordinates, $x(\theta)$

Using *CST MWS* the tapered waveguide used for the feed of the system is extended and terminated with an open boundary, Figure 5.10. The E and H fields are measured on a line running parallel to the aperture at the position that the sub-reflector would be. Probes are positioned at the centre and edge of the measurement line which enables the *Transient Solver* to be aborted as soon as the forward travelling wave passes both probes, Figure 5.11. The primary purpose of the centre probe is to verify that no reflections of the boundary pass the measurement line while the signal is still passing through the edge probe. This reduces unwanted reflections from the terminated boundary and yields only the desired forward travelling wave.

The complex Poynting vector is derived from the E and H fields through,

$$S = \frac{1}{2}[E \times H^*], [15]. \tag{5.32}$$

According to Stutzman [15] only the *real* part of the complex Poynting vector is used for this application,

$$S = \frac{1}{2}Re[E \times H^*] \tag{5.33}$$

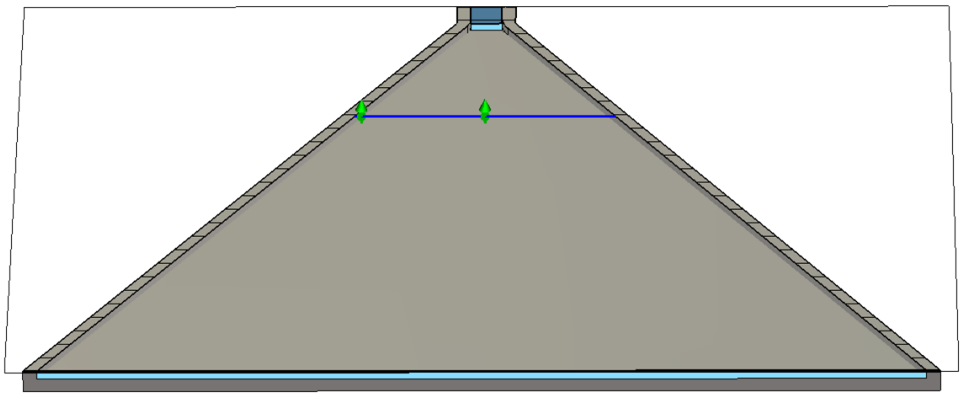

Figure 5.10: Model of feed containing measurement line and probes

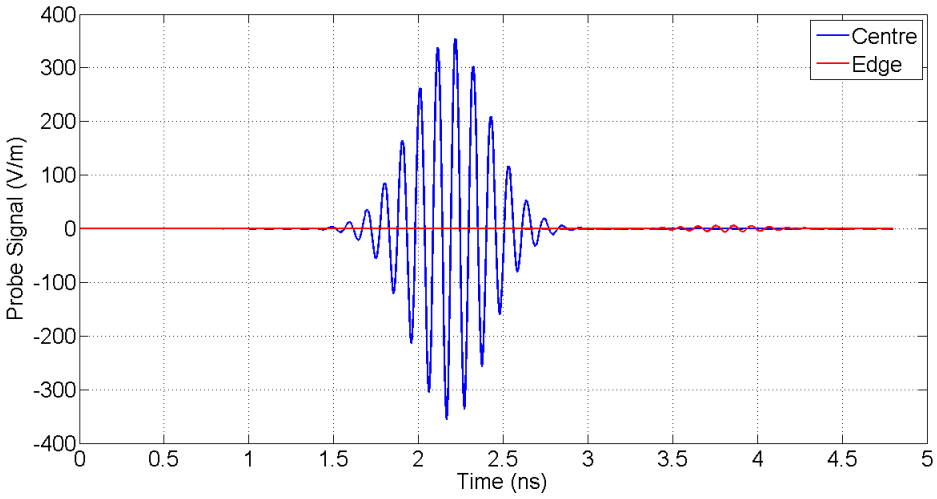

Figure 5.11: Signal passing through probes positioned at the edge and centre of the measurement line within the feed

where S is a vector with components in the x, y and z directions. It is assumed that the y component is insignificant due to the parallel plates of the feed. Each ray's angle is determined through

$$\theta = tan^{-1}\left(\frac{S_x}{S_z}\right), \tag{5.34}$$

which is derived from the diagram in Figure 5.12. With the incident angle of each ray determined and each ray's position on the measurement line known, $x(\theta)$ is obtained, shown

in Figure 5.13.

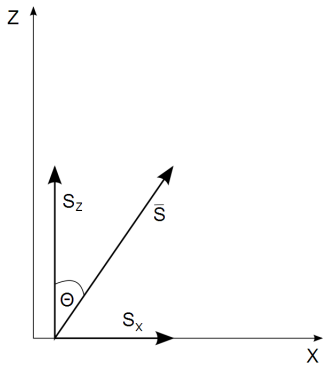

Figure 5.12: Diagram illustrating the use of Poynting vectors to calculate the incident angle of a ray

The angle of incidence is obtained from the phase front at the measurement line for validation purposes. The phase is obtained from the y component of the E-field, measured at this location. To determine the angle of incidence of each ray, the difference in phase between consecutive rays is first transformed to a length. Transformation from phase to length is done by dividing by the wavenumber, k. The angle of incidence is calculated from (5.35) using the difference in phase, dC, between consecutive rays and their respective distance from each other on the line, dx. Figure 5.13 shows the relationship between the incident angle of rays to their respective interception point on the measurement line.

$$\theta = sin^{-1}\left(\frac{dC}{dx}.\frac{1}{k}\right) \tag{5.35}$$

From Figure 5.13 it can be seen that both techniques yield the same results. A polynomial can be fitted on either curve to reduce the noise found on the curve. With $x(\theta)$ obtained, fields obtained along the measuring line can be transformed to polar coordinates.

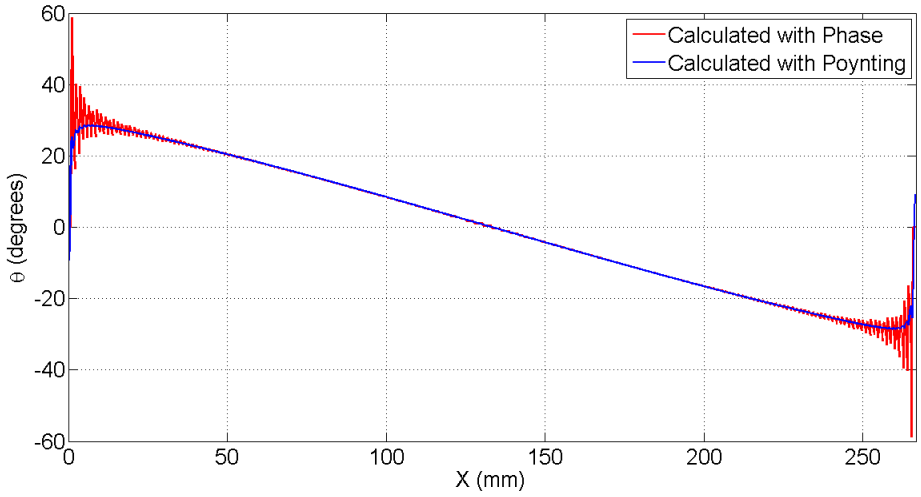

Figure 5.13: Incident angle of rays relative to position on measurement line, calculated with Poynting vectors together with phase gradients

5.2.5.2 Obtaining each Ray's Point of Origin

Each ray bundle is considered to comprise two consecutive rays. The intersection point of these two rays is taken as the point of origin of the ray bundle.

Each ray's point of origin is determined from the values calculated for $x(\theta)$. The expressions for the two consecutive rays are solved simultaneously to obtain the coordinates for the intersection point and hence the point of origin of the ray tube,

$$\beta_x = \frac{X_1 cot(\theta_1) - X_2 cot(\theta_2)}{cot(\theta_1) - cot(\theta_2)} \tag{5.36}$$

$$\beta_y = (\beta_x - X_1) cot(\theta_1). \tag{5.37}$$

Here θ_1 and X_1 are the angle and measurement line intersection point of the first ray, whereas θ_2 and X_2 are the angle and measurement line intersection point of the second ray.

The point of origin for a couple of rays is determined from (5.36) and (5.37) and shown in Figure 5.14. It is noted that the source points of rays closer to the edge of the measurement line vary more from the expected value than that of rays closer to the middle of the measurement line.

Values for $\beta_x(\theta)$ and $\beta_y(\theta)$ relative to the input angle which is needed for the input model of

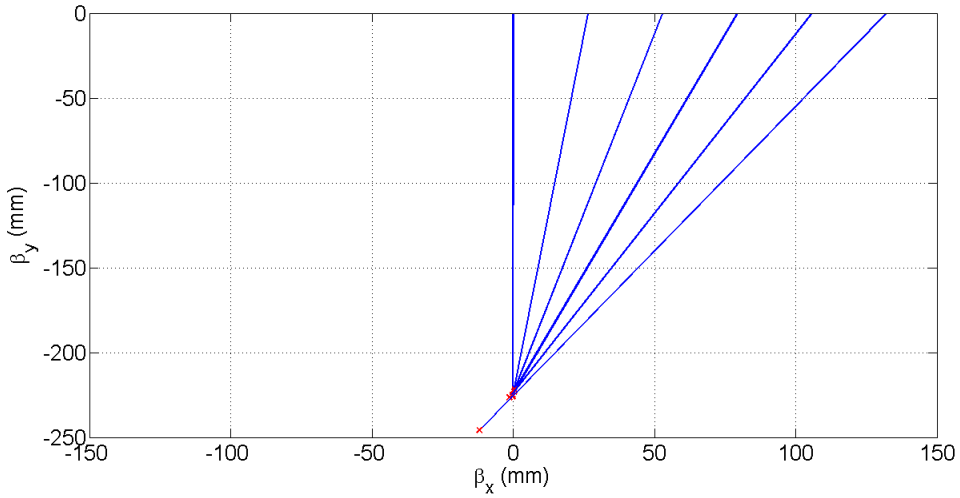

Figure 5.14: Rays plotted from their origin to their interception with the measurement line

the antenna can be found in Figure 5.15.

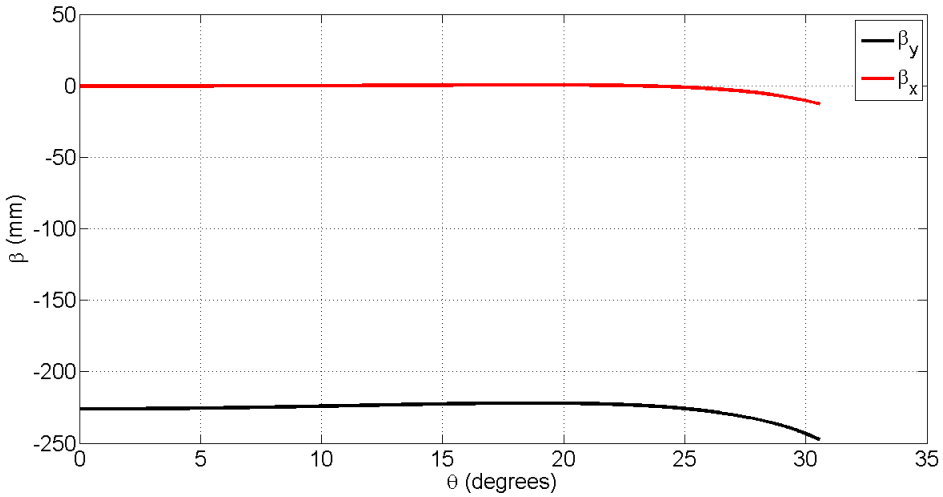

Figure 5.15: Ray source points relative to their angle of incidence

5.2.5.3 Input Phase and Power Distribution

The input phase, $C(\theta)$, and power distribution, $I(\theta)$, at the source of the feed model need to be determined. Values for the phase, $C(x)$, and power, $I(x)$, obtained from the measurement line are traced to the feed model's source and transformed from Cartesian to polar coordinates.

The phase along the measurement line, $C(x)$, is obtained from the acquired E-field's y component, whereas the power along the line, $I(x)$, is obtained from the Poynting vector components derived in (5.33) through

$$P = \sqrt{S_x^2 + S_y^2 + S_z^2}. \tag{5.38}$$

$I(x)$ and $C(x)$ are transformed to $I(\theta)$ and $C(\theta)$ through the use of values obtained for $x(\theta)$ in Chapter.5.2.5.1. With the power and phase known at the measurement line with respect to the incident angle, it needs to be translated to the feed model's source to be used as an input to the dual shaped curve synthesis algorithm. To translate the power and phase to the origin, the path length of each ray from the source to the measurement line is required. The ray length, R, is calculated with geometry as

$$R(\theta) = \sqrt{(x(\theta) - \beta_x(\theta))^2 + (\beta_y(\theta))^2}. \tag{5.39}$$

To obtain the phase at the source of the feed, the ray length, R, is transformed to a phase delay and added to the phase obtained at the measurement line,

$$C_\theta(\theta) = C(\theta) + R(\theta) * k. \tag{5.40}$$

The power distribution at the source is obtained by compensating for the power dissipation that occurs over the ray's length. Power dissipation is calculated using the Conservation of energy principle. Using the diagram in Figure 5.16, the power dissipation from one point to another can be expressed as

$$I_1(\theta)A_1 r_1 sin(\theta) = I_2(\theta)A_2 r_2 sin(\theta), \tag{5.41}$$

where

$$A_1 = r_1 d\theta * r_1 d\Psi \tag{5.42}$$

$$A_2 = r_2 d\theta * r_2 d\Psi. \tag{5.43}$$

Substituting (5.42) and (5.43) into (5.41) gives

$$I_1(\theta) = I_2(\theta)\left(\frac{r_2}{r_1}\right)^3 \tag{5.44}$$

where r_1 can be any arbitrary number as long as it is constant for all values of θ and r_2 is the distance from the ray source to the measurement line, $R(\theta)$.

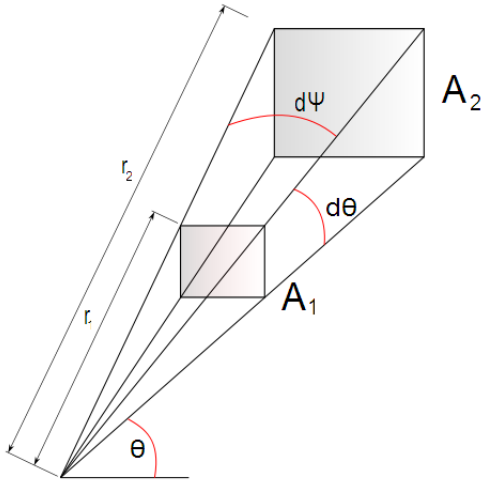

Figure 5.16: Diagram to illustrate the power dissipation occurring in a ray bundle over distance

Both the power and phase distributions at the source of the feed is now available, Figure 5.17, to be used as input values for the dual shaped curve synthesis algorithm. The power distribution can be normalised since the effect of the magnitude is removed through the constant, K, from (5.25) during the curve synthesis procedure.

5.2.6 Conclusion on the Dual Shaped Algorithm

An algorithm has been derived with which curves are synthesised to deliver a required aperture power and phase distribution for a given source power and phase distribution. The synthesised curves were tested through the use of ray-tracing algorithms and found to yield the required results.

Algorithms were derived to obtain the power and phase distributions at the source of the feed to be used in the curve synthesis algorithm. This allowed fields simulated along a line to

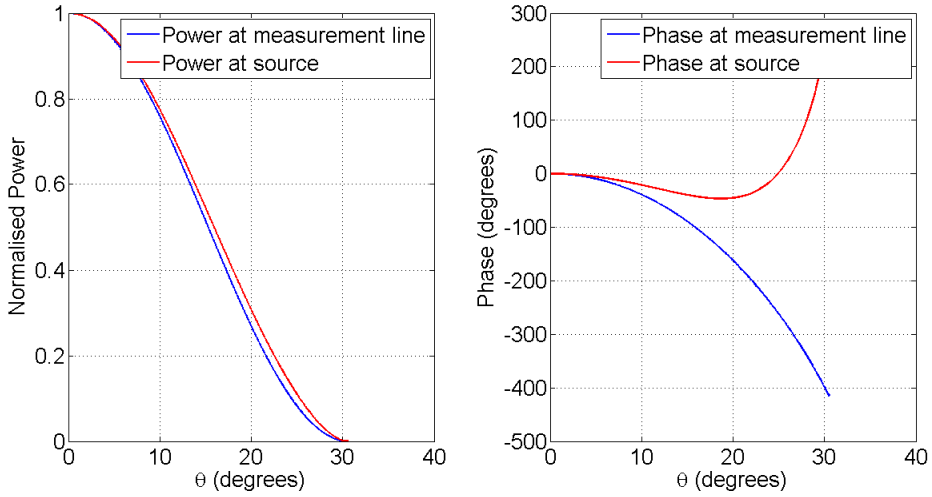

Figure 5.17: Power and phase distribution at the source of the feed

be transformed to rays with respective values for the point of origin, phase and power to be obtained.

The algorithms were solved numerically using *Matlab*, allowing for arbitrary input and output distributions.

5.3 Dual Shaped Reflector Triple Layer Pillbox Antenna

In this section dual reflector shaping is implemented into a triple layer pillbox design to achieve a certain aperture distribution. Two antennas are designed for different radiation pattern characteristics. A low side-lobe antenna will first be designed to achieve as low side-lobe levels as possible and then a high gain antenna will be designed to achieve maximum gain.

The designed antennas are evaluated using simulation. Further verification is done by repeating the design process to obtain low side-lobes for different sized antennas. Simulation results are verified through comparison between *CST* and *FEKO* results.

5.3.1 Design of Dual Shaped Triple Layer Pillbox Antenna

For this design a constant aperture phase distribution is required for both antennas. To achieve the desired far-field patterns an aperture magnitude distribution is required that would yield the low side-lobes in the azimuth far-field pattern for the one antenna and high gain for the other antenna.

The triple layer pillbox model is adapted to implement the dual shaped reflectors. The parabolic reflector in the second bend is replaced by the main-reflector, whereas the straight reflector in the first bend is replaced by the sub-reflector.

The size of the antenna needs to be chosen to be large enough to make the antenna electrically large enough for the principles of geometric optics to still apply. For design purposes the antenna must be small enough for reasonable simulation times. It was decided to use an aperture width of 20λ for the antenna.

5.3.1.1 Design of Dual Shaped Antenna with Low Side-lobes

The low side-lobe antenna's sub-reflector width is chosen rather arbitrarily as 40% of the main reflector's width. This value needs to be large enough for the principle of geometric optics to remain applicable. For the reflector to focus energy to the centre of the aperture effectively, the sub-reflector's width cannot be too large relative to the main-reflector's width. The feed taper is arbitrarily chosen as $30°$.

The power distribution must be chosen to yield low side-lobes, yet be practical to implement. For the distribution to be practical it cannot have non-zero amplitude at the edges of the aperture. Since a non-zero power distribution cannot exist at a metal boundary, designing for such a distribution will force the rest of the aperture distribution to become distorted. It is also difficult

to acquire low amplitude distributions across large parts of the aperture since internal reflections and scattering will cause distortions on these parts.

A Gaussian distribution with $\alpha = 4.3$ is chosen for the aperture power distribution. This distribution has low power at the edge of the aperture as seen in Figure 5.18. Theoretical side-lobes of less than $-90dB$ are obtained for this distribution, Figure 5.18. Errors occurring in the curve synthesis procedure together with internal reflections and scattering within the antenna structure will however make such low side-lobes unattainable.

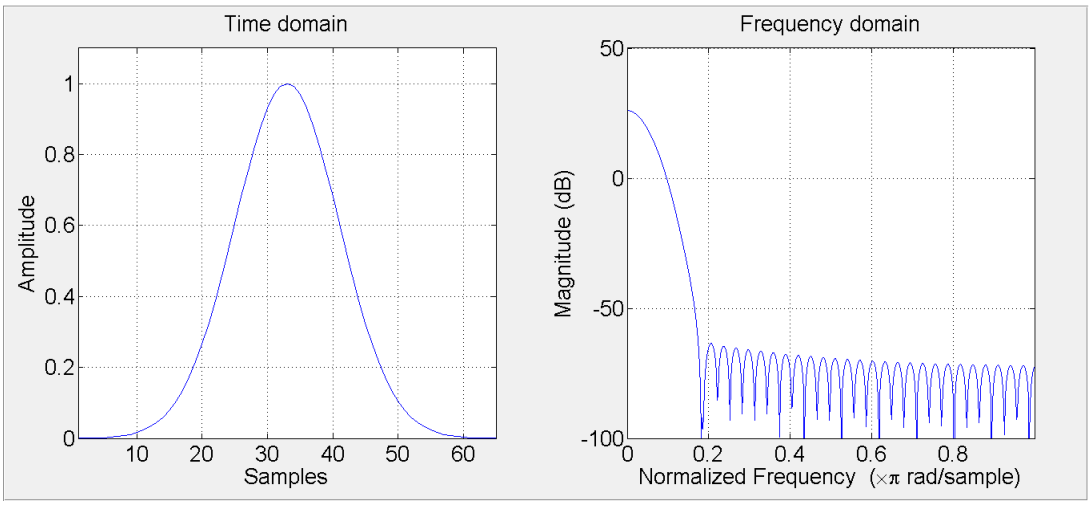

Figure 5.18: Proposed power distribution at aperture of low side-lobe antenna, together with its theoretical far-field pattern

The final designed model of the triple layer pillbox antenna with low side-lobes is shown in Figure 5.19. Better usage of space can be made by increasing the feed's angle or reducing the size of the sub-reflector relative to the main-reflector. These changes could however cause an increase in the sub-reflector's depth, causing the limited change in the antenna's dimensions.

5.3.1.2 Design of Dual Shaped Antenna with High Gain

For the high gain antenna, the sub-reflector width is again chosen rather arbitrarily, this time as 30% of the main reflector's width. For this sub-reflector width, a feed taper of 30° is found to be optimal to acquire minimal antenna dimensions.

Although a rectangular power distribution at the aperture would yield the highest gain, this distribution requires non-zero power at the edges of the aperture. It was decided to rather use

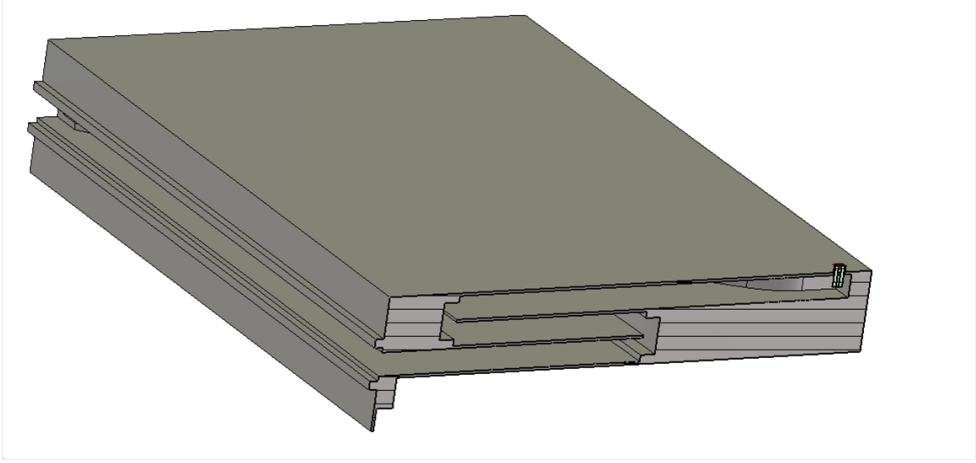

Figure 5.19: Model of Dual Shaped Triple Layer Pillbox with low side-lobes

a cosine distribution as shown in Figure 5.20. This distribution should yield a higher gain than was obtained for the Gaussian distribution, used for low side-lobes, but should theoretically yield higher relative side-lobes of $-23dB$.

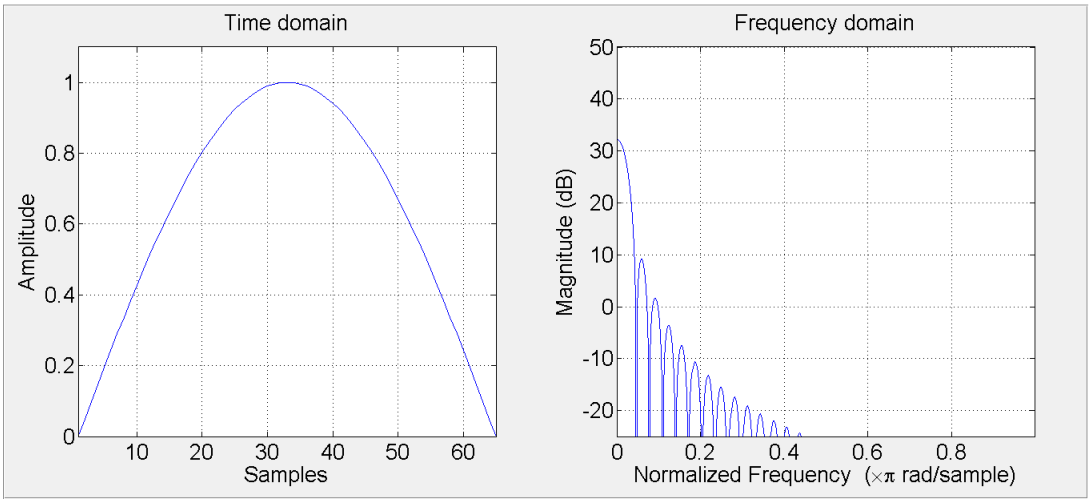

Figure 5.20: Proposed power distribution at aperture of high gain antenna together with its theoretical far-field pattern

The designed model for the shaped triple layer pillbox antenna with high gain is shown in Figure 5.21. This design is more compact than found for the low side-lobe antenna due to the power being more spread over the aperture.

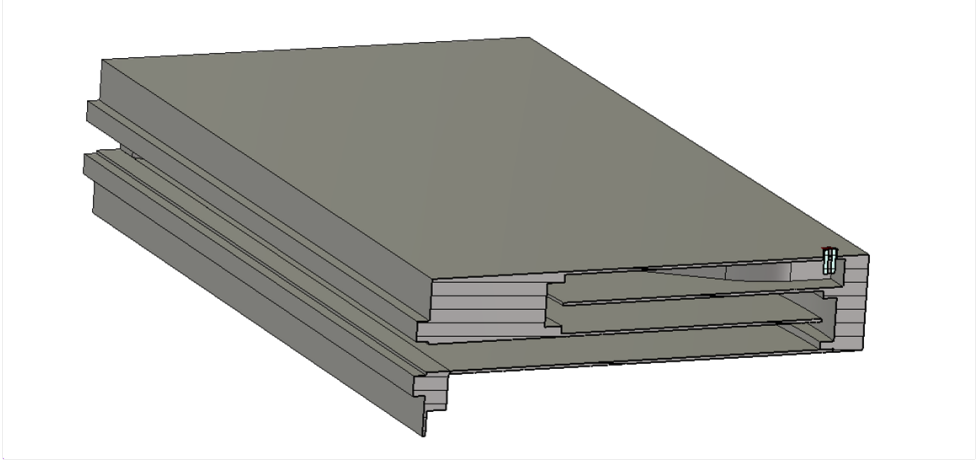

Figure 5.21: Model of Dual Shaped Triple Layer Pillbox with high gain

5.3.2 Simulated Results of Dual Shaped Triple Layer Pillbox Antenna

The synthesised sub-reflector and main-reflector curves are implemented into the CST model used for the triple layer pillbox antenna. Power and E-field measurements are taken on a measurement line, positioned in the aperture, to compare with the requested values. Far-field results are obtained to determine the antenna's performance.

5.3.2.1 Simulated Results of Dual Shaped Antenna with Low Side-lobes

A reflection coefficient of less than $-25dB$ is obtained in Figure 5.22 for the required frequency band. This result is a good indication of whether or not the fields in the structure are behaving as assumed in the synthesis process. From this result it can be seen that the structure is well adapted.

The magnitude of the aperture power distribution at centre frequency is compared to the required Gaussian distribution in Figure 5.23. The power distribution does have some differences to the required distribution which could be due to internal reflections, scattering or an error made in the feed model. Figure 5.24 shows that the aperture phase distribution is relatively flat, as required.

The purpose of this design was to obtain low side-lobes in the azimuth far-field pattern. From Figure 5.25 the antenna performs well at the designed frequency of $9.5GHz$, with side-lobes of less than $-40dB$. The side-lobe levels are higher away from centre frequency with relative side-

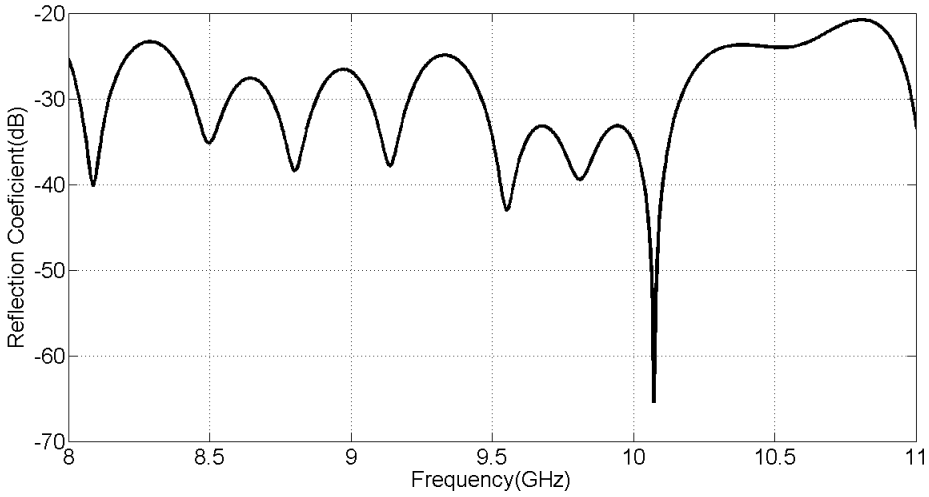

Figure 5.22: Simulated reflection coefficient of Dual Shaped Pillbox antenna with low side-lobes

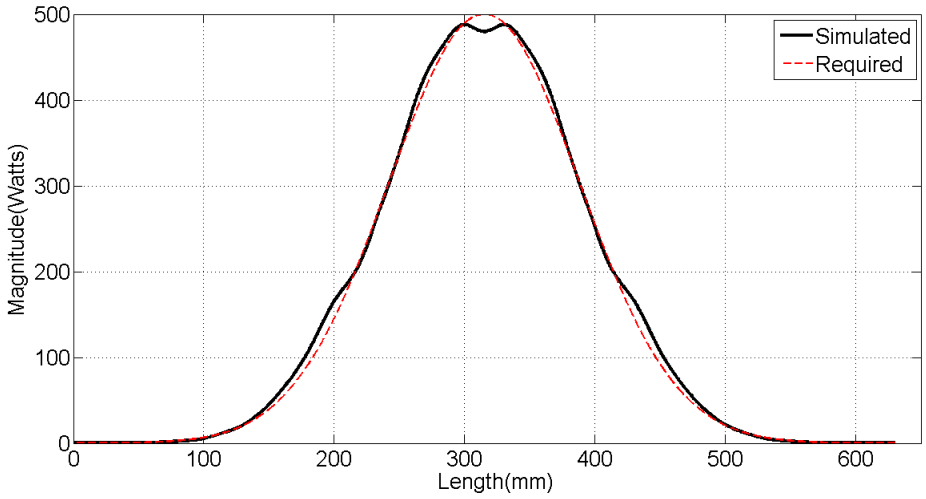

Figure 5.23: Simulated aperture power distribution of Dual Shaped Pillbox antenna with low side-lobes

lobes of $-27.9dB$ at $10.5GHz$ and $-37dB$ at $8.5GHz$. Figure 5.25 also shows that the antenna has a gain of $20.3dBi$ at centre frequency.

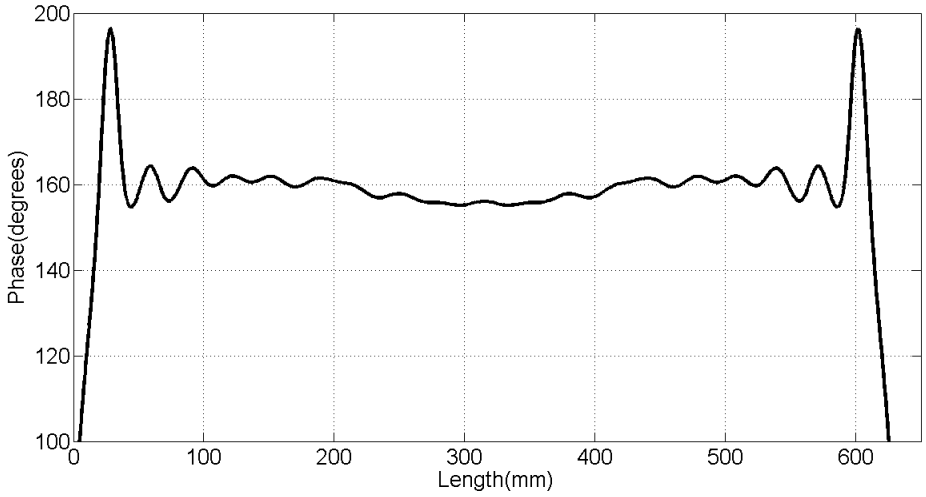

Figure 5.24: Simulated aperture phase distribution of Dual Shaped Pillbox antenna with low side-lobes

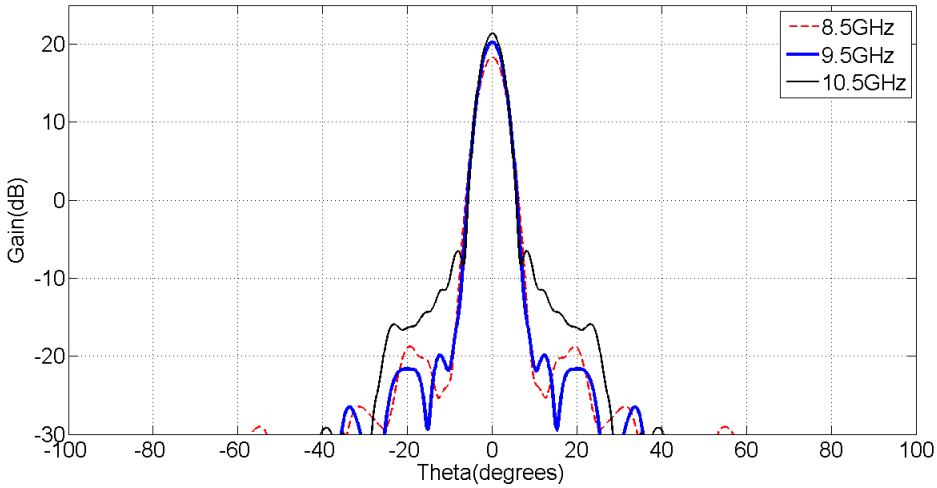

Figure 5.25: Simulated azimuth far-field result at centre frequency of Dual Shaped Pillbox antenna with low side-lobes

5.3.2.2 Simulated Results of Dual Shaped Antenna with High Gain

The reflection coefficient in Figure 5.26 shows that the high gain antenna is also well matched with a reflection coefficient of less than $-20dB$ over the $2GHz$ frequency band.

A relatively flat aperture phase distribution is found in Figure 5.27, with a variation of about 20° over the aperture. The aperture power distribution does not correlate as well with the required cosine distribution in Figure 5.28, this could be due to the difficulty in acquiring power

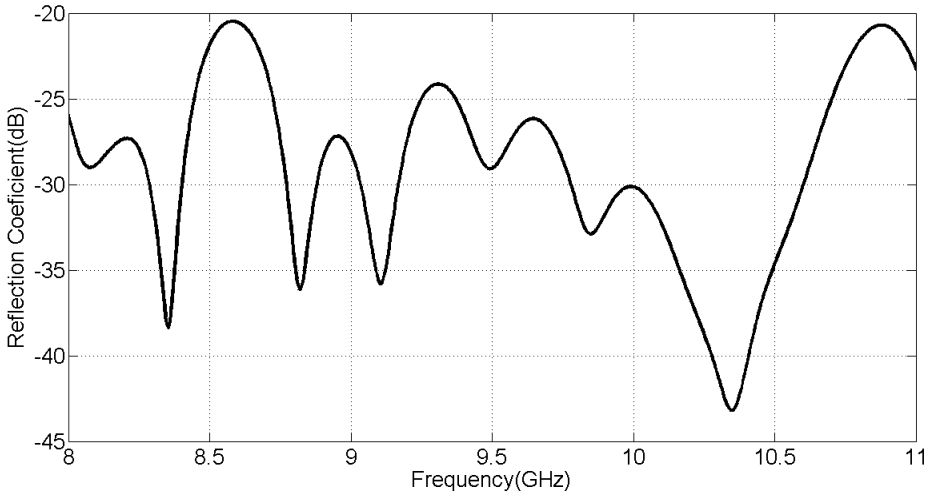

Figure 5.26: Simulated reflection coefficient of Dual Shaped Pillbox antenna with high gain

at the edges of the aperture where the power is forced down as seen in the simulated results.

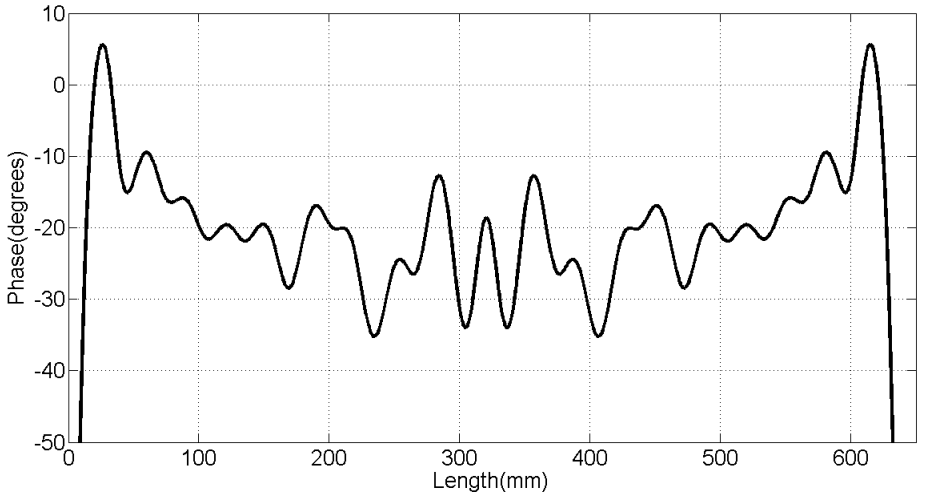

Figure 5.27: Aperture phase distribution of Dual Shaped Pillbox antenna with high gain

Figure 5.29 shows the azimuth far-field pattern where a gain of $22.3dBi$ is obtained at centre frequency. This design yields $2dB$ more gain than was acquired for the low side-lobe antenna. The side-lobe level is about $-19dB$ at centre frequency which is more than the theoretical $-23dB$.

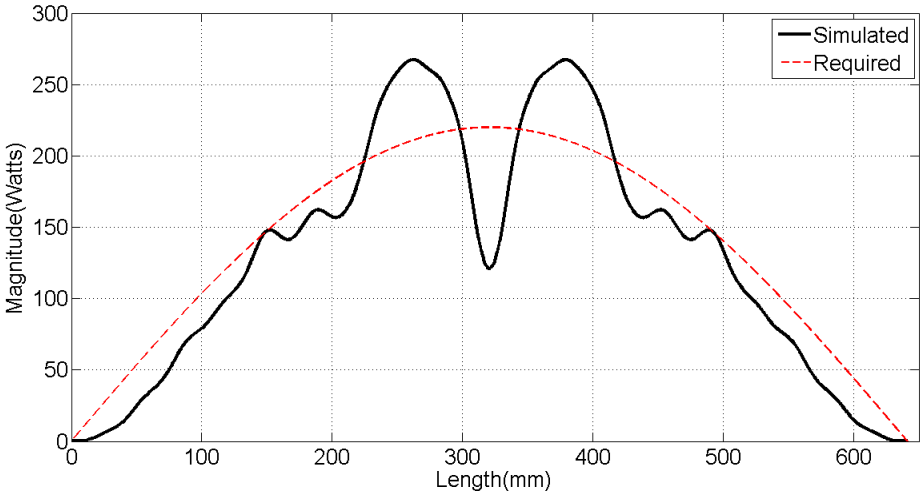

Figure 5.28: Aperture power distribution of Dual Shaped Pillbox antenna with high gain

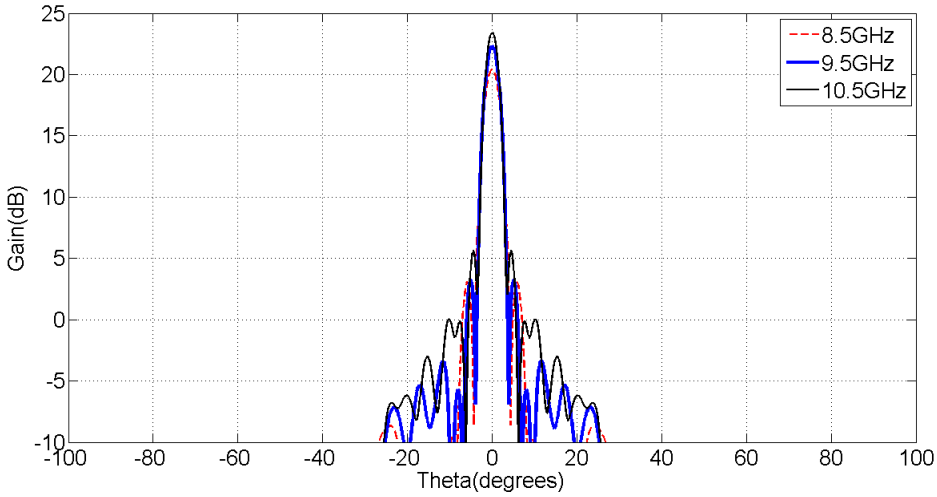

Figure 5.29: Azimuth far-field pattern of Dual Shaped Pillbox antenna with high gain

5.3.2.3 Further Confirmation of Effectiveness of Dual Reflector Shaping

The simulated results are verified through the use of *FEKO* which uses a different solver algorithm than *CST*. The low side-lobe antenna design is adapted to have zero plate thickness and solved with *CST* and *FEKO*. Azimuth far-field radiation patterns simulated using both *CST* and *FEKO* at centre frequency are shown in Figure 5.30. Results show a $-40dB$ correlation down

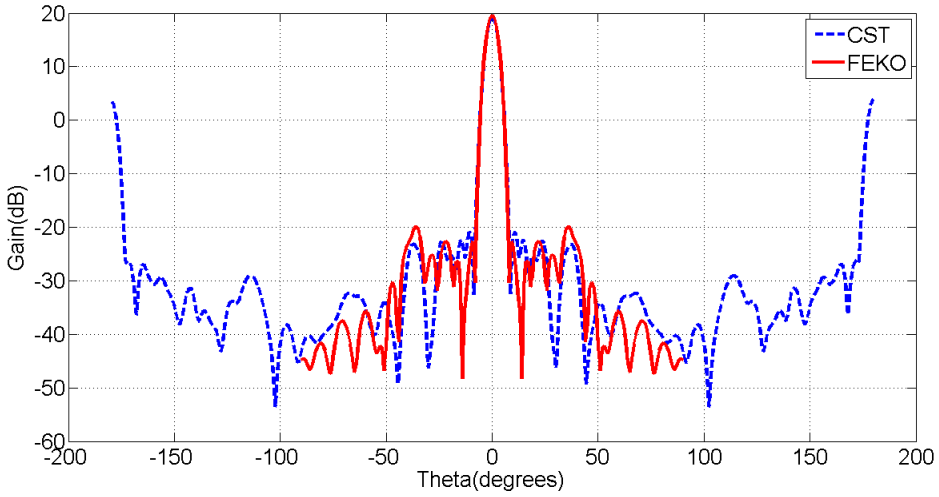

Figure 5.30: Azimuth far-field pattern at centre frequency of low side-lobe Dual Shaped Pillbox antenna, simulated using *CST* and *FEKO*

the main beam.

To show that the process is repeatable, the dual shaped pillbox is designed to have low side-lobes for different aperture widths. The antenna is designed for an aperture width of 10λ, 20λ and 40λ. Azimuth far-field results in Figure 5.31 show that the antenna maintains $-40dB$ side-lobes for the different sizes, proving repeatability.

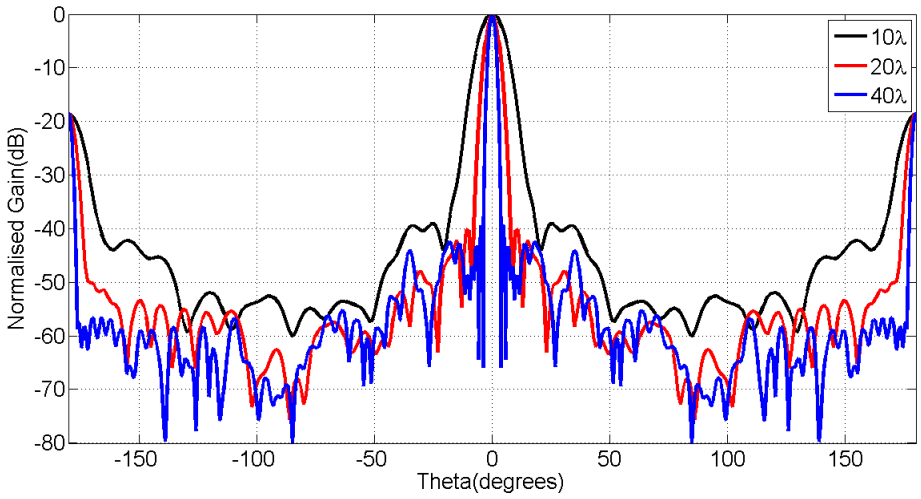

Figure 5.31: Azimuth far-field result at centre frequency of low side-lobe Dual Shaped Pillbox antenna designed for different sizes

5.3.3 Conclusion on the Design of a Triple Layer Pillbox using Dual Reflector Shaping

Dual reflector shaping was used to design a dual shaped triple layer pillbox antenna with different aperture distributions to achieve a desired azimuth far-field pattern. Two antennas were designed, one with low side-lobes and another with high gain.

Side-lobes of $-40dB$ were obtained through simulation at centre frequency for the low side-lobe antenna. These results were verified through comparison between *FEKO* and *CST* simulations. Repeatability was proven by obtaining the same results for different sized antennas.

Designing for higher gain yielded an antenna with $2dB$ more gain than that acquired for the low side-lobe design. Side-lobes were found to be close to the expected value for the distribution used.

It was thus proven through simulation that dual reflector shaping allows for some control over the aperture distribution of a triple layer pillbox antenna and thus its radiation pattern.

5.4 Dual Shaped Reflector Triple Layer Pillbox Measurements

Both the high gain and low side-lobe dual shaped pillbox antennas are manufactured with stacked laser-cut aluminium plates through the same process described in Chapter 4.5. It was decided to use four 2mm aluminium plates instead of 8mm plates for the high gain antenna to save time from manually drilling holes while also increasing accuracy.

Near-field measurements are done for both antennas after which a near- to far-field transform is done as described in Chapter.4.5. Gain measurements are done on both antennas to determine whether the high gain antenna yields a higher gain than the low side-lobe antenna does.

5.4.1 Gain Measurement Theory

The *'Three-antenna measurements technique'* described in [10] is used to determine the antenna gain. This technique requires the use of a third antenna of which the gain is known. Near-field measurements are done for both the AUT and the reference antenna. The spacing between both the antennas and the probe need to be kept the same for both measurements.

Equation (5.45), [10], is used to calculate the antenna gain, G_{AUT}. G_{SGH} is the known gain of the reference antenna in dB. P_{AUT} and P_{SGH} are respectively the received power for the AUT and reference antenna, obtained from the near-field measurements.

$$G_{AUT} = G_{SGH} + 10log_{10}\left(\frac{P_{AUT}}{P_{SGH}}\right) \tag{5.45}$$

The total received power, $10log_{10}(P)$, can be expressed as $20log_{10}(E_{tot})$, removing the need to transform the measured E-fields to power. E_{tot} is the total E-field intensity in the far-field, calculated through

$$E_{tot} = \oint E(k_x, k_y)dk_x dk_y, \tag{5.46}$$

where $E(k_x, k_y)$ is obtained from the measured E-field through a near- to far-field transform. Equation (5.45) can thus be simplified to

$$G_{AUT} = G_{SGH} + 20log_{10}\left(\frac{Etot_{AUT}}{Etot_{SGH}}\right). \tag{5.47}$$

The reference antenna used is a Marconi Horn which has a known gain of $17.3dB$ at $9.5GHz$. Figure 5.32 shows the measured elevation and azimuth far-field patterns of the Marconi horn at $9.5GHz$ which was calculated from 2-D near-field measurements, taken at 70mm from the

antenna. From the elevation pattern it can be seen that the antenna was not aligned correctly and is squinting upwards. The total E-field received, $20log_{10}(Etot_{SGH})$, is calculated as $170dB$.

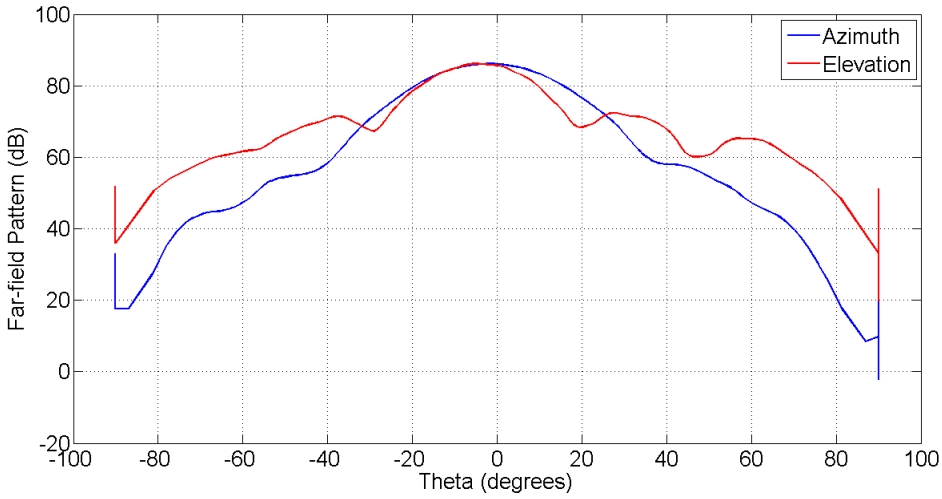

Figure 5.32: Measured far-field pattern of Marconi Horn

5.4.2 Measurements of Dual Shaped Antenna with Low Side-lobes

The dual shaped pillbox antenna with low side-lobes is measured with the same process used to measure the triple layer pillbox antenna in Chapter.4.5. The measurement setup is shown in Figure 5.33. The normalised 2-D near-field pattern, measured at 70mm is shown in Figure 5.34.

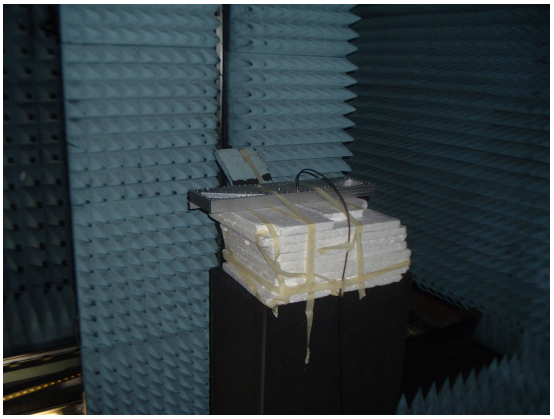

Figure 5.33: Measurement of Dual Shaped Triple Layer Pillbox antenna in anechoic chamber

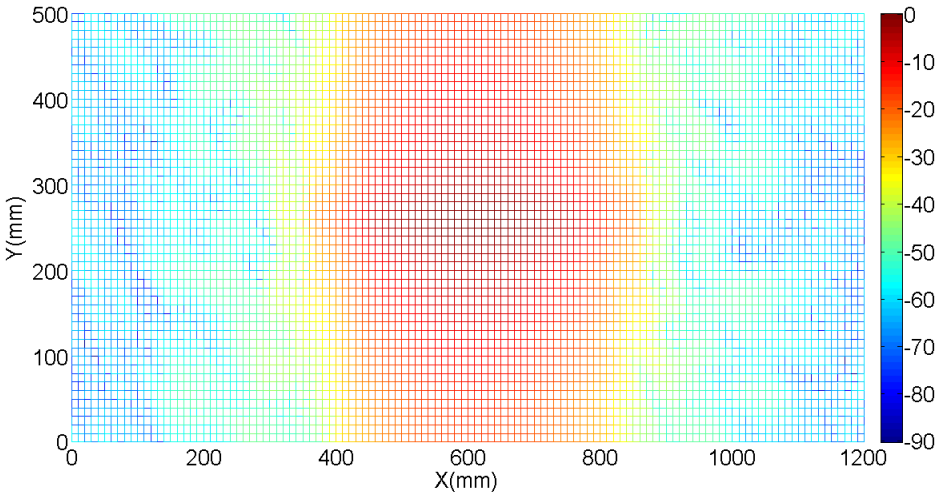

Figure 5.34: Normalised magnitude of 2-D near-field measurement in dB of Dual Shaped Triple Layer Pillbox antenna with low side-lobes

The measured E-field magnitude along the x-axis is compared to the simulated E-field magnitude along the same line in Figure 5.35. These results correlate well up to $-20dB$, after this level the measured data starts to noticeably deviate from the simulated data. The phase measured along the same line is shown in Figure 5.36. Simulated data shows a relatively flat phase between $+/-$ 200mm. The measured phase deviates from the simulated phase by roughly 15° between these positions on the same line. This is still relatively flat and the deviation can be attributed to manufacturing tolerances.

Near-field measurements of the AUT, taken at 10mm increments between 60mm and 90mm, are transformed to the far-field through the near to far-field transform algorithms discussed in Chapter.4.5. Figure 5.37 shows the azimuth far-field patterns obtained from the various E-field measurements. The far-field patterns vary significantly close to the main beam, indicating significant scattering within the measurement setup.

The far-field patterns are averaged to reduce the error introduced through scattering and are shown in Figure 5.38. Probe compensation is done on the averaged pattern to obtain the compensated azimuth far-field pattern at centre frequency in Figure 5.38. Relative side-lobes of $-34dB$ are obtained from the manufactured model which is significantly less than the simulated $-40dB$ side-lobes.

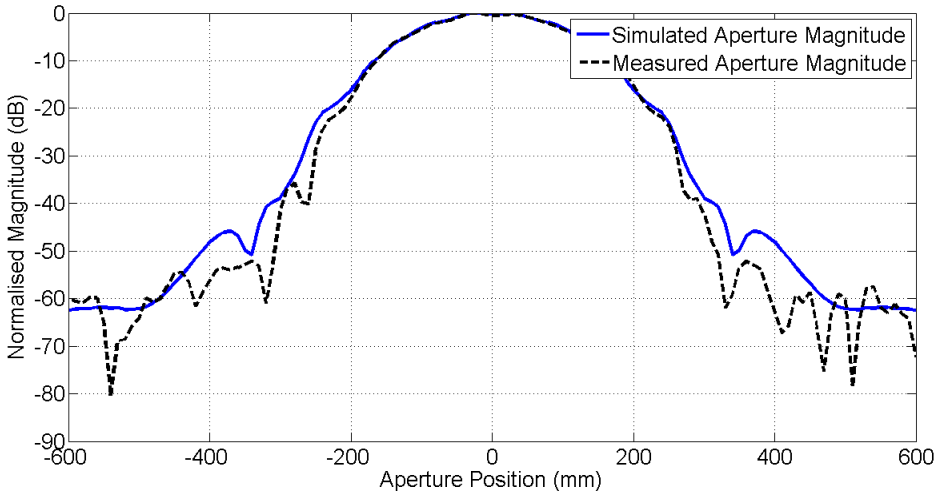

Figure 5.35: Normalised magnitude in dB of near-field measurement along the x-axis of the Dual Shaped Triple Layer Pillbox antenna with low side-lobes, compared to simulated results

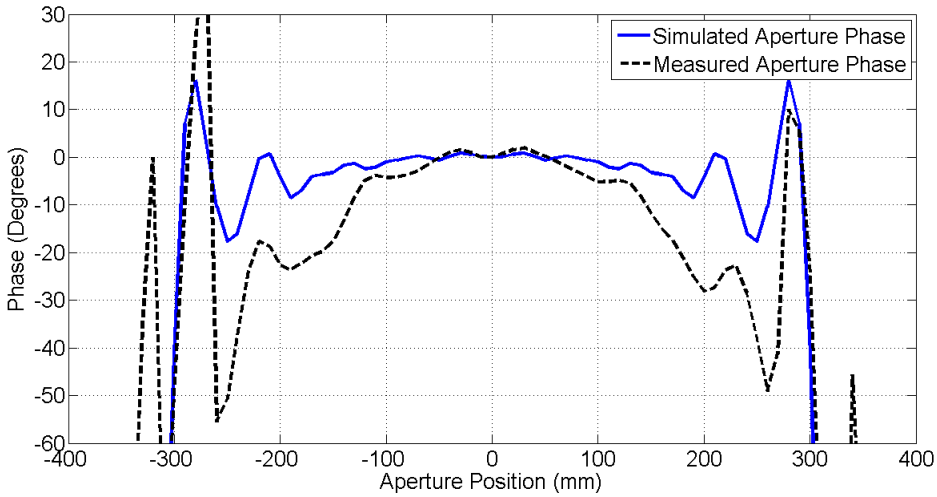

Figure 5.36: Phase of near-field measurement along the x-axis of the Dual Shaped Triple Layer Pillbox antenna with low side-lobes, compared to simulated results

The measured azimuth far-field patterns at $8.5GHz$, $9.5GHz$ and $10.5GHz$ are shown in Figure 5.39. Side-lobes of less than $-34dB$ are obtained at the centre frequency of $9.5GHz$ whereas $-40dB$ side-lobes are found through simulation in Figure 5.40. Measured side-lobes of less than $-32dB$ are obtained at the cut-off frequencies of $8.5GHz$ and $10.5GHz$ which are roughly $2dB$ more than the simulated $-34dB$ side-lobes. The difference in measured side-lobe

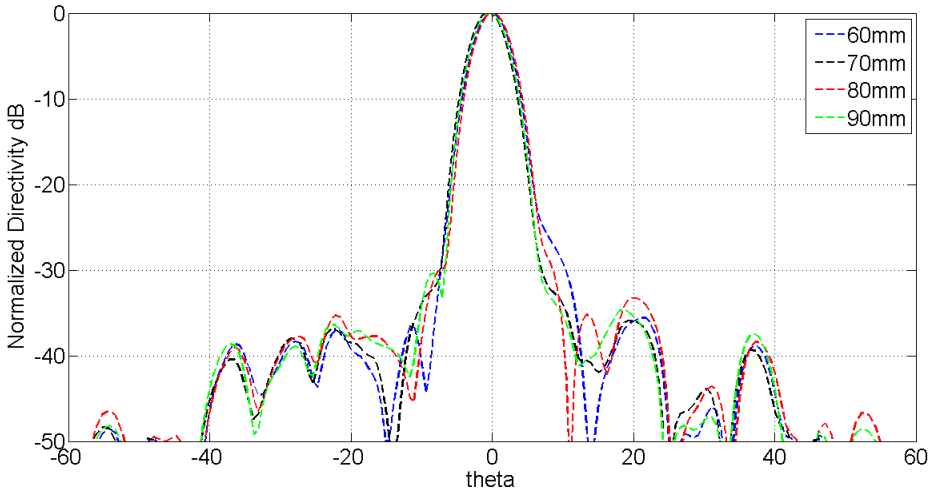

Figure 5.37: Azimuth far-field results obtained from near-field measurements taken at different distances between the probe and Dual Shaped Triple Layer Pillbox with low side-lobes

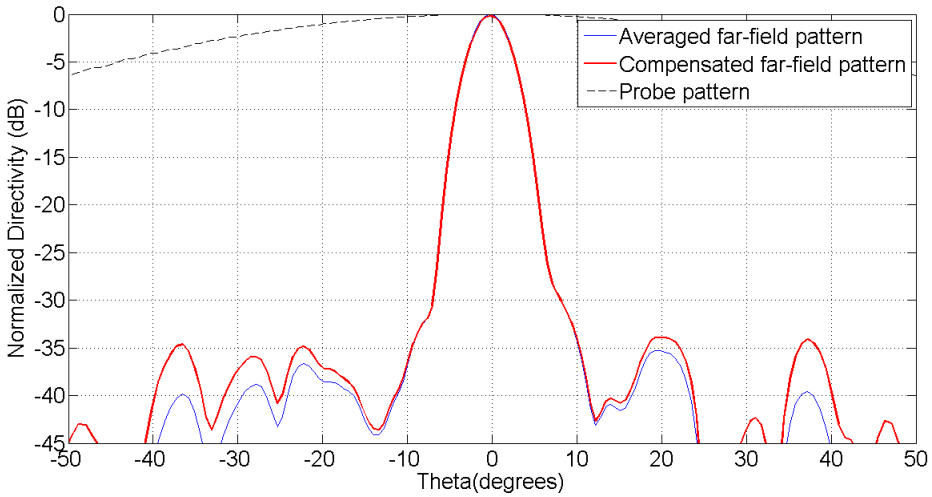

Figure 5.38: Azimuth far-field pattern of Dual Shaped Triple Layer Pillbox with low side-lobes at centre frequency before and after probe compensation is done

levels to the simulated results could be attributed to the surface roughness at the reflectors due to the laser-cutting process together with the miss alignment of the stacked plates. From [16] the minimum side-lobe level that can be obtained from a reflector antenna is expressed as a function of surface error through,

$$SLL = tan^2(\Delta\phi), \tag{5.48}$$

where $\Delta\phi$ is the surface error in degrees. From (5.48) it is determined that a surface roughness of less than $47\mu m$ is needed for $-40dB$ side-lobes to be obtained. Although aluminium plates can be cut to have a surface roughness off less than this, it is unlikely that the plates are aligned to such a low tolerance.

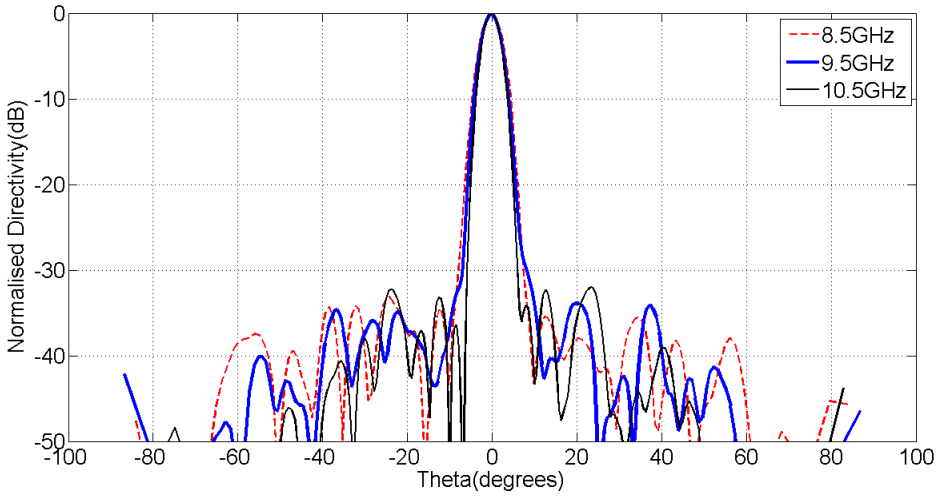

Figure 5.39: Measured azimuth far-field pattern of constructed Dual Shaped Triple Layer Pillbox with low side-lobes over the 20% bandwidth

The measured reflection coefficient is compared to the simulated results in Figure 5.41. The measured result does not compare well to the simulated result, possibly due to manufacturing tolerances. A reflection coefficient of less than $-10dB$ is still obtained for the required bandwidth.

Figure 5.42 shows the E-field in the far-field at centre frequency which was obtained during the gain measurement of the low side-lobe antenna. From this data, $Etot_{AUF}$ in equation (5.47) is calculated as $172dB$. The gain of the dual shaped triple layer pillbox antenna with low side-lobes is thus calculated as $19.8dBi$. A simulated gain of $20.3dBi$ was obtained which is $0.5dB$ more than the measured gain.

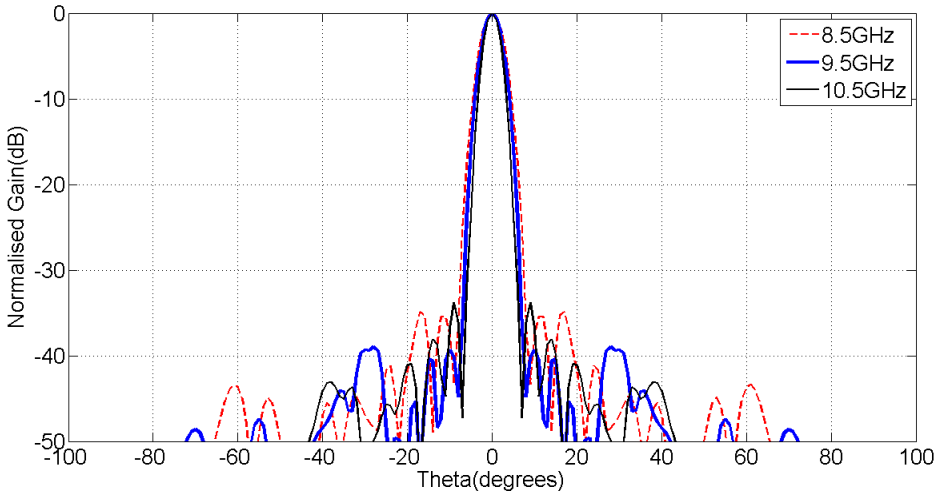

Figure 5.40: Simulated azimuth far-field pattern of constructed Dual Shaped Triple Layer Pillbox with low side-lobes over the 20% bandwidth

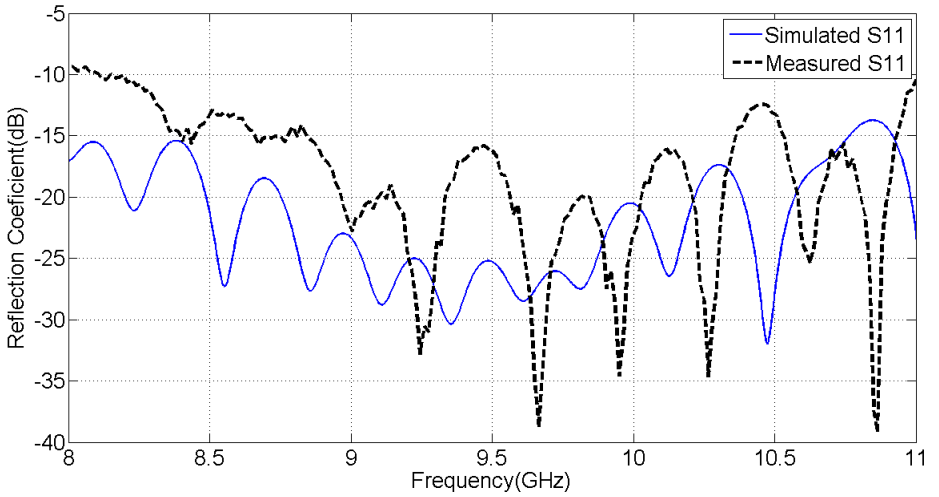

Figure 5.41: Measured reflection coefficient of Dual Shaped Triple Layer Pillbox with low side-lobes compared to its simulated result

5.4.3 Measurements of Dual Shaped Pillbox Antenna with High Gain

The dual shaped triple layer pillbox antenna with high gain is measured using the methods described in Chapter.4.5. It was decided to do only one measurement since gain results are less susceptible to the effect of reflections than the side-lobe results are. The most important aspect of this antenna is its gain which needs to be higher than that obtained for the dual shaped pillbox antenna with low side-lobes.

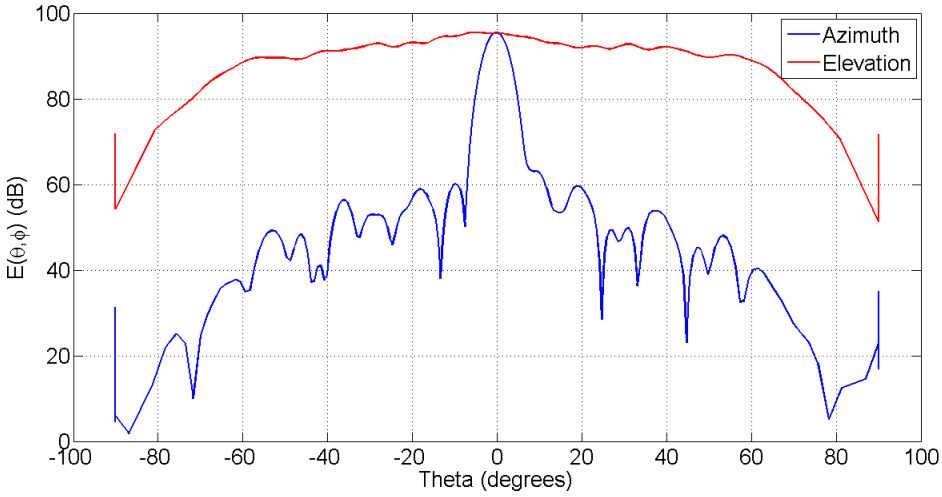

Figure 5.42: Measured E-field far-field pattern of Dual Shaped Triple Layer Pillbox with low side-lobes

Figure 5.43 shows the measured E-field magnitude along the x-axis of the antenna at centre frequency, compared to the simulated results along the same line. Good correlation between the measured and simulated E-field magnitude is obtained. The E-field phase along the same line is shown in Figure 5.44. Good correlation between the measured and simulated phase is found over most of the aperture.

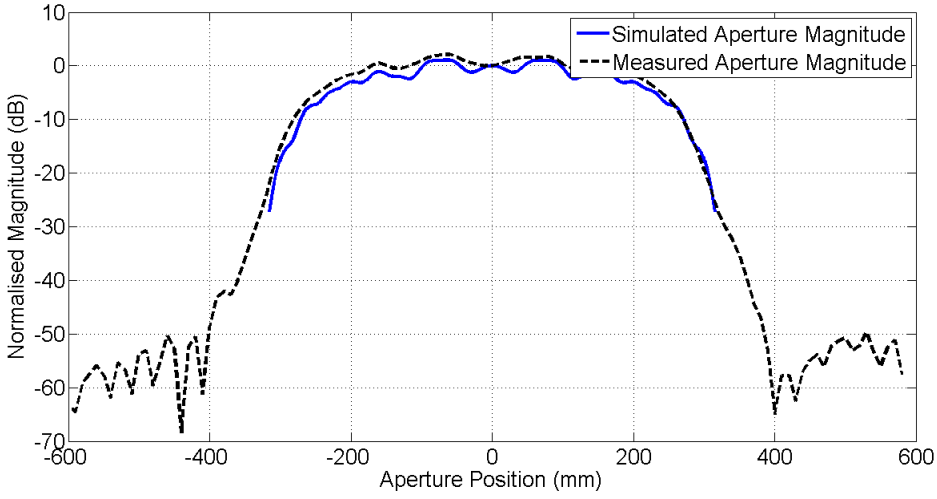

Figure 5.43: Normalised magnitude in dB of near-field measurements along the x-axis of the Dual Shaped Triple Layer Pillbox antenna with high gain, compared to simulated results

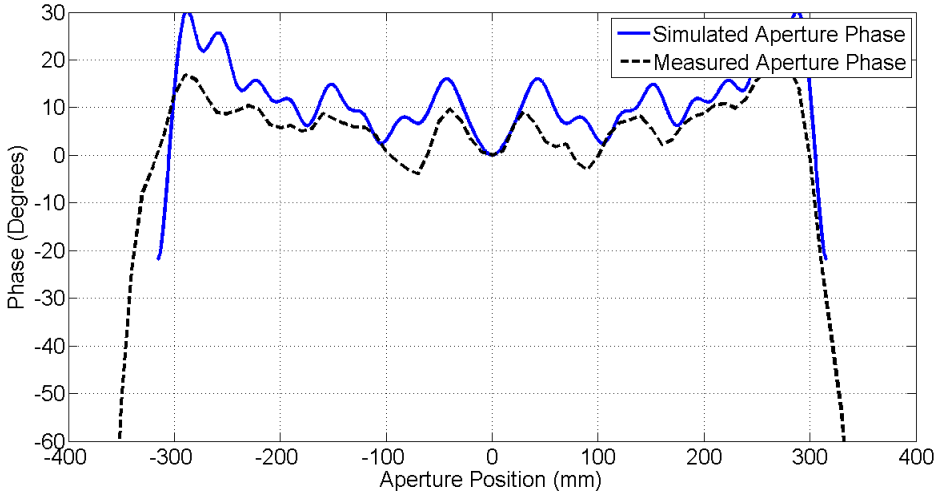

Figure 5.44: Phase of near-field measurements along the x-axis of the Dual Shaped Triple Layer Pillbox antenna with high gain, compared to simulated results

A near to far-field transform is done on the measured E-field data, and then probe compensation is done to obtain the far-field pattern of the antenna. Figure 5.45 shows the azimuth far-field pattern at centre frequency before and after probe compensation.

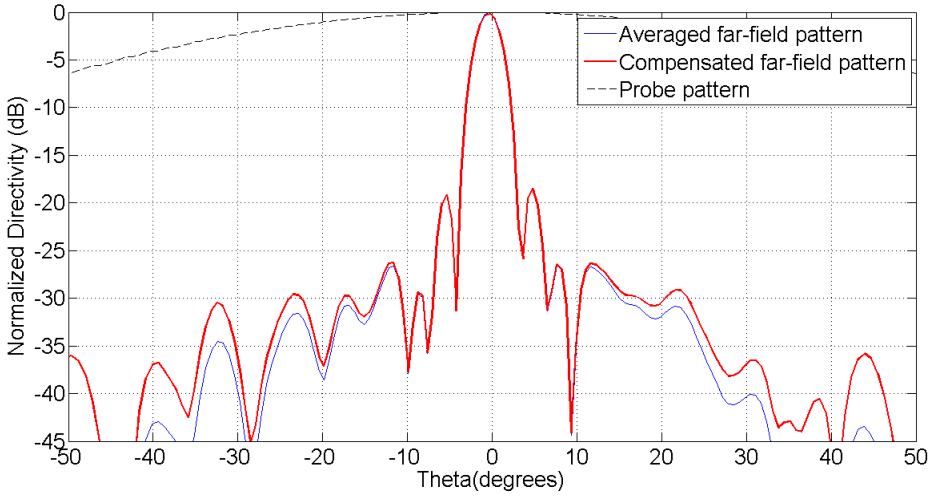

Figure 5.45: Azimuth far-field pattern of Dual Shaped Triple Layer Pillbox with high gain at centre frequency before and after probe compensation is done

The measured azimuth far-field patterns at $8.5GHz$, $9.5GHz$ and $10.5GHz$ are shown in Figure 5.46, whereas the simulated results are shown at the same frequency points in Figure 5.47.

The measured relative side-lobe level of the antenna at centre frequency is $-18.5dB$, whereas the simulated side-lobe level is at $-19.3dB$, which is about $0.8dB$ lower. Similar increases in side-lobes in the measurements are found at $8.5GHz$ and $10.5GHz$. Overall the measured results agree to an acceptable degree with the simulated results.

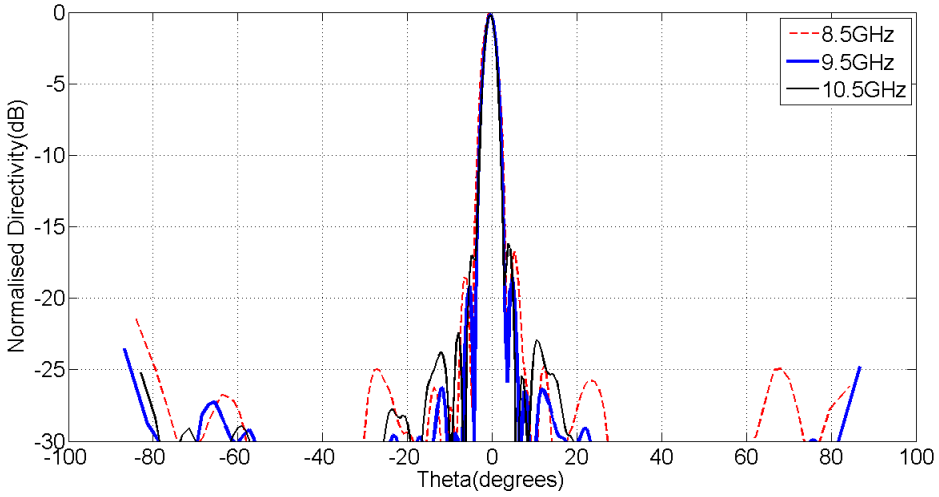

Figure 5.46: Measured azimuth far-field pattern of Dual Shaped Triple Layer Pillbox with high gain over the 20% bandwidth

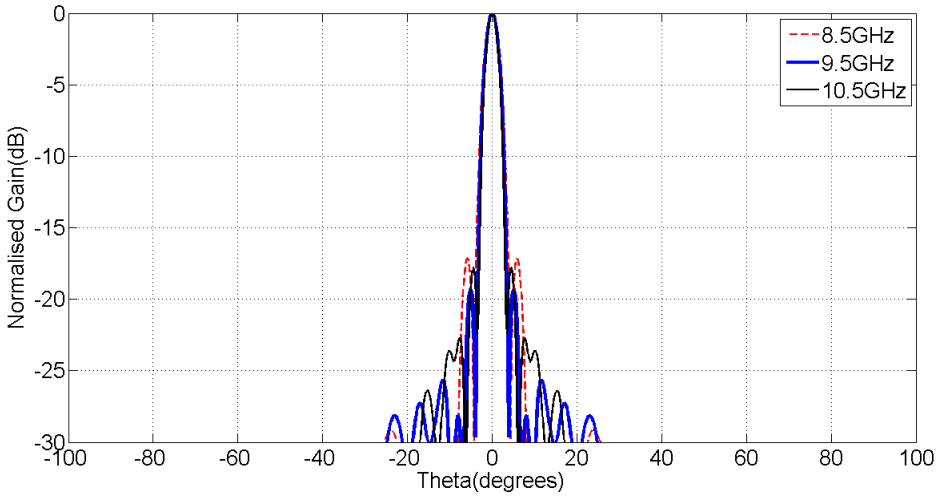

Figure 5.47: Simulated azimuth far-field pattern of constructed Dual Shaped Triple Layer Pillbox with high gain over the 20% bandwidth

The far-field E-field patterns in the azimuth and elevation planes are shown in Figure 5.48.

$E(k_x, k_y)$ is integrated to obtain a value for $Etot_{AUT}$ in $20log_{10}(Etot_{AUT})$ which has a value of $175dB$. This value is used in equation (5.47) to calculate the antenna's gain. A gain of $22.3dBi$ is calculated for the dual shaped triple layer pillbox antenna with high gain. This measured gain correlates well with the simulated gain of $22.3dBi$. From this result it is shown that the dual shaped triple layer pillbox that was designed for high gain delivered $2dB$ more gain than the one designed for low side-lobes.

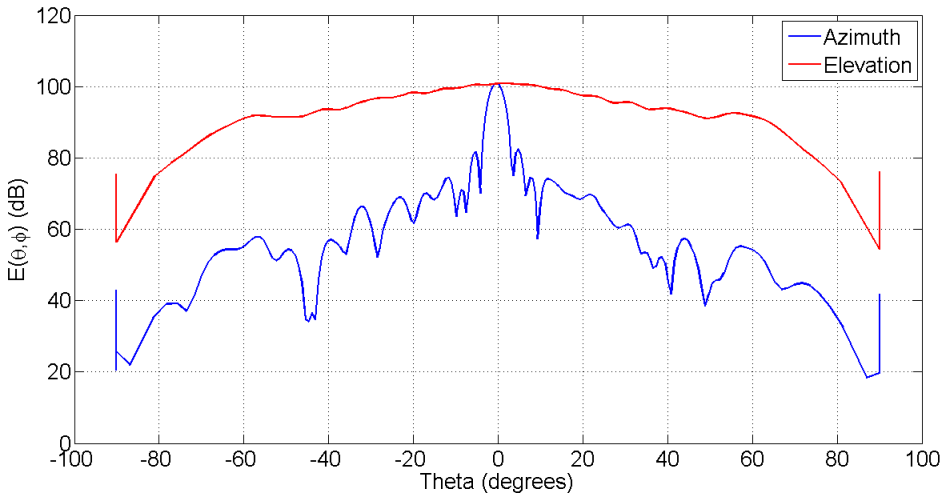

Figure 5.48: Measured E-field far-field pattern of Dual Shaped Triple Layer Pillbox with high gain

5.5 Conclusion on Measured Dual Shaped Antenna Results

The two dual shaped triple layer pillbox antennas which were designed in Chapter.5.3 were constructed using stacked laser-cut aluminium plates.

It was found that the side-lobes obtained through simulation of the low side-lobe antenna were unobtainable through the processes used to manufacture and measure the antenna. Side-lobes at centre frequency of less than $-34dB$ were measured, whereas $-40dB$ was expected.

The measured gain of the high gain antenna was found to be satisfactory, yielding a gain of $22.3dBi$ at centre frequency, which was $2dB$ higher than obtained for the low side-lobe antenna.

Measured results prove that the concept of using dual reflector shaping in a triple layer pillbox structure is valid.

CHAPTER 6
Conclusion

The potential performance of a single layer pillbox antenna was explored. It was found that this configuration would not be able to yield the required bandwidth or side-lobes. Side-lobe levels lower than $-10dB$ could not be obtained although a $-10dB$ reflection coefficient was obtained over a 20% bandwidth for the pin fed pillbox. The primary problem in this design was observed to be the aperture blockage cause by the position of the feed within the aperture.

Aperture blockage was solved by creating a multi layered pillbox structure. The double layer pillbox antenna was formed by placing the feed in a separate layer than the aperture. A compensated transition was designed to couple energy from the feed layer to the aperture layer. A reflection coefficient of less than $-27dB$ was obtained from this transition over the 20% bandwidth for angles of incidence ranging from 90° to 40°. The double layer pillbox antenna yielded acceptable results with side-lobes of less than $-30dB$ and a reflection coefficient of less than $-16.5dB$ acquired for the required frequency band. The protruding feed layer causes an asymmetrical elevation pattern which does not meet the fan beam specifications.

The feed layer was folded back to form the triple layer pillbox antenna. Aperture compensators where designed to match the antenna to free space and yielded a reflection coefficient of less than $-30dB$. Side-lobes of less than $-30dB$ and a reflection coefficient of less than $-20dB$ were obtained through simulation. The antenna was constructed using stacked parallel laser-cut aluminium plates and measured to obtain side-lobes of less than $-27dB$. Results obtained from simulation and measurements meet the required specifications, making the triple layer pillbox antenna a relatively cheap antenna with good performance.

Dual reflector shaping algorithms were derived and implemented in the triple layer pillbox design. An antenna with low side-lobes was designed and built. This antenna yielded $-40dB$ side-lobes through simulation, but only $-34dB$ side-lobes were obtained through measurements. The low simulated side-lobes was not obtained, but the antenna still yielded lower side-lobes than were obtained from the unshaped triple layer pillbox. A high gain antenna was designed and built using the same method. This antenna yielded a simulated and measured gain of $22.3dBi$ which was more than $2dB$ higher than obtained for the other antennas. This result was confirmed by the measured $22.3dBi$ gain. Side-lobes were much higher at $-18dB$ which was expected for the

used cosine distribution. The dual shaped triple layer pillbox antenna was proven to be able to yield a specified radiation pattern through both simulated and measured results.

A design procedure has thus been proposed with which a relatively cheap antenna with good performance can be designed. The procedure is robust and allows for an antenna to be designed to adhere to dimensional restraints while delivering a required radiation pattern.

BIBLIOGRAPHY

[1] R. L. Mattingly, B. McCabe, and M. J. Traube ,"The Split Reflector Technique for Broad-Band Impedance Matching of Center-Fed Antenna Without Pattern Deterioration", Bell Telephone Laboratories, inc, Whippany, N. J.

[2] H. Jasik, "Antenna Engineering Handbook", McGraw-Hill Book Co., New York, sec. 12.4, First Edition.

[3] R. L. Fante, P. R. Franchi, N. R. Kernweis, and L. F. Dennett, "A Parabolic Cylinder Antenna with Very Low Sidelobes", IEEE Trans. Antennas and Propagation, vol. AP-28, no. 1, pp 53-59, January 1980.

[4] W. Rotman, "Wide-Angle Scanning with Microwave Double-Layer Pillboxes", IRE Trans. Antennas and Propagation, pp 96-105, January 1958.

[5] V. Mazzola, and J. E. Becker, "Coupler-Type Bend for Pillbox Antennas", IEEE Trans. Microwave Theory and Techniques, vol. MTT-15, no. 8, August 1967.

[6] CST AG, "CST STUDIO SUITE-GETTING STARTED", Aug 2009.

[7] Balanus, "Antenna Theory", John Wiley & Sons, Inc, Hoboken, sec. 17.2, third edition, 2005.

[8] N. Marcuvitz, "Waveguide Handbook", McGraw-Hill Book Co, Inc, New York, N. Y., First edition, 1951.

[9] EMSS, "FEKO User's Manual", Suite 5.5, July 2009.

[10] S. Gregson, J. McCormick, and C. Parini, "Principles of Planar Near-Field Antenna Measurements", The Institution of Engineering and Technology, London, United Kingdom, sec. 3.2, sec. 4.13, ch. 5, 2007.

[11] A. D. Yaghijian, "Approximate Formulas for the Far Field and Gain of Open-Ended Rectangular Waveguide", IEEE Trans. Antennas and Propagation, vol. AP-32, no 4, April 1984.

[12] V. Galindo, "Design of Dual-Reflector Antennas with Arbitrary Phase and Amplitude Distributions", IEEE Trans. Antennas and Propagation, July 1964.

[13] S. Silver, "Microwave Antenna Theory and Design", McGraw-Hill Book Co., Inc., New York, N. Y., ch 4, sec. 12.16,sec. 13.9; 1949.

[14] A. S. Dunbar, "Calculation of Doubly Curved Reflectors for Shaped Beams", Proceedings of the I.R.E-Waves and Electrons Section, pp. 1289-1296, October 1948.

[15] W. L. Stutzman, G. A. Thiele, "Antenna Theory and Design ", John Wiley & Sons, Inc, New York, sec. 7.6, sec. 9.1, 2nd edition.

[16] J. D. Kraus, R. J. Marhefka, "Antennas For All Applications", McGraw-Hill Book Co., Inc., New York, N. Y., ch 12, sec. 12.10; 2nd edition.

[17] M.Spiegal, J.Liu, Mathematical Handbook of Formulas and Tables

[18] E. L. Holzman, "Pillbox Antenna Design for Millimeter-Wave Base-Station Applications", IEEE Antennas and Propagation Magazine, vol. 45, no. 1, February 2003.

[19] M. Ettore, R. Sauleau, and L. Le Coq, "Multi-Beam Multi-Layer Leaky-Wave SIW Pillbox Antennas for Millimeter-Wave Applications", IEEE Trans. Antennas and Propagation, vol. 59, no. 4, pp. 1093-1100, April 2011.

[20] F. C. de Ronde, "A Simple Full-Band Matched 180 E Plane Waveguide Bend", ISEB Trans. Microwave Theory and Techniques, vol MTT-28, no. 4, April 1980.

APPENDIX A
Parabola Characteristics

The equation for a parabola with focus point f is expressed in cartesian coordinates as

$$y = \frac{x^2}{4f}. \tag{A.1}$$

Rays launched from the focal point of a parabola will be reflected off the parabolic surface parallel to the axis of symmetry of the parabola. A ray originating from the focal point, F, intersects the parabolic reflector at point P and is reflected. The angle of the reflected ray relative to the axis of symmetry of the parabola, y-axis in this case, can be expressed as a function of the angle of the parabola's gradient at point P, θ, and the angle of the ray incident at this point, ϕ.

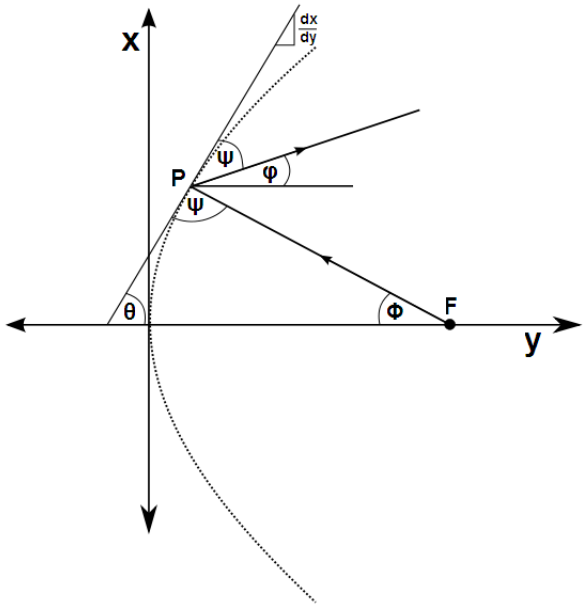

Figure A.1: Diagram illustrating reflected ray angle in parabolic reflector

Using geometry in Figure A.1, the angle of the reflected ray relative to the axis of symmetry, φ, is given as a function of θ and ϕ,

$$\varphi = 2\theta + \phi - \pi. \tag{A.2}$$

The angles θ and ϕ can be written as a function of each other through (A.1). The angle of the gradient relative to the y-axis is given by

$$\theta = tan^{-1}\left(\frac{dx}{dy}\right) \tag{A.3}$$

with dx/dy being the gradient of the parabola at point P,

$$\frac{dx}{dy} = \frac{1}{2}\sqrt{\frac{4f}{y}}. \tag{A.4}$$

The angle of the incident ray is given by

$$\phi = tan^{-1}\left(\frac{\sqrt{4fy}}{f-y}\right). \tag{A.5}$$

Substituting (A.3) - (A.5) in (A.2) gives

$$\varphi = 2tan^{-1}\left(\frac{1}{2}\sqrt{\frac{4f}{y}}\right) + tan^{-1}\left(\frac{\sqrt{4fy}}{f-y}\right) \tag{A.6}$$

which can be simplified through the use of trigometric functions.

$$tan\varphi = tan\left(2tan^{-1}\left(\frac{1}{2}\sqrt{\frac{4f}{y}}\right) + tan^{-1}\left(\frac{\sqrt{4fy}}{f-y}\right)\right) \tag{A.7}$$

Set

$$A = tan^{-1}\left(\frac{1}{2}\sqrt{\frac{4f}{y}}\right) \tag{A.8}$$

$$B = tan^{-1}\left(\frac{\sqrt{4fy}}{f-y}\right) \tag{A.9}$$

giving

$$tan\varphi = tan(2A + B) \tag{A.10}$$

$$tan\varphi = \frac{tan(2A) + tan(B)}{1 - tan(2A)tan(B)} \tag{A.11}$$

$$tan\varphi = \frac{\frac{2tan(A)}{1-tan^2(A)} + tan(B)}{1 - \frac{2tan(A)}{1-tan^2(A)}tan(B)} \tag{A.12}$$

$$tan\varphi = \frac{2tanA + tanB - tan^2AtanB}{1 - tan^2A - 2tanAtanB} \tag{A.13}$$

Substituting (A.8) and (A.9) back into (A.13) gives

$$tan\varphi = \frac{2\left(\frac{1}{2}\sqrt{\frac{4f}{y}}\right) + \left(\frac{\sqrt{4fy}}{f-y}\right) - \left(\frac{1}{2}\sqrt{\frac{4f}{y}}\right)^2\left(\frac{\sqrt{4fy}}{f-y}\right)}{1 - \left(\frac{1}{2}\sqrt{\frac{4f}{y}}\right)^2 - 2\left(\frac{1}{2}\sqrt{\frac{4f}{y}}\right)\left(\frac{\sqrt{4fy}}{f-y}\right)} \tag{A.14}$$

$$= \frac{(f-y)\sqrt{4fy} + y\sqrt{4fy} - f\sqrt{4fy}}{y(f-y) - f(f-y) - 4fy^2} \tag{A.15}$$

$$= 0 \tag{A.16}$$

$$\varphi = 0 \tag{A.17}$$

This thus shows that any ray launched from the focal point is reflected parallel to the axis of symmetry.

The path length from the focal point to the intersection with the directrix of the parabola is the same for all rays as shown in Figure A.2.

A ray originating from the focal point, F, which intersects the parabola at point P and the directrix at B has a length of

$$L1 = FP + PB. \tag{A.18}$$

The length of FP can be calculated through Pythagoras as

$$FP = \sqrt{x^2 + (y - F)^2} \tag{A.19}$$

which transforms to

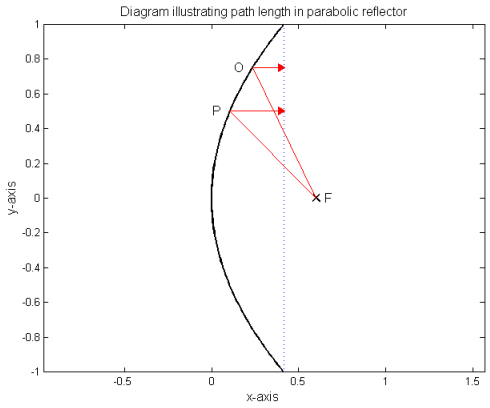

Figure A.2: Diagram illustrating path length in parabolic reflector

$$FP = \sqrt{4yF + (y - F)^2}. \tag{A.20}$$

Further simplification of (A.20) gives

$$FP = y + F. \tag{A.21}$$

The reflected ray is parallel to the axis of symmetry and thus the length of PB is simply

$$PB = B - y, \tag{A.22}$$

giving the total length of the ray as

$$L1 = y + F + B - y. \tag{A.23}$$

A ray traveling from the focal point to intersection point O has a length of

$$L2 = FO + OB. \tag{A.24}$$

Where $FO = F$ and $OB = B$. The difference in path length between ray 1 and ray 2 is thus

$$\Delta L = L2 - L1 \tag{A.25}$$

$$\Delta L = F + B - F - B \tag{A.26}$$

$$\Delta L = 0 \tag{A.27}$$

All rays have thus got the same path length.

APPENDIX B
Antenna-to-antenna Coupling Formula

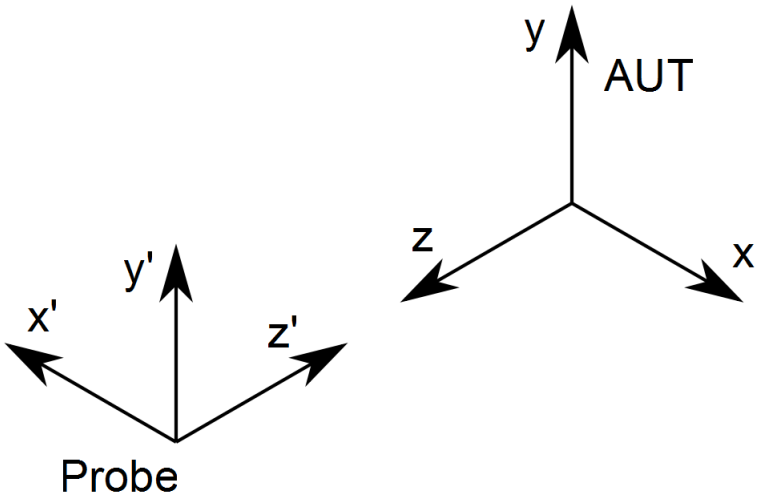

Figure B.1: Antenna-to-antenna measurement coordinate system

$$\hat{e}_{x'} = -\hat{e}_x \tag{B.1}$$

$$\hat{e}_{y'} = \hat{e}_y \tag{B.2}$$

$$\hat{e}_{z'} = -\hat{e}_z \tag{B.3}$$

The unknown plane wave spectral components of the AUT is given by

$$de^A(\alpha,\beta) = \left\{ A_x(\alpha,\beta)\hat{e}_x + A_y(\alpha,\beta)\hat{e}_y - \left(\frac{\alpha}{\gamma} A_x(\alpha,\beta) + \frac{\beta}{\gamma} A_y(\alpha,\beta) \right) \hat{e}_z \right\} d\alpha d\beta. \tag{B.4}$$

The relationship between the direction cosines of a plane wave propagation in the direction k from the AUT to the probe with

$$\begin{aligned} k' &= -k && \text{(B.5)} \\ &= -k_0\left(\alpha\hat{e}_x + \beta\hat{e}_y + \gamma\hat{e}_z\right) && \text{(B.6)} \\ &= -k_0\left(-\alpha\hat{e}_{x'} + \beta\hat{e}_{y'} - \gamma\hat{e}_{z'}\right) && \text{(B.7)} \\ &= k_0\left(\alpha\hat{e}_{x'} - \beta\hat{e}_{y'} + \gamma\hat{e}_{z'}\right) && \text{(B.8)} \\ &= k_0\left(\alpha'\hat{e}_{x'} + \beta'\hat{e}_{y'} + \gamma'\hat{e}_{z'}\right) && \text{(B.9)} \end{aligned}$$

is described by

$$\begin{aligned} \alpha' &= \alpha && \text{(B.10)} \\ \beta' &= -\beta && \text{(B.11)} \\ \gamma' &= \gamma && \text{(B.12)} \end{aligned}$$

and hench the the far-field vector-pattern function of the receiving antenna when receiving unit power $e^C(\alpha', \beta')$, from [10], as described by

$$e^C(\alpha', \beta') = \frac{j}{\lambda}\left\{\left[\gamma'\hat{e}_{x'} - \alpha'\hat{e}_{z'}\right] P_x^C(\alpha', \beta') + \left[\gamma'\hat{e}_{y'} - \beta'\hat{e}_{z'}\right] P_y^C(\alpha', \beta')\right\} \quad \text{(B.13)}$$

becomes:

$$e^C(\alpha, -\beta) = \frac{j}{\lambda}\left\{\left[-\gamma\hat{e}_x + \alpha\hat{e}_z\right] P_x^C(\alpha, -\beta) + \left[\gamma\hat{e}_y - \beta\hat{e}_z\right] P_y^C(\alpha, -\beta)\right\}. \quad \text{(B.14)}$$

The phase reference is changed to the origin of the receiving antenna, yielding

$$\begin{aligned} e^C(\alpha, -\beta) = \frac{j}{\lambda}\Big\{&\left[-\gamma\hat{e}_x + \alpha\hat{e}_z\right] P_x^C(\alpha, -\beta) \\ &+ \left[\gamma\hat{e}_y - \beta\hat{e}_z\right] P_y^C(\alpha, -\beta)\Big\} \times e^{-jk_0(\alpha x_0 + \beta y_0 + \gamma z_0)} \end{aligned} \quad \text{(B.15)}$$

which is expanded to

$$\begin{aligned} e^C(\alpha,-\beta) &= \frac{j}{\lambda}\left\{-\gamma P_x^C(\alpha,-\beta)\hat{e}_x + \alpha P_x^C(\alpha,-\beta)\hat{e}_z \right. \\ &\quad \left. +\gamma P_y^C(\alpha,-\beta)\hat{e}_y - \beta P_y^C(\alpha,-\beta)\hat{e}_z\right\} \times e^{-jk_0(\alpha x_0+\beta y_0+\gamma z_0)} \end{aligned} \tag{B.16}$$

The scalar product of the elemental transmitted wave and this vector-pattern function is

$$\begin{aligned} e^C \cdot de^A &= \frac{j}{\lambda}\left\{-\gamma P_x^C(\alpha,-\beta)A_x(\alpha,\beta) - \alpha P_x^C(\alpha,-\beta)\left(\frac{\alpha}{\gamma}A_x(\alpha,\beta)+\frac{\beta}{\gamma}A_y(\alpha,\beta)\right)\right. \\ &\quad \left. +\gamma P_y^C(\alpha,-\beta)A_y(\alpha,\beta) + \beta P_y^C(\alpha,-\beta)\left(\frac{\alpha}{\gamma}A_x(\alpha,\beta)+\frac{\beta}{\gamma}A_y(\alpha,\beta)\right)\right\} \\ &\quad \times e^{-jk_0(\alpha x_0+\beta y_0+\gamma z_0)} \end{aligned} \tag{B.17}$$

$$\begin{aligned} e^C \cdot de^A &= \frac{j}{\lambda}\left\{\left(\frac{-\gamma^2-\alpha^2}{\gamma}\right)P_x^C(\alpha,-\beta)A_x(\alpha,\beta)\right. \\ &\quad +\left(\frac{\beta\alpha}{\gamma}\right)P_y^C(\alpha,-\beta)A_x(\alpha,\beta) \\ &\quad -\left(\frac{\alpha\beta}{\gamma}\right)P_x^C(\alpha,-\beta)A_y(\alpha,\beta) \\ &\quad \left.+\left(\frac{\gamma^2+\beta^2}{\gamma}\right)P_y^C(\alpha,-\beta)A_y(\alpha,\beta)\right\} \\ &\quad \times e^{-jk_0(\alpha x_0+\beta y_0+\gamma z_0)} \end{aligned} \tag{B.18}$$

Since $\alpha^2+\beta^2+\gamma^2=1$

$$\begin{aligned} e^C \cdot de^A &= \frac{j}{\lambda}\left\{(\beta^2-1)P_x^C(\alpha,-\beta)A_x(\alpha,\beta)\right. \\ &\quad +(\beta\alpha)P_y^C(\alpha,-\beta)A_x(\alpha,\beta) \\ &\quad -(\alpha\beta)P_x^C(\alpha,-\beta)A_y(\alpha,\beta) \\ &\quad \left.+(1-\alpha^2)P_y^C(\alpha,-\beta)A_y(\alpha,\beta)\right\} \\ &\quad \times \frac{e^{-jk_0(\alpha x_0+\beta y_0+\gamma z_0)}}{\gamma} \end{aligned} \tag{B.19}$$

Take

$$\begin{aligned} s(x,y) = e^C \cdot e^A &= \frac{j}{\lambda}\left\{(\beta^2-1)P_x^C(\alpha,-\beta)A_x(\alpha,\beta)\right. \\ &\quad +(\beta\alpha)P_y^C(\alpha,-\beta)A_x(\alpha,\beta) \\ &\quad -(\alpha\beta)P_x^C(\alpha,-\beta)A_y(\alpha,\beta) \\ &\quad \left.+(1-\alpha^2)P_y^C(\alpha,-\beta)A_y(\alpha,\beta)\right\} \\ &\quad \times\frac{e^{-jk_0(\alpha x_0+\beta y_0+\gamma z_0)}}{\gamma}d\alpha d\beta \end{aligned} \tag{B.20}$$

Therefore if $S(\alpha,\beta)=\int_{-\infty}^{\infty}\int_{-\infty}^{\infty}s(x,y)e^{jk_0(\alpha x+\beta y)}dxdy$,

$$\begin{aligned} S(\alpha,\beta) &= \frac{j}{\lambda}\left\{(\beta^2-1)P_x^C(\alpha,-\beta)A_x(\alpha,\beta)\right. \\ &\quad +(\beta\alpha)P_y^C(\alpha,-\beta)A_x(\alpha,\beta) \\ &\quad -(\alpha\beta)P_x^C(\alpha,-\beta)A_y(\alpha,\beta) \\ &\quad \left.+(1-\alpha^2)P_y^C(\alpha,-\beta)A_y(\alpha,\beta)\right\}\frac{e^{-jk_z z_0}}{\gamma} \end{aligned} \tag{B.21}$$

Which reduces to

$$S(\alpha,\beta) = \frac{j}{\lambda}\left\{(1-\alpha^2)P_y^C(\alpha,-\beta)A_y(\alpha,\beta)\right\}\frac{e^{-jk_z z_0}}{\gamma} \tag{B.22}$$

if the x-polarised terms are assumed to be negligibly small.

The decoupled AUT pattern is obtained from

$$A_y(\alpha,\beta) = \frac{\lambda}{j}\left\{(1-\alpha^2)^{-1}P_y^C(\alpha,-\beta)^{-1}S(\alpha,\beta)\right\}\gamma e^{jk_z z_0} \tag{B.23}$$

APPENDIX C
Dual Shaped Curve Formulation

From Chapter.5,

$$r_3 = \sqrt{(x_2' - x_2)^2 + y_2^2} = \frac{y_2}{\sqrt{1 - (\frac{dC_p}{dx_2'})^2}} \tag{C.1}$$

$$(x_2' - x_2)^2 + y_2^2 = \frac{y_2^2}{1 - (\frac{dC_p}{dx_2'})^2} \tag{C.2}$$

$$(x_2' - x_2)^2 = \frac{y_2^2(\frac{dC_p}{dx_2'})^2}{1 - (\frac{dC_p}{dx_2'})^2} \tag{C.3}$$

$$x_2 = -\frac{y_2(\frac{dC_p}{dx_2'})}{\sqrt{1 - (\frac{dC_p}{dx_2'})^2}} + x_2' \tag{C.4}$$

Set $\frac{dC_p}{dx_2'} = C$

$$r_2 = \sqrt{(x_2 - x_1)^2 + (\alpha + \beta + y_2 - y_1)^2} \tag{C.5}$$

$$= \sqrt{x_2^2 - 2x_2x_1 + x_1^2 + (\alpha + \beta - y_1)^2 + 2y_2(\alpha + \beta - y_1) + y_2^2} \tag{C.6}$$

Substitute (C.4) into (C.6) and set $(\alpha + \beta - y_1) = G$ for,

$$r_2^2 = \left[\frac{-y_2C}{\sqrt{1 - C^2}} + x_2'\right]^2 - 2x_1\left[\frac{-y_2C}{\sqrt{1 - C^2}} + x_2'\right] + x_1^2 + G^2 + 2y_2G + y_2^2 \tag{C.7}$$

$$= \frac{y_2^2C^2}{1 - C^2} - \frac{2x_2'y_2C}{\sqrt{1 - C^2}} + x_2'^2 + \frac{2x_1y_2C}{\sqrt{1 - C}} - 2x_1x_2' + x_1^2 + G^2 + 2y_2G + y_2^2 \tag{C.8}$$

$$= y_2^2\left[\frac{C^2}{1 - C^2} + 1\right] + y_2\left[\frac{2x_1C}{\sqrt{1 - C^2}} - \frac{2x_2'C}{\sqrt{1 - C^2}}\right] - 2x_1x_2' + x_2'^2 + x_1^2 + G^2 + 2y_2G \tag{C.9}$$

$$= y_2^2\left[\frac{C^2 + 1 - C^2}{1 - C^2}\right] + y_2\left[\frac{2C(x_1 - x_2')}{\sqrt{1 - C^2}} + 2G\right] - 2x_1x_2' + x_2'^2 + x_1^2 + G^2 \tag{C.10}$$

$$= y_2^2\left[\frac{1}{1 - C^2}\right] + y_2\left[\frac{2C(x_1 - x_2') + 2G\sqrt{1 - C^2}}{\sqrt{1 - C^2}}\right] + (x_1 - x_2')^2 + G^2 \tag{C.11}$$

$$r_3 = \sqrt{(x_2' - x_2)^2 + y_2^2} \tag{C.12}$$
$$= \sqrt{x_2'^2 - 2x_2x_2' + x_2^2 + y_2^2} \tag{C.13}$$

Substitute (C.4) into (C.13)

$$r_3^2 = x_2'^2 - 2x_2'(x_2' - \frac{y_2C}{\sqrt{1-C^2}}) + (x_2' - \frac{y_2C}{\sqrt{(1-C^2)}})^2 + y_2^2 \tag{C.14}$$
$$= x_2'^2 - 2x_2'^2 + \frac{2x_2'y_2C}{\sqrt{1-C^2}} + x_2'^2 - \frac{2x_2'y_2C}{\sqrt{1-C^2}} + \frac{y_2^2C^2}{1-C^2} + y_2^2 \tag{C.15}$$
$$= y_2^2\left(\frac{C^2}{1-C^2} + 1\right) \tag{C.16}$$
$$= y_2^2\left(\frac{1}{1-C^2}\right) \tag{C.17}$$

Set $B = C_p - r_1 - C_p(\theta_1)$ so that $B = r_2 + r_3$

$$B - y_2\frac{1}{\sqrt{1-C^2}} = \sqrt{y_2^2\left[\frac{1}{1-C^2}\right] + y_2\left[\frac{2C(x_1-x_2')+2G\sqrt{1-C^2}}{\sqrt{1-C^2}}\right] + (x_1-x_2')^2 + G^2}$$

(C.18)

$$(B - y_2\frac{1}{\sqrt{1-C^2}})^2 = y_2^2\left[\frac{1}{1-C^2}\right] + 2y_2\left[\frac{C(x_1-x_2')+G\sqrt{1-C^2}}{\sqrt{1-C^2}}\right] + (x_1-x_2')^2 + G^2 \quad \text{(C.19)}$$

$$B^2 - 2By_2\frac{1}{\sqrt{1-C^2}} = 2y_2\left[\frac{C(x_1-x_2')+G\sqrt{1-C^2}}{\sqrt{1-C^2}}\right] + (x_1-x_2')^2 + G^2 \quad \text{(C.20)}$$

$$2y_2\left[\frac{C(x_1-x_2')+G\sqrt{1-C^2}}{\sqrt{1-C^2}}\right] + 2By_2\frac{1}{\sqrt{1-C^2}} = B^2 - (x_1-x_2')^2 - G^2 \quad \text{(C.21)}$$

$$2y_2\left[\frac{C(x_1-x_2')+G\sqrt{1-C^2}+B}{\sqrt{1-C^2}}\right] = B^2 - (x_1-x_2')^2 - G^2 \quad \text{(C.22)}$$

$$y_2 = \frac{-\left[(x_1-x_2')^2 + G^2 - B^2\right]}{2\left[(G) + \frac{C(x_1-x_2')+B}{\sqrt{1-C^2}}\right]} \quad \text{(C.23)}$$

$$y_2 = \frac{-\left[(x_1-x_2')^2 + (\alpha+\beta-y_1)^2 - B^2\right]}{2\left[(\alpha+\beta-y_1) + \frac{\left(\frac{dC_p}{dx_2'}\right)(x_1-x_2')+B}{\sqrt{1-\left(\frac{dC_p}{dx_2'}\right)^2}}\right]} \quad \text{(C.24)}$$

Substituting (C.24) in (C.4)

$$x_2 = -\frac{\left(-\left[(x_1-x_2')^2 + G^2 - B^2\right]\right)C}{2\left[(G) + \frac{C(x_1-x_2')+B}{\sqrt{1-C^2}}\right]\sqrt{1-C^2}} + x_2' \quad \text{(C.25)}$$

$$x_2 = \frac{\left[(x_1-x_2')^2 + G^2 - B^2\right]C}{2\left[(G)\sqrt{1-C^2} + C(x_1-x_2') + B\right]} + x_2' \quad \text{(C.26)}$$

$$x_2 = \frac{\left[(x_1-x_2')^2 + G^2 - B^2\right]}{2\left[(x_1-x_2') + \frac{G\sqrt{1-C^2}+B}{C}\right]} + x_2' \quad \text{(C.27)}$$

$$x_2 = \frac{\left[(x_1-x_2')^2 + (\alpha+\beta-y_1)^2 - B^2\right]}{2\left[(x_1-x_2') + \frac{(\alpha+\beta-y_1)\sqrt{1-\left(\frac{dC_p}{dx_2'}\right)^2}+B}{\left(\frac{dC_p}{dx_2'}\right)}\right]} + x_2' \quad \text{(C.28)}$$